LEVEL (12)

ADA087629

ASL-DUST: A TACTICAL BATTLEFIELD DUST CLOUD AND PROPAGATION CODE

VOLUME 1 - MODEL FORMULATIONS

JUNE 1980

Prepared by

James H. Thompson

General Electric—TEMPO
816 State Street
Santa Barbara, CA 93102

Under Contract: DAAD07-76-C-0143

Contract Monitor: Melvin G. Heaps

DTIC
ELECTE
AUG 7 1980

A

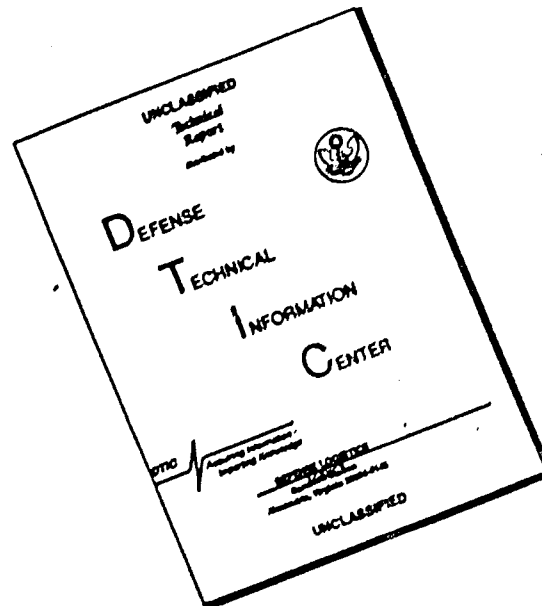Approved for public release; distribution unlimited

US Army Electronics Research and Development Command
ATMOSPHERIC SCIENCES LABORATORY
White Sands Missile Range, NM 88002

80 8 5 083

DISCLAIMER NOTICE

THIS DOCUMENT IS BEST
QUALITY AVAILABLE. THE COPY
FURNISHED TO DTIC CONTAINED
A SIGNIFICANT NUMBER OF
PAGES WHICH DO NOT
REPRODUCE LEGIBLY.

NOTICES

Disclaimers

The findings in this report are not to be construed as an official Department of the Army position, unless so designated by other authorized documents.

The citation of trade names and names of manufacturers in this report is not to be construed as official Government indorsement or approval of commercial products or services referenced herein.

Disposition

Destroy this report when it is no longer needed. Do not return it to the originator.

SECURITY CLASSIFICATION OF THIS PAGE (When Data Entered)

19 REPORT DOCUMENTATION PAGE	READ INSTRUCTIONS BEFORE COMPLETING FORM

1. REPORT NUMBER	2. GOVT ACCESSION NO.	3. RECIPIENT'S CATALOG NUMBER
ASL-CR-80-0143-1	AD-A087629	

4. TITLE (and Subtitle)	5. TYPE OF REPORT & PERIOD COVERED
ASL-DUST: A Tactical Battlefield Dust Cloud and Propagation Code. Volume 1. Model Formulations	Final Report
	6. PERFORMING ORG. REPORT NUMBER

7. AUTHOR(s)	8. CONTRACT OR GRANT NUMBER(s)
James H. Thompson	DAAD07-79-C-0143

9. PERFORMING ORGANIZATION NAME AND ADDRESS	10. PROGRAM ELEMENT, PROJECT, TASK AREA & WORK UNIT NUMBERS
General Electric-TEMPO 816 State Street Santa Barbara, CA 93102	DA Task 1L161102B53A

11. CONTROLLING OFFICE NAME AND ADDRESS	12. REPORT DATE
US Army Electronics Research and Development Command Adelphi, MD 20783	June 1980
	13. NUMBER OF PAGES
	86

14. MONITORING AGENCY NAME & ADDRESS(if different from Controlling Office)	15. SECURITY CLASS. (of this report)
Atmospheric Sciences Laboratory White Sands Missile Range, NM 88002	UNCLASSIFIED
	15a. DECLASSIFICATION/DOWNGRADING SCHEDULE

16. DISTRIBUTION STATEMENT (of this Report)

Approved for public release; distribution unlimited.

17. DISTRIBUTION STATEMENT (of the abstract entered in Block 20, if different from Report)

18. SUPPLEMENTARY NOTES

Melvin G. Heaps, ASL Contract Monitor

19. KEY WORDS (Continue on reverse side if necessary and identify by block number)

Battlefield dust	Electro-optical propagation
Optical transmission	Dust model
Millimeter transmission	Particulates
Infrared transmission	

20. ABSTRACT (Continue on reverse side if necessary and identify by block number)

ASL-DUST is a computer code that models: (1) the dust clouds generated by tactical munitions impacting the ground, and (2) the propagation of electro-optical signals through the resulting dusty environment. This volume discusses the models in ASL-DUST and compares the code results with the experimental data base. Volume 2 is the User's Manual.

DD FORM 1473 EDITION OF 1 NOV 65 IS OBSOLETE 1

SECURITY CLASSIFICATION OF THIS PAGE (When Data Entered)

PREFACE

Several efforts to model the general problem of battlefield obscuration, and specifically that of battlefield dust, have been carried out at and under the auspices of the Atmospheric Sciences Laboratory (ASL) over the past two years. One such effort is documented here; namely, the development of a general research computer code to simulate the effects of artillery produced dust on the transmission of electromagnetic energy. The purpose of this code is to assist the modeler in the interpretation of past test data, and to aid in the methodology and structure of future tests. As is always the case with an on-going effort, this report represents a snapshot in time of a dynamically evolving code. It is necessary to modify the code as the year progresses, and elements of this effort will finally be incorporated into the Electro-Optics Systems Atmospheric Effects Library (EO-SAEL).

Melvin G. Heaps
US Army Atmospheric Sciences Laboratory

3

CONTENTS

LIST OF FIGURES

List of Figures (cont)

LIST OF TABLES

SECTION 1
INTRODUCTION

A wide variety of electro-optical (E-O) sensors are employed in the modern tactical battlefield environment. Dust clouds are generated when tactical munitions detonate at or below the ground surface. These dust clouds can be a major source of degradation for the battlefield performance of the E-O sensors.

In Reference 1, our previous report, we began the task of modeling the munition dust clouds and the propagation of E-O signals through the clouds. Under the present contract we have

- Continued the dust cloud model development
- Written a computer program, ASL-DUST, incorporating the models developed for the dust clouds and the propagation of E-O signals through the clouds
- Validated the models by comparing model predictions with experimental test data.

This volume presents the new dust cloud model developments and the comparisons with test data. Volume 2 (Reference 2) is the User's Manual for the ASL-DUST computer code.

9

SECTION 2
NEW AND IMPROVED DUST CLOUD MODELS

In this section we continue the modeling effort begun in Reference 1. The new and improved dust cloud models include

- Fractionization, that is, mixing of particles among the different size groups
- A base cloud model; this is the ground level, nonrising base surge dust region
- Time delays before horizontal transport of the main and base clouds due to wind transport
- A vertical profile for the mean wind speed
- An improved fallout model for the main dust cloud.

FRACTIONIZATION

We divide the particle size distribution into a number of size groups. The rise, wind transport, diffusion, and fallout of each size group are calculated separately. In the preliminary model we assumed that all particles of a given size group remained within their volume; we assumed nonmixing of particles from one size group volume to another. At later times, differential fallout would produce an absolute separation in the cloud, with the lightest particles at the top of the cloud and the heaviest particles at the bottom. In a real dust cloud we would expect to find, on the average, lighter particles at the top and heavier particles at the bottom, but not the perfect separatio of the preliminary model.

There are many processes in the rising dust cloud that ten to mix the different size particles, especially the lighter particles

10

among the heavier particles. Turbulence, the circulating air flow fields of the rising cloud, nonuniformity of the flow fields over the volume of the size group, and adhesion of smaller particles to each other and to the larger particles will all produce mixing. Since heavier particles are less affected by the mixing processes than lighter particles, we expect mixing to be more efficient as the particle size decreases.

We formulate the following simple model to simulate the particle fractionization. We assume that a fraction of the particles of a given size group is mixed among all larger size groups. Thus a fractionized size group will consist of a mixture of particles from itself and from all smaller size groups. We take a constant fraction of the mass from each size group and distribute this mass among all larger size groups in proportion to the mass fractions of the heavier groups.

Let

F_z = fraction of the mass of a size group that is mixed among the heavier size groups

F_{Mi} = mass fraction of the unmixed size group i (mass of particles in size group i before mixing divided by total mass of all particles)

μ_i = propagation mass coefficient (for extinction, absorption, scatter, or backscatter) for unmixed size group i $(cm^2 \ g^{-1})$

$F_{Ti} = \displaystyle\sum_{j=i+1}^{n} F_{MJ}$ = sum of the mass fractions of all size groups larger than i. Note that F_{Ti} is only defined for i between 1 and n-1, where n is the total number of size groups.

The mass contributed to size group j(j > i) from size group i after mixing is

$$\Delta m_{ij} = M F_{Mi} F_z \frac{F_{Mi}}{F_{Ti}} \quad g \quad , \quad \begin{array}{l} 1 \leq i \leq n-1 \\ j > i \end{array} \tag{1}$$

11

where M is the total mass of all particles (g). The total mass in size group j after mixing is the mass of size group j that is not contributed to larger groups plus the sum of all mass contributions to group j from size groups smaller than j:

$$
M'_j = \begin{cases} MF_{M1}(1 - F_z) & j = 1 \\[2em] MF_{Mj}S_j + MF_{Mj}F_z \displaystyle\sum_{i=1}^{j-1} \frac{F_{Mi}}{F_{Ti}} & 2 \leq j \leq n \end{cases}
\tag{2}
$$

where

M'_j = mass in size group j after mixing (g)

$$
S_j = \begin{cases} 1 - F_z & j < n \\[1em] 1 & j = n \end{cases}
\tag{3}
$$

The factor S_j represents the fraction of unmixed size group j left after contributing mass to larger groups. The last group $(j = n)$ has no larger groups and thus does not contribute mass.

After mixing, each size group has a different mass and (except for size group 1) a different group propagation mass coefficient. The mass fraction of size group j after mixing is

$$
F'_{Mj} = \frac{M'_j}{M}
\tag{4}
$$

The group propagation mass coefficient after mixing is

$$
\mu'_j = \begin{cases} \mu_1 & j = 1 \\[2em] \dfrac{F_{Mj}S_j\mu_j + F_{Mj}F_z \displaystyle\sum_{i=1}^{j-1} \dfrac{F_{Mi}}{F_{Ti}}\mu_i}{F'_{Mj}} & 2 \leq j \leq n \end{cases} \quad cm^2\ g^{-1}.
\tag{5}
$$

We assume that the rise, transport, and diffusion of each size group is still given by the models developed for the unmixed size

12

groups. Hence the cloud location and shape are not changed; only the population of particles within the cloud is mixed. The amount of mixing is controlled by the mixing fraction F_z. For the present we take

$$F_z = \frac{1}{2} \quad .$$

A value of one-half allows a moderate amount of mixing. With this value model predictions of electro-optical transmissions through dust clouds are in good agreement with measured test results.

BASE CLOUD

Figure 1 is an artist's sketch of the dust regions produced by a munition impacting the ground. In Reference 1 we developed models for the main cloud dust region. In this report we will develop models for the base cloud dust region. That part of the stem due to fallout from the main cloud is included in the main cloud models. But no separate geometric stem region is currently modeled.

When a munition detonates at or below the ground surface, a quantity of soil is ejected into the air from the resultant crater. A region of rising, circulating air flow is set up by the shock wave and the buoyant rise of the heated air. Part of the ejected soil is entrained into the rising flow fields and forms the main dust cloud. Part of the soil ejecta is thrown to the side and is not entrained. Also, the explosion-produced shock will scour some additional dust from the ground surface. The base cloud dust region represents that portion of the lofted dust whi h is nonrising.

We assume that the initial base cloud forms instantaneously at burst time, like the main cloud. We use the same spheroidal geometry and Gaussian mass distribution as in the main cloud model, and we scale the initial radii of the base cloud in terms of the initial radii of the main cloud. Let

R_T = initial horizontal radius of the main cloud along the

13
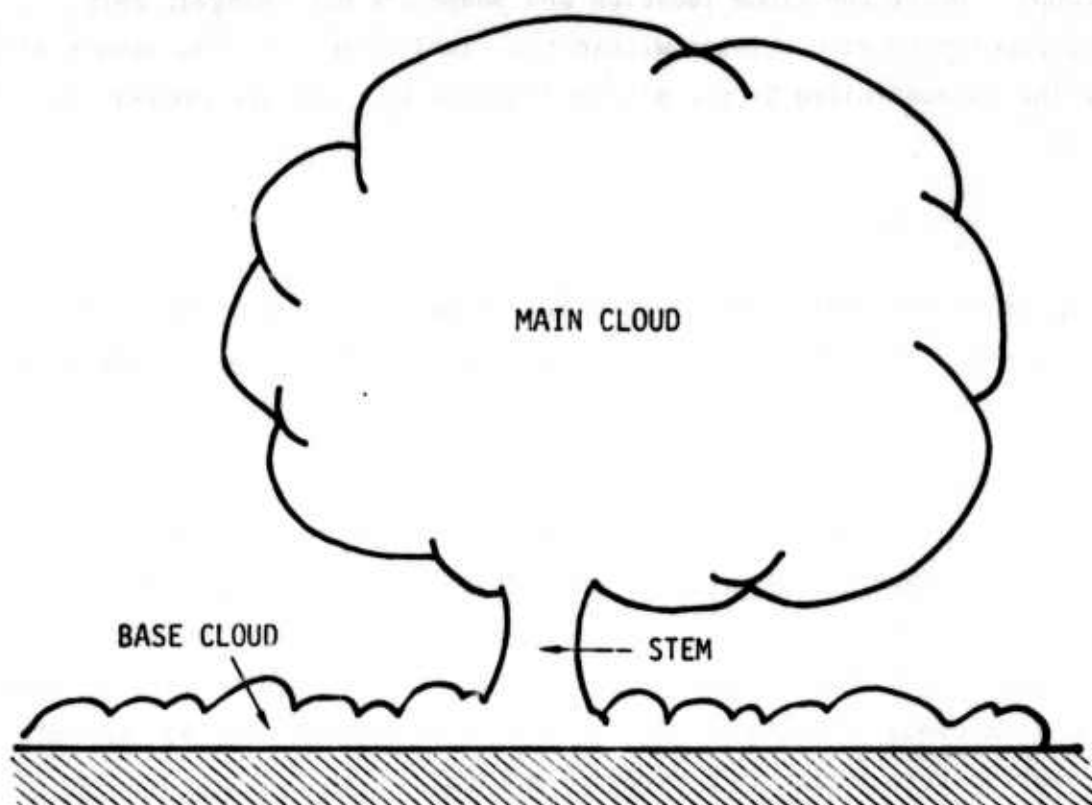
Figure 1. Munition-produced dust regions.

artillery shell track direction (m)

R_P = initial horizontal radius of the main cloud in the direction perpendicular to the shell track (m)

R_V = initial vertical radius of the main cloud (m).

We expect the initial vertical dimension of the base cloud to be about the same as the main cloud, but expect the dimensions to the side to be larger due to the ejecta thrown sideways. We take

$$R_{BT} = B_M R_T \tag{6a}$$

$$R_{BP} = B_M R_P \tag{6b}$$

$$R_{BV} = R_V \quad , \tag{6c}$$

where R_{BT}, R_{BP}, R_{BV} are the corresponding base cloud radii in the shell track, cross track, and vertical directions. B_M is a constant

multiplying factor. Considering the base cloud formation mechanisms, we would expect B_M to be in the range of about 2 to 4. We obtain the best agreement between model and test results by choosing

$$B_M = 3.$$

We assume the base cloud has the same dust and carbon composition as the main cloud, and thus we use the same size groups. At burst time all size groups occupy the same volume. After burst time the groups begin falling out of the cloud, and the wind transports them horizontally. Let the wind be along the positive (horizontal) X-axis, Z is positive upward, and Y is in the cross-wind direction. Then the coordinates of the centroid of the smallest, essentially massless particles are

$$X_{co}(t) = \overline{V}_W \, \Delta t \tag{7a}$$

$$Y_{co}(t) = 0 \tag{7b}$$

$$Z_{co}(t) = R_{BV} \quad ,$$

where

$\overline{V}_W$ = mean wind velocity at altitude Z_{co} (m s^{-1})

Δt = length of time the wind has been transporting the base cloud horizontally (s).

Since the base cloud is nonrising, the Z coordinate of the massless particles remains at the initial position.

For the centroid coordinates of the finite mass size groups, we use the same fallout and transport models as the main cloud:

$$X_{ci}(t) = X_{co}(t) - \frac{1}{C_1}\left[\ln\left\{\left(1 + \frac{C_1 \overline{V}_W}{C_2}\right)e^{C_2 \Delta t} - \frac{C_1}{C_2}\overline{V}_W\right\} - C_2 \Delta t\right] \tag{8a}$$

$$Y_{ci}(t) = 0 \tag{8b}$$

$$Z_{ci}(t) = Z_{co}(t) - V_{ti}\Delta t \tag{8c}$$

15

where

$X_{ci}(t)$ = X coordinate of the centroid of the ith size group (m)

V_{ti} = terminal fall velocity under gravity of the ith size group (m s^{-1})

and C_1 and C_2 are the same main cloud constants as before.

However, the diffusion of the base cloud differs from that of the main cloud. During the rise phase the main cloud diffusion is driven by the buoyant rise velocity and only later is controlled by atmospheric diffusion processes. Since the base cloud is nonrising, its diffusion is atmospherically controlled from the beginning. Table 1, with data taken from Reference 3, shows the scaling factors for angular lateral spread and vertical spread due to atmospheric diffusion as a function of the atmospheric Pasquill stability category. The relations between the scaling factors and the particulate Gaussian standard deviations are

$$\theta(rad) = \frac{4.3\sigma_Y(km)}{X(km)} \tag{9}$$

$$\sigma_Z(km) = aX(km)^S \quad, \tag{10}$$

where

X = downwind distance

$= \dfrac{\overline{V}_W(m\ s^{-1})t}{1000}$ (km)

t = time since release (s)

θ = angular lateral spread (rad)

σ_Y = Gaussian standard deviation for mass density in '' Y (horizontal cross wind) direction (km)

σ_Z = Gaussian standard deviation in the Z (vertical) direction (km)

TABLE 1.   ATMOSPHERIC DIFFUSION SCALING FACTORS

Pasquill Stability Category	θ (deg)	a	s
A	60	0.140	0.90
B	45	0.080	0.85
C	30	0.056	0.80
D	20	0.038	0.76
E	15	0.023	0.73
F	10	0.012	0.67

a,s = scaling factors.

Rewriting the scaling formulas in terms of radii ($r = 2.15\sigma$) and converting distance units to meters, we have

$$r_y(t) = \frac{\theta(\text{deg}) \ \overline{V}_W t}{2(57.296)} \quad \text{m} \tag{11}$$

$$r_z(t) = 2.15(a)10^{3(1-s)}[\overline{V}_W t]^s \quad \text{m} \quad . \tag{12}$$

These radii relations are for a point source. For our case of instantaneous finite source, we take the diffusion relations for the smallest particles to be

$$R_{xo}(t) = R_x(o) + r_y(t) \quad \text{m} \tag{13}$$

$$R_{yo}(t) = R_y(o) + r_y(t) \tag{14}$$

$$R_{zo}(t) = (R_z^{1/s}(o) + r_z^{1/s}(t))^s \quad , \tag{15}$$

where $R_x(o)$, $R_y(o)$, and $R_z(o)$ are the initial base cloud radii in the x, y, and z directions, respectively.

For the finite mass size groups, we assume the same relation as for the main cloud, namely

17

$$\frac{dR_i^2}{dt} = \frac{\dfrac{dR_o^2}{dt}}{\left(\dfrac{16V_{ti}}{\overline{V}_W^2} + 1\right)^{1/2}} \qquad (16)$$

where R_o is the radius of the zero diameter particle group and R_i is the radius of the ith size group. Differentiating and rearranging, the equations for the radii for size group i become

$$R_{xi}(t) = \frac{R_{xo}(t)}{\left(\dfrac{16V_{ti}}{\overline{V}_W^2} + 1\right)^{1/2}} \qquad m \qquad (17)$$

$$R_{yi}(t) = \frac{R_{yo}(t)}{\left(\dfrac{16V_{ti}}{\overline{V}_W^2} + 1\right)^{1/2}} \qquad (18)$$

$$R_{zi}(t) = \frac{R_{zo}(t)}{\left(\dfrac{16V_{ti}}{\overline{V}_W^2} + 1\right)^{s/2(2s-1)}} \qquad . \qquad (19)$$

The total dust and carbon mass lofted into the base cloud is only a small fraction of that in the main cloud. Typical estimates of the base cloud mass are about 5 to 10 percent of the main cloud mass. Many electro-optical sensor sight paths in the battlefield are within the first 2 or 3 meters above the ground. The nonrising base cloud can produce significant attenuation effects on these low-altitude sight paths. The lighter particles in the main cloud rapidly rise above these low sight paths. Thus even though the main cloud has a much larger mass, at later times the attenuation effects from the base cloud are often dominant.

18

TIME DELAYS

A shock wave is produced in the air by the explosion of a munition. We have scaled the initial radius of the dust cloud to the region of strong shock effects. The strong-shock-induced air flow fields and the ejected dust particles will disrupt the smooth, mean wind airflow. It will take a finite time before the mean wind flow is reestablished within the cloud volume. Thus there is a finite time delay before the dust cloud is transported horizontally by the mean wind.

We define a characteristic time of

$$t_c = \frac{D_c}{v_c} \quad s \quad , \tag{20}$$

where D_c is the characteristic distance and v_c is the characteristic velocity. For the base cloud we take the characteristic distance to be the diameter of the strong shock region along the wind track direction,

$$D_c = 2R_{TW} \quad m \quad , \tag{21}$$

and we take the characteristic velocity to be the mean wind velocity at the altitude of the base cloud centroid,

$$v_c = \overline{V}_W \quad m \ s^{-1} \quad . \tag{22}$$

The time delay should be proportional to the characteristic time. A proportionality factor of 2 gives the best fit to the Dugway transmission test data of Reference 4. The time delay for the base cloud is then

$$t_{DB} = 2t_c = \frac{4R_{TW}}{\overline{V}_W} \quad s \quad . \tag{23}$$

The characteristic distance for the main cloud is the same, but we take the characteristic velocity as

$$v_c = \sqrt{\overline{V}_{WM}^2 + V_R^2} \quad m \ s^{-1} \quad , \tag{24}$$

19

where

$\overline{V}_{WM}$ = mean wind speed at a characteristic main cloud altitude of 10 meters (m s^{-1})

V_R = initial buoyant rise velocity of the main cloud (m s^{-1}).

The main cloud time delay is

$$t_{DM} = 2t_c = \frac{4R_{TW}}{\sqrt{\overline{V}_{WM}^2 + V_R^2}} \quad s \quad . \tag{25}$$

VERTICAL WIND PROFILE

The mean wind speed model utilizes the following two assumptions. The direction of the wind does not change with altitude. The wind speed as a function of altitude has the form

$$\overline{V}(Z) = \overline{V}(Z_R)\left(\frac{Z}{Z_R}\right)^{P_W} \quad , \tag{26}$$

where

$\overline{V}(Z)$ = mean wind speed at altitude Z (m s^{-1})

$V(Z_R)$ = mean wind speed at reference altitude Z_R (m s^{-1})

P_W = power law exponent of the vertical wind profile.

The current model for horizontal transport of the dust clouds is very simple. After the time delays the lightest particles in the clouds are transported horizontally with a constant velocity. For the base cloud, the constant horizontal velocity is the mean wind speed at the altitude of the base cloud centroid. The main cloud rises over a range of altitudes. We choose the mean wind speed at 10 meters as the main cloud horizontal transport velocity.

MAIN CLOUD FALLOUT

In the fallout model of Reference 1, we assumed the altitude of the centroid of size group i was given by

$$Z_{ci}(t) = Z_{co}(t) - V_{Ti}t \quad m \quad , \tag{27}$$

where

$Z_{ci}(t)$ = altitude of centroid of size group i at time t (m)

$Z_{co}(t)$ = altitude of centroid of massless particles (altitude of ideal buoyant cloud) (m)

V_{Ti} = terminal fall velocity under gravity of size group i $(m\ s^{-1})$.

This formulation implicitly assumes that the size group experiences the full upward flow of the buoyant rise. But as the larger particles fall below the buoyant cloud, the upward flow velocities experienced by the particles decrease. Hence the particles will fall faster than our simple formulation.

As a first-order correction to allow larger particles to fall faster, we reformulate the fallout to be

$$Z_{ci}(t) = Z_{co}(o) + \left[Z_{co}(t) - Z_{co}(o)\right]\left[1 - \min\left(\frac{V_{Ti}}{V_{RO}}, 1\right)\right] - V_{Ti}t \quad m$$

(28)

where

$Z_{co}(0)$ = initial altitude of buoyant cloud (m)

V_{RO} = initial rise velocity of buoyant cloud $(m\ s^{-1})$.

This formulation assumes that the particles experience only a fraction of the upward flow velocity. The larger the particle terminal velocity is, the smaller the fraction. The smallest particles with essentially zero terminal fall velocity experience the full cloud upward flow velocity, while the large particles with terminal fall velocities equal to or greater than the initial rise velocity do not experience any of the upward flow velocity.

21

SECTION 3
COMPARISONS WITH TEST DATA

INTRODUCTION

All of the models developed in this report and Reference 1 have been incorporated into a munition dust cloud and propagation computer code called ASL-DUST. In this section we assess the validity of the models in ASL-DUST by comparing the code results with experimental test data. In Reference 1 we compared the model results for the main cloud vertical and lateral dimensions as a function of time with the test results from Dugway (Reference 4) and Fort Sill (Reference 5). In this report we compare the model size and altitude predictions with the more recent DIRT-1 test results (References 6 through 11). But our primary goal is to compare the end product of the code with the test results. That is, we want to compare the code predictions for electro-optical propagation through the clouds with the actual measured results. This propagation comparison is the ultimate validity test for a munitions dust code. We compare code results with the infrared transmission data from Dugway and with the visible, infrared, and millimeter transmission data from DIRT-1. We do not have sufficient test site data for Fort Sill to make code predictions to compare with the transmission data.

MODEL COMPARISONS WITH DIRT-1 TEST DATA
Site Geometry

DIRT-1 was a coordinated program to produce information of direct use to the E-O sensor and obscuration modeling communities. Figure 2, taken from Reference 6, shows the test site layout. The path length from the north site to the south site is 2 kilometers. The test area, where explosives were detonated and artillery shells impacted, is 100
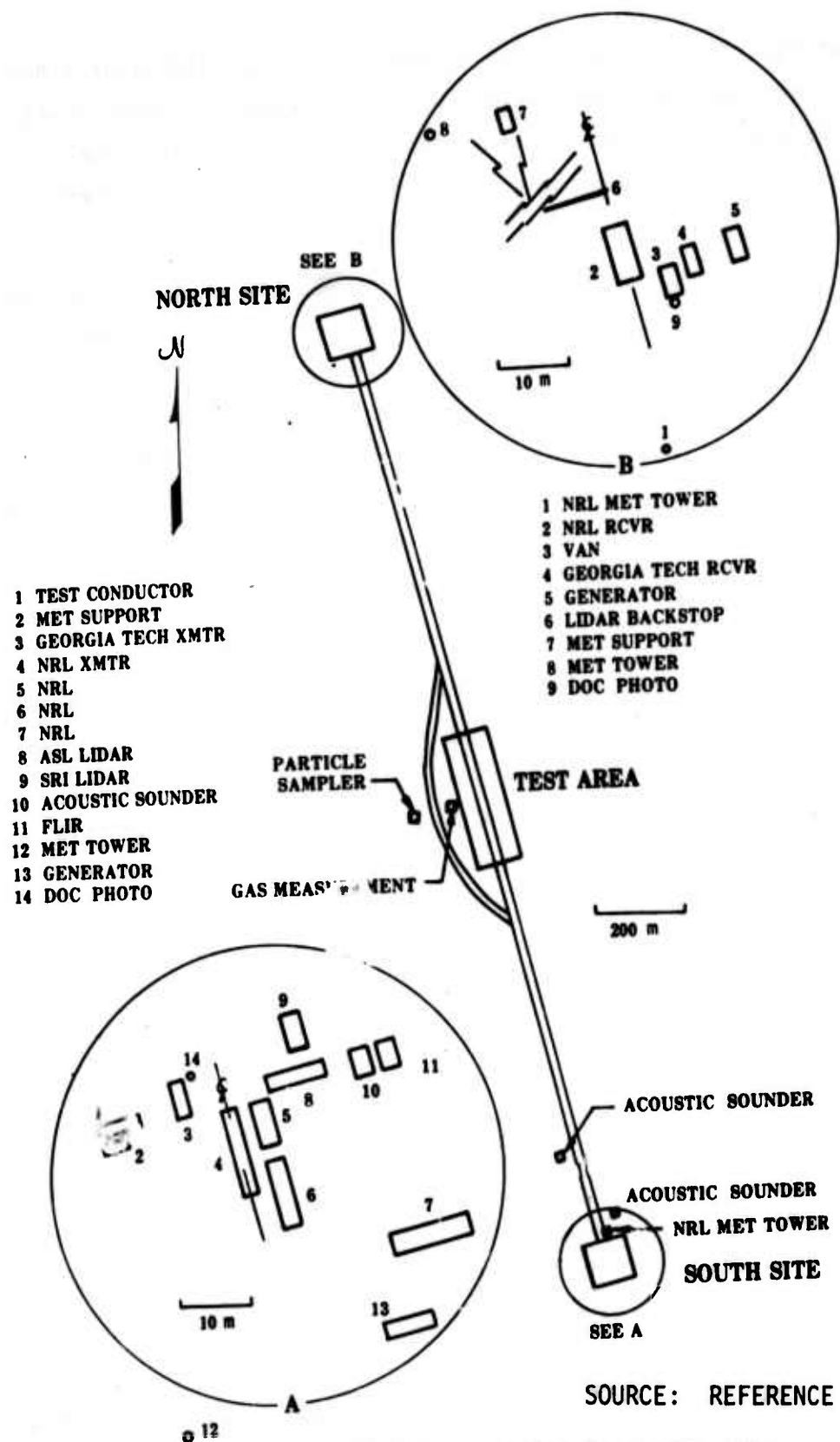
22

NORTH SITE

1 TEST CONDUCTOR
2 MET SUPPORT
3 GEORGIA TECH XMTR
4 NRL XMTR
5 NRL
6 NRL
7 NRL
8 ASL LIDAR
9 SRI LIDAR
10 ACOUSTIC SOUNDER
11 FLIR
12 MET TOWER
13 GENERATOR
14 DOC PHOTO

1 NRL MET TOWER
2 NRL RCVR
3 VAN
4 GEORGIA TECH RCVR
5 GENERATOR
6 LIDAR BACKSTOP
7 MET SUPPORT
8 MET TOWER
9 DOC PHOTO

PARTICLE SAMPLER

TEST AREA

GAS MEASUREMENT

200 m

ACOUSTIC SOUNDER

ACOUSTIC SOUNDER

NRL MET TOWER

SOUTH SITE

SEE A

SOURCE: REFERENCE 6

10 m

Figure 2. Detailed layout of DIRT-1 test site.

23

by 300 meters. Table 2, also from Reference 6, gives the event schedule. The explosives for the events using three TNT charges or three static projectiles were placed on a line perpendicular to the site center-line, one explosion on the centerline and one on each side 15 meters away.

We place our model coordinate system with origin at the ground surface at the midpoint of the site centerline with the Y axis along the centerline pointing north, the X axis perpendicular to the centerline, and the Z axis vertical. The centerline (and Y axis) lies 14.88° west of north. Table 3 shows the transmitter-receiver coordinates assumed for the model. Each set of coordinates defines a sight path, which extends from the transmitter to the receiver. These coordinates were calculated from the sight path data given in Reference 6.

Crater Scaling Factors

Two critical parameters required by any dust obscuration model are the amount and type of material lofted into the air by a munition detonation. The amount of material can be related to the size of the apparent crater left in the soil by the explosion. The model assumes that the scaling relation between the volume of the apparent crater and the yield of the munition is

$$V_A = S_{AC} W^{1.111} \quad m^3 \quad , \tag{29}$$

where

V_A = volume of apparent crater (m^3)
S_{AC} = apparent crater volume scaling factor $(m^3 (lb\ TNT)^{-1.111})$
W = total munition yield (lb TNT).

The scaling factor depends on the type of soil, type of munition, and depth of burst. In Reference 1 we presented illustrations s o ng the scaling factor as a scaled function of depth of burst for se.c. l different soil types.

The data gathered in DIRT-1 were the most complete of any munition dust test series to that date. An extensive crater measurement program

24

TABLE 2. EVENT SCHEDULE FOR DIRT-1

Date (Oct 1978)	Time (MDT)	Event	Size (lb)	Comments
2	0707	A-1	3	Three 1-lb TNT charges
2	0718:30	A-2	45	Three 15-lb TNT charges
2	0729	A-3	90	Three 30-lb TNT charges
2	0739:50	A-4	90	Three 30-lb TNT charges
3	0710	B-1	45	Three 15-lb TNT charges
3	0723	B-2	45	Three 15-lb TNT charges
3	0731	B-3	90	Three 30-lb TNT charges
3	0741:10	B-4	90	Three 30-lb TNT charges
3	0751:20	B-5	180	Three 60-lb TNT charges
3	0801:25	B-6	180	Three 60-lb TNT charges
3	0815	B-7	360	Three 120-lb TNT charges
3	0828:25	B-8	360	Three 120-lb TNT charges
5	0712·50	C-1	2100	One hundred and forty 15-lb charges
6	0717:25	D-1	36	Twelve 3-lb TNT charges
6	0730:40	D-2	72	Twelve 6-lb TNT charges
6	0748:55	D-3	144	Twelve 12-lb TNT charges
6	0807	D-4	288	Twelve 24-lb TNT charges
10	0900	C-2	2100	One hundred and forty 15-lb TNT charges
11	0747:40	E-1	45	Three 155-mm projectiles (TNT), static
11	0757:10	E-2	45	Three 155-mm projectiles (TNT), static
11	0821:45	E-3	180	Twelve 155-mm projectiles (TNT), static
11	0829:05	E-4	180	Twelve 155-mm projectiles (TNT), static
12	0737:10	F-1	60	Four 155-mm projectiles fired simultaneously
12	0748:10	F-2	180	Twelve 155-mm projectiles, rapid fire
12	0805:35	F-3	180	Twelve 155-mm projectiles, rapid fire
12	0823:10	F-4	120	Eight 155-mm projectiles, rapid fire
13	0738:10	F-5	120	Eight 155-mm projectiles, rapid fire
13	0753:35	F-6	120	Eight 155-mm projectiles, rapid fire
13	0808:20	F-7	120	Eight 155-mm projectiles, rapid fire
13	0826:15	F-8	45	Three 155-mm projectiles fired simultaneously
14	0739:50	E-5	45	Three 155-mm projectiles, 2-ft deep, static, 30°
14	0756:00	E-6	45	Three 155-mm projectiles, 2-ft deep, static, 30°
14	0808:45	E-7	45	Three 155-mm projectiles, 1-ft deep, static, 30°
14	0823:55	E-8	45	Three 155-mm projectiles, 1-ft deep, static, 30°
14	0836:10	E-9	45	Three 155-mm projectiles, surface, static, 30°
14	0846:10	E-10	45	Three 155-mm projectiles, surface, static, 30°
14	1056	G-1	-	Diesel oil, rubber, gasoline fire
14	1105:30*	G-1	-	Diesel oil, rubber, gasoline fire
14	1108:50*	G-1	-	Diesel oil, rubber, gasoline fire
14	1111:05*	G-1	-	Diesel oil, rubber, gasoline fire
14	1113:55*	G-1	-	Diesel oil, rubber, gasoline fire
14	1116:40*	G-1	-	Diesel oil, rubber, gasoline fire
14	1119*	G-1	-	Diesel oil, rubber, gasoline fire
14	1122:55*	G-1	-	Diesel oil, rubber, gasoline fire
14	1125:15*	G-1	-	Diesel oil, rubber, gasoline fire
14	1127:15*	G-1	-	Diesel oil, rubber, gasoline fire
14	1129:35*	G-1	-	Diesel oil, rubber, gasoline fire
14	1132:45*	G-1	-	Diesel oil, rubber, gasoline fire

*Command for range cameras on; helicopter approximately 10 to 15 seconds from smoke cloud.

SOURCE: REFERENCE 6

25

TABLE 3. MODEL TRANSMITTER-RECEIVER COORDINATES (meters)

Instrument	Transmitter			Receiver		
	X	Y	Z	X	Y	Z
SRI ruby lidar, 0.69 μm	11.4	-1000	3.2	-9.7	1000	4.66
ASL CO_2 lidar, 10.6 μm	12.3	-1000	3.2	-10.7	1000	3.2
NRL filter transmissometer, 0.55 μm and 10.35 μm	1.2	-1000	1.7	1.2	1000	1.7
ASL millimeter transmissometer, 94 GHz and 140 GHz	-5.9	-1000	2.9	9.1	1000	2.9

was carried out. Table 4 shows the average depth and average diameter of the apparent craters. These data were taken from Reference 7. If we assume that the apparent crater profile is a section of a sphere, then the volume of the apparent crater is

$$V_A = \frac{\pi d}{6} \left(\frac{3D^2}{4} + d^2 \right) \quad m^3 \quad , \tag{30}$$

where

d = apparent crater depth (m)

D = apparent crater diameter (m).

Knowing the apparent crater volume and the event yield, we can solve for the apparent crater volume scaling factor. The scaling factor,

$$S_{AC} = \frac{V_A}{W^{1.111}} \quad m^3 \text{ (lb TNT)}^{-1.111} \quad , \tag{31}$$

is also given in Table 4. We take these scaling factor values as the inputs to the dust model.

Particle Size Distributions

The attenuation due to dust particles at a point along the sight path is determined by the dust mass density at the point, the complex

TABLE 4. APPARENT CRATER DIMENSIONS AND SCALING FACTORS

Event	Yield W (lb TNT)	Depth d(m)	Diameter D(m)	Scaling Factor S_{AC} (m^3[lb TNT]$^{-1.111}$)
A1	1	0.27	0.85	0.0869
A2	15	0.53	1.75	0.0353
A3	30	0.65	2.23	0.0322
A4	30	0.60	2.23	0.0293
B1	15	0.49	1.43	0.0225
B2	15	0.54	1.40	0.0246
B3	30	0.59	1.98	0.0233
B4	30	0.62	1.85	0.0219
B5	60	0.86	3.02	0.0361
B6	60	0.95	3.88	0.0642
B7	120	1.02	3.67	0.0291
B8	120	0.96	3.87	0.0299
C1	15	0.57	1.66	0.0352
C2	15	0.55	1.76	0.0373
D1	3	0.38	1.03	0.0552
D2	6	0.43	1.15	0.0362
D3	12	0.52	1.49	0.0333
D4	24	0.57	2.00	0.0290
E1	≈15 (155 mm shell)	0.49	1.52	0.0250
E2		0.49	1.40	0.0117
E3		0.52	1.40	0.0234
E4		0.52	1.44	0.0245
E5		0.74	2.77	0.120
E6		0.75	2.59	0.109
E7		0.66	2.36	0.0785
E8		0.66	2.26	0.0726
E9		0.50	1.79	0.0343
E10		0.34	1.65	0.0190
F[a]		0.37	1.44	0.0162

[a]Average values for events F1-F8.

index of refraction of the dust particles, and the dust particle size distribution. Due to dust particle fallout and diffusion, the particle size distribution varies as a function of position within the cloud and time after burst. By following the various size groups as a function of time, the model can calculate the particle size distribution at a point provided the size distribution of the initial particles lofted is known. At present there is no adequate method of predicting the initial lofted particle size distribution from the standard physical soil measurements. More munition tests in different soil types are needed before a general size distribution model can be formulated with any confidence.

One standard soil procedure is to use sieve and hydrometer analysis on bulk soil samples to determine the soil grain distribution. In this analysis all of the grains are separated from each other before measurement. Figure 3, reproduced from Reference 7, shows a cumulative grain mass distribution for the DIRT-1 soil. Figure 4 shows this data replotted on log-log paper. Also shown on this figure are the cumulative masses calculated from three standard number size probability distributions, two power laws and one log-normal. We see that a reasonable fit to the soil grain size distribution would be a power law distribution with exponent $p = 3.65$ for grains up to a diameter of 60 microns joined to a log-normal distribution ($a_m = 7.1$ microns, $\sigma = 2.65$) for particles greater than 60 microns.

Can we use the measured soil grain size distribution as the model initial lofted dust particle distribution? We can if the explosion dynamics simply separate and loft the *in situ* soil grains. However, if in the cratering and lofting processes some grains are fractured and/or remain stuck together, then the lofted initial size distribution will differ from the soil grain distribution.

An experiment to measure the actual particle size distributions within the explosively produced dust clouds was fielded in DIRT-1. This experiment consisted of three particulate spectrometers mounted on an airborne platform; the platform was suspended beneath a helicopter, which maneuvered it through the dust clouds at various altitudes

28

Figure 3. Cumulative grain mass distribution curve (from Reference 7).
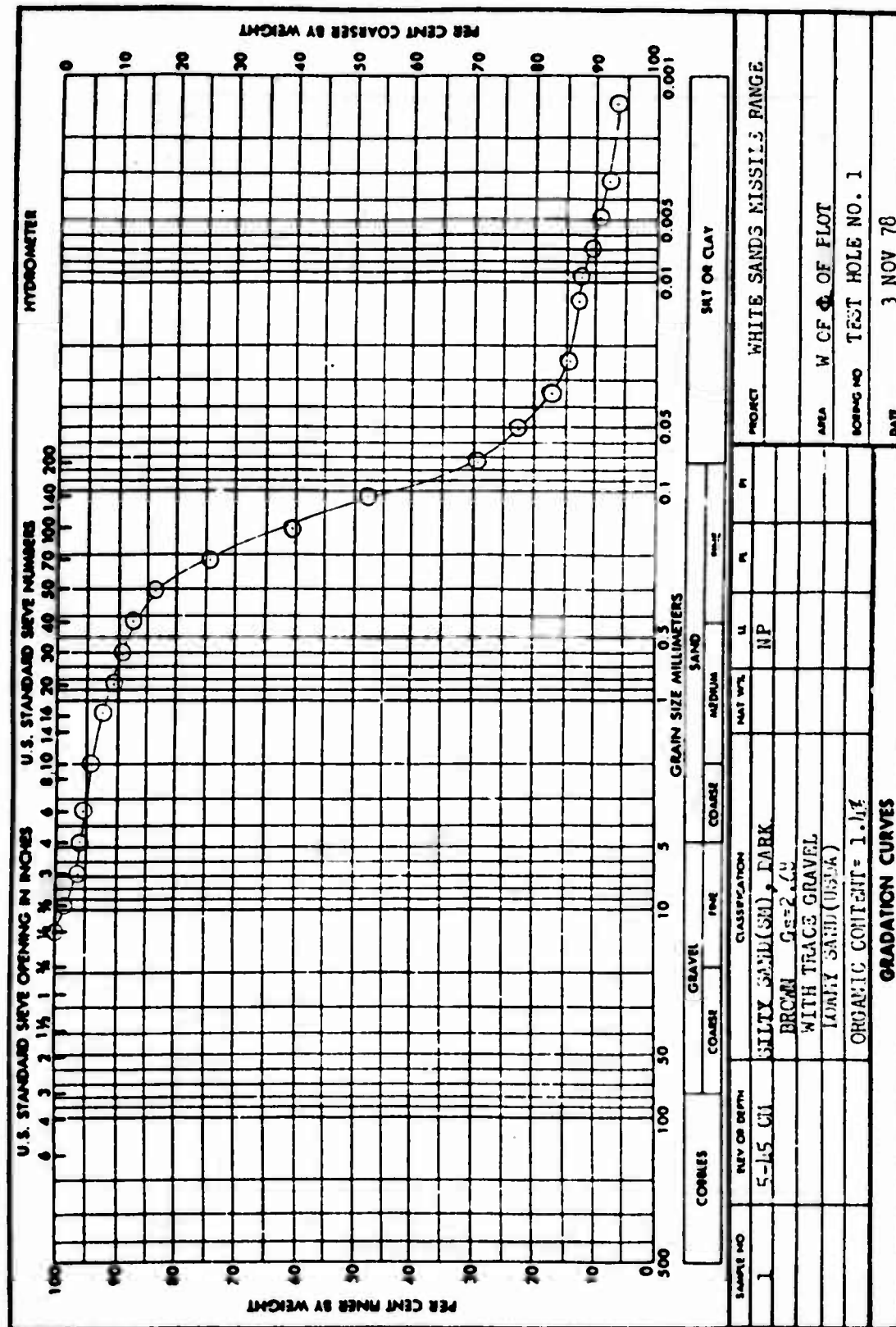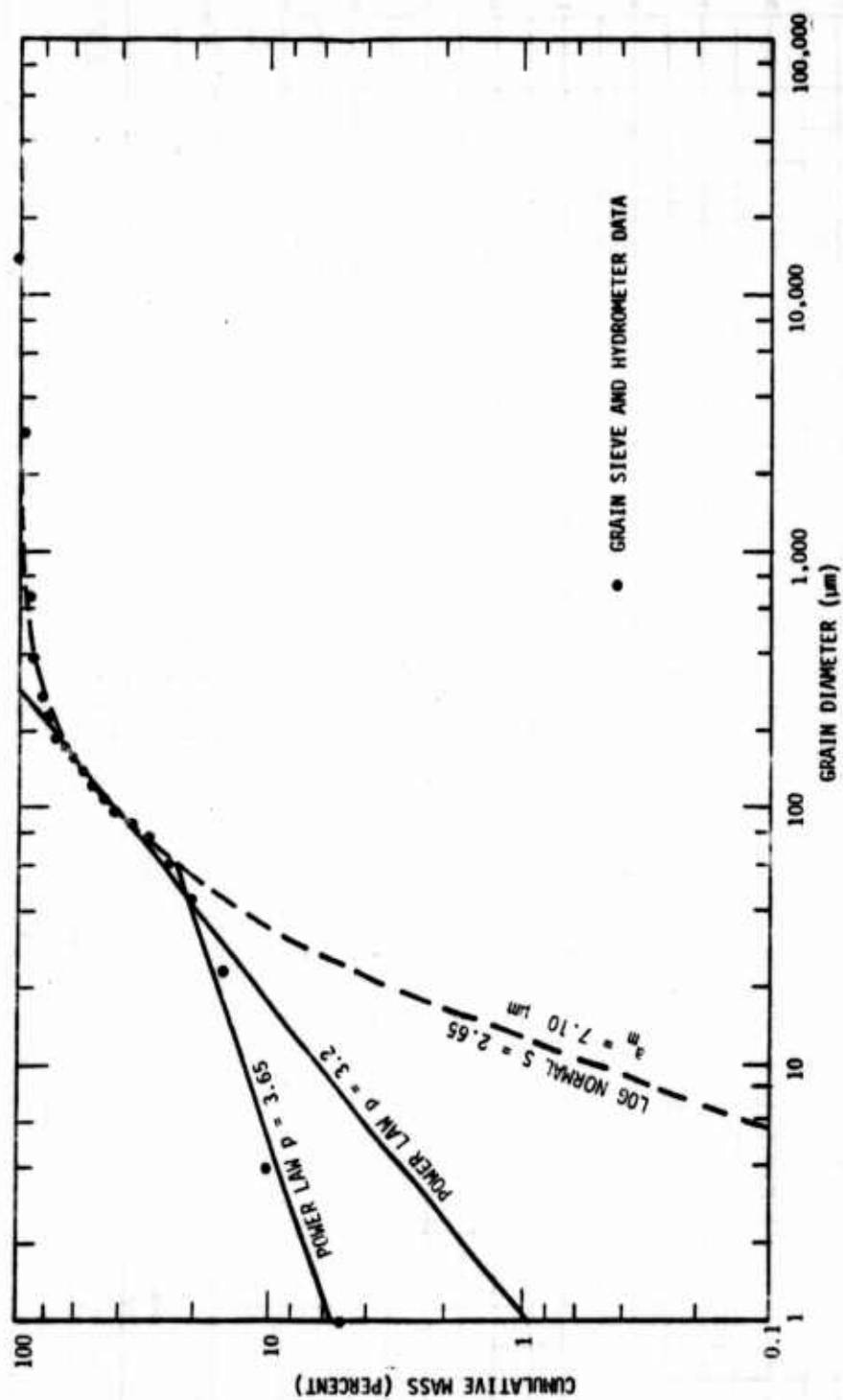
Figure 4. Cumulative grain mass distribution versus grain size.

30

and times after burst. Figure 5 (from Reference 6) shows the particle size distribution measured at 10.6 meters above ground level about 2 minutes after completion of an eight-round barrage of 155-mm super-quick point detonating projectiles (event F6). Note that this figure shows the number size distribution, in contrast to Figures 3 and 4 which show mass cumulative probabilities.

On the log-log graph of Figure 5 a power law distribution plots as a straight line. Fitting a straight line through the data points gives a power law exponent of about 3.4. This value is intermediate between the power law fits to the soil grain data of exponents 3.65 for grains less than 40 microns in diameter and 3.2 for grains bigger than 40 microns.

Integrating the size distribution and normalizing, we have the cumulative probability size distribution shown in Figure 6 plotted on lognormal probability paper. The cumulative distribution from any lognormal size probability distribution plots on this probability paper as a straight line. The fit to the data shown in Figure 6 is a lognormal size probability distribution with

$$a_m = 3.1 \ \mu m$$
$$S = 2.34 \quad .$$

The airborne particle data was taken about 2 minutes after burst. Fallout would have reduced the airborne populations of dust particles larger than about 50 to 100 microns. But airborne particles less than about 10 microns should have been virtually unaffected by fallout at this time. The airborne data show relatively less small particles than the soil grain data. Assuming both sets of data are accurate, the difference suggests that not all of the smaller soil grains are being separated during the cratering and lofting dynamics.

Because of the fallout, the airborne data are of limited use in predicting the initial size distribution of particles greater than about 50 to 100 microns in diameter. Using the code, we input a number
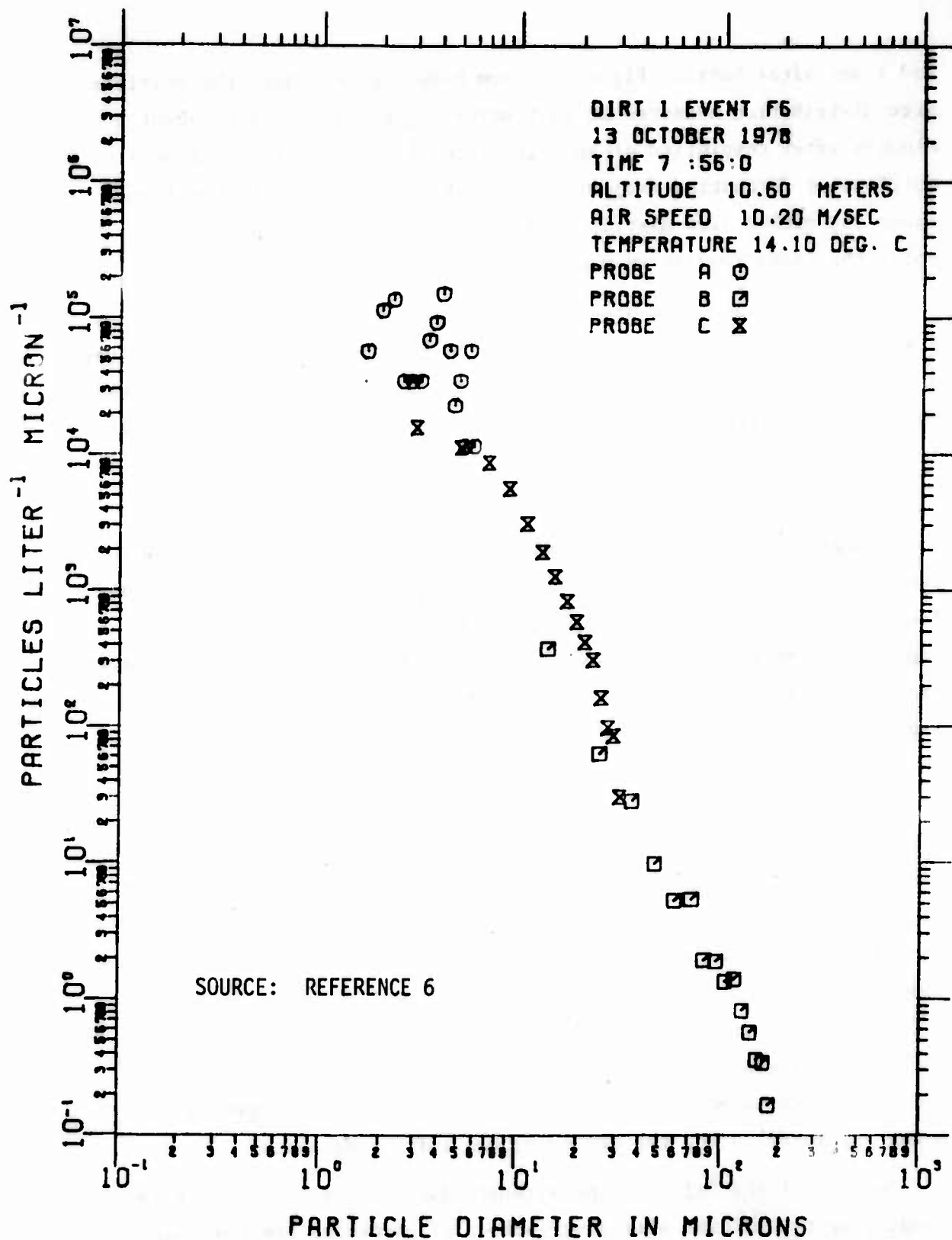
Figure 5. Airborne particle size distribution.
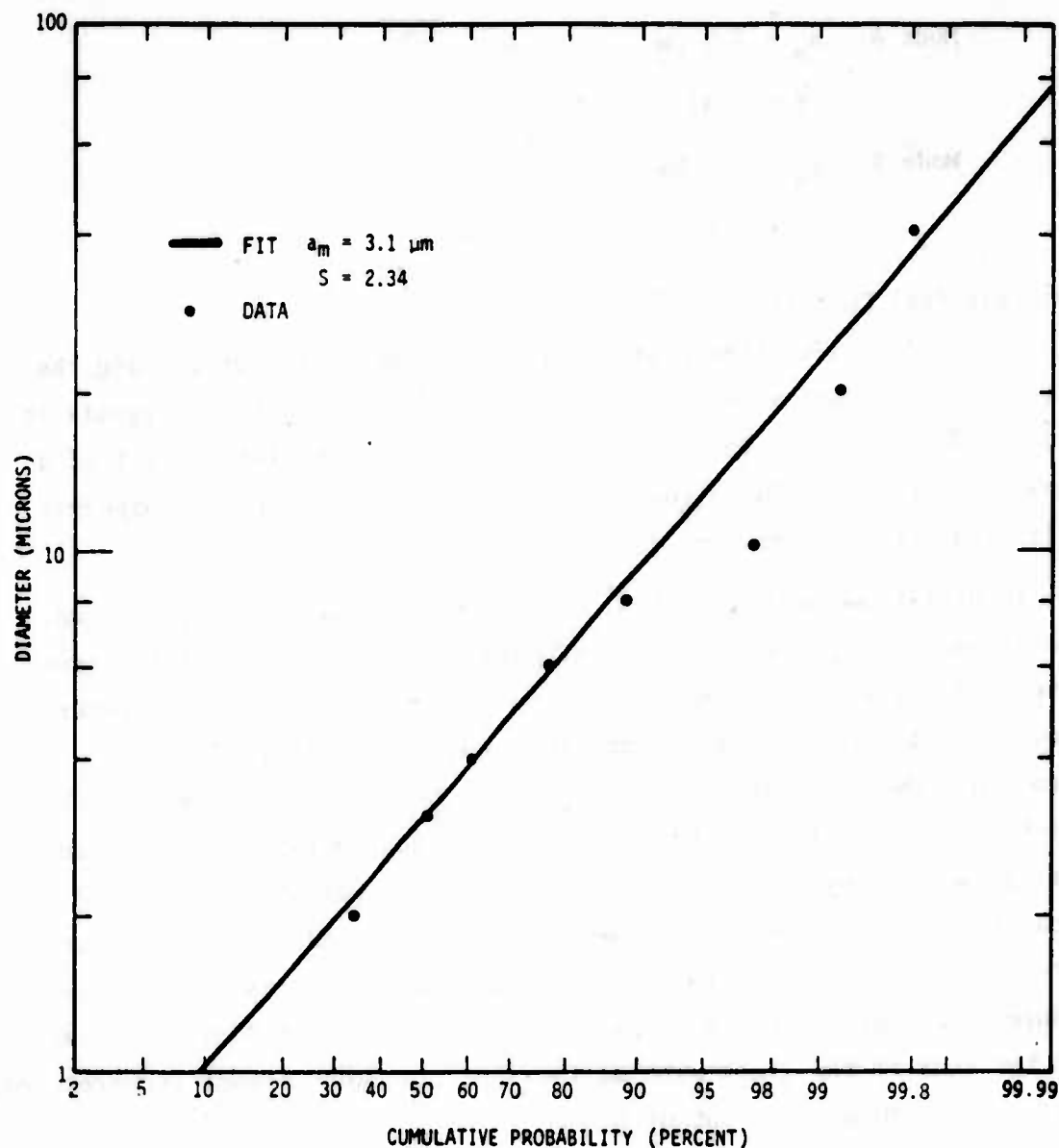
Figure 6. Airborne cumulative size distribution.

of size distributions for the larger particles and compared the predicted transmissions with test data. The log-normal fit to the larger particles in the grain size data, in Figure 4, produces a reasonable fit to the data. For the model we assume a bimodal dust distribution. We take mode A, the small particles, to have the log-normal fit to the airborne data, and take mode B, the larger particles, to have the log-normal fit to the soil grain data. Thus

Mode A: $a_m = 3.1$ µm

$S = 2.34$

Mode B: $a_m = 7.1$ µm

$S = 2.65$.

Meterological Conditions

The wind is often the most important parameter in determining the strength and duration of degradation of the electro-optical signals in a dusty environment. The wind can blow a dust cloud into or out of a sensor sight path. The stronger the wind, the faster the atmospheric diffusion will disperse the dust cloud.

In DIRT-1 two meteorological data collection sites were employed, one at each end of the 2 km optical path (see Figure 2). At the south site the wind direction and speed were measured at 1, 2, and 4 meters above ground level. At the north site only the 2 meter winds were recorded. The wind data were averaged for both a 5-minute and a 10-minute period starting at the beginning of each test event. The winds during all test events were light and extremely variable. The wind data given in Reference 6 show that the average wind direction at one site sometimes changed direction by more than 45 degrees from one 10-minute averaging period to the next. Moreover, the wind direction at the two ends of the sight path at the same time were almost uncorrelated, often being 180 degrees out of phase.

For the dust model we need to specify the mean wind speed at a reference altitude, the exponent of the vertical profile, and the wind direction. We take 2 meters as the reference altitude, and use the 10-minute averaged speed at 2 meters at the south site as the mean wind speed. The wind direction at the midpoint of the sight path is difficult to estimate because of the extreme variability. We make a first estimate by averaging the north and south site directions. We then modify the direction to produce the best agreement between model and test transmission results. For each event we calculate an average

vertical profile exponent using the south site 1-, 2-, and 4-meter
data. We then average all exponents to come up with one average ex-
ponent of 0.19, which we use for all events. Table 5 shows the mean
wind speeds and directions chosen for the dust model inputs.

Other Model Parameters

From the soil measurements of Reference 7, we take the average
moisture fraction of the soil to be 8.4 percent and the average *in situ*
soil density to be 1.6 g cm^{-3}. Table 6 shows the indices of refrac-
tion used in the model. The visible and infrared values are the values
recommended in Reference 6, the carbon values are from Reference 12, and
the millimeter values were chosen to provide agreement between model and
test transmission results.

At its present stage of development, ASL-DUST does not include
multiple-burst interactions. Although the model allows up to 10
bursts, the size, position, and internal mass distribution of each
dust cloud are calculated independently of all other clouds. The
total propagation effect is simply taken as the sum of the individual
effects. If the dust clouds from the multiple bursts are separated
sufficiently so there is little mutual overlap, noninteraction is a
good assumption. However, if the multiple bursts are spaced close
enough in time and space, then the rising dust clouds will intersect;
the air flow fields will interact and rearrange to form one larger
merged cloud from the individual clouds. The single merged cloud will
have different transport, diffusion, and propagation properties than
the sum of the individual clouds.

All of the DIRT-1 test events were multiple bursts. For all but
the smallest yields, the individual clouds rapidly merged to form a
single cloud. For the smallest yields we input the individual bursts.
For the other yields we simulate the single merged cloud in the model
by the following method. We input only a single charge at the center
of the multi-charge layout; the yield of the single charge is the sum
of the individual yields. When the individual clouds first merge, the

35

TABLE 5. MEAN WIND SPEED AND AZIMUTH

Event	Mean Wind Speed (m s^{-1})	(mph)	Wind Azimuth (deg)
B1	1.3	3	70
B2	1.8	4	50
B3	3.6	8	65
B4	1.8	4	60
B5	1.8	4	22
B6	2.2	5	70
B7	1.8	4	26
B8	1.8	4	26
E1	1.3	3	32
E2	0.9	2	17
E5	1.3	3	295
E6	0.9	2	5
E7	1.3	3	240
E8	1.3	3	267
E9	2.2	5	337
E10	1.8	4	22

Notes: Mean wind speed measured at 2 m above ground.
Model azimuth measured from Y axis.
Model azimuth = true azimuth + 14.88°.

TABLE 6. COMPLEX INDICES OF REFRACTION

Wavelength or Frequency	Material	
	Dust	Carbon
0.55 µm	1.525 - i 0.005	1.53 - i 0.005
10.6 µm	1.65 - i 0.14	1.65 - i 0.14
94 GHz	1.45 - i 0.033	2 - i 1

merged single cloud is larger than the cloud from an equivalent single
burst. Also the rise rate of the merged cloud is smaller than the
equivalent single-burst cloud. We roughly account for both of these
effects in the model by increasing the entrainment factor, α, from
its nominal value of 1 to a value of 2. This increased α factor will
cause the equivalent single cloud to entrain ambient air more rapidly.
The increased entrainment will cause the cloud to grow more rapidly in
size and to rise at a slower rate, thereby more closely simulating the
behavior of the merged cloud.

In general, the other model parameters not mentioned were set at
the model default values.

Size and Altitude Comparisons

When Reference 1 was prepared, only the Fort Sill and Dugway test
data were available; we did not have any cloud altitude test data to
compare against the model predictions. The DIRT-1 test data does in-
clude cloud altitude; Figures 7 through 13* show the ASL-DUST model
comparisons with the test data for the B-series of events. The test
data shown are for the centroid of the whole main cloud. The model
data shown are for the centroid of the size group of the smallest
particles. Until fallout becomes significant at later times, these
two centroids should be approximately equal. At later times we expect
the whole cloud centroid to fall below the smallest particles centroid.

*Figures 7 through 55 are on pages 45 through 84.

In general the intermediate and later time comparisons are as expected; the two centroids are approximately equal, and then the test data centroid falls below the model centroid. In the first few seconds the test data centroid is higher than the model centroid. The model altitude is that of a buoyantly rising cloud. However, for about the first second, the cloud rise is controlled by the shock-induced air flow fields. These predominantly upward flowing fields carry the cloud upward one or two cloud diameters. The shock-induced rise forces die away and the buoyant rise force controls the rise history thereafter. This first-second nonbuoyant rise regime should be scalable from the shock and initial cloud dimensions. A model for this effect will be added to ASL-DUST at a later date.

Figure 14 shows the cloud geometry of event B7 with the model predictions superimposed. This event is three 120-lb charges in a line 15 meters apart. The early time cloud is thus wider than the cloud from a single 360-lb charge. In the model we simulate this three-charge event with a single 360-lb charge with an enhanced entrainment coefficient. The geometry comparisons show the expected early time difference, but the comparisons are quite good from about 10 seconds on. The comparisons at 20 seconds illustrate the differences in the two centroids. The model centroid and geometry are a good fit to the upper cloud, where we expect the smaller particles to reside. In the model, the lower part of the cloud is accounted for by the fallout of the larger size groups.

Attenuation Comparisons

The DIRT-1 B-series of events is particularly valuable for model comparisons. The events have a fairly large yield range, from three 15-lb charges to three 120-lb charges. Test data were taken on crater size, cloud size and altitude, and cloud attenuation at visible, infrared, and millimeter wavelengths. All these test data provide a good test for any dust cloud model. The wide range of wavelengths in the attenuation measurements provide both early and late time comparisons

38

as well as the spectral sensitivity comparisons. The significant milli-
meter attenuation generally lasts less than about 10 seconds; the vis-
ible and infrared attenuation can last for hundreds of seconds. Thus
the millimeter data provide a data base for validation of the early
time model, while the visible and infrared data provide a late time
data base.

Figures 15 through 25 show the data (Reference 8) and model compar-
isons at 94 GHz for events B4 through B8, and events E5 through E10.
For the B series the chart recorder time constant was 400 ms, and for
the E series it was changed to 40 ms. For the B series, the maximum
magnitude of the model attenuation predictions and the time history
are quite similar to the measured test data. Because of the model as-
sumption that the initial cloud forms instantaneously at burst time,
the model attenuation peaks at burst time and declines thereafter.
The real cloud takes a finite time to form and build up to maximum at-
tenuation. The figures show that the test data attenuation reaches a
maximum about 1.5 seconds after burst time for the B series and slightly
less than a second for the E series. Part of the delay is artificial
and is due to the chart recorder time constant, and part is real and
is due to the cloud formation physics. The real part of the delay is
probably about one-half to three-quarters of a second. We could im-
prove the agreement between model and data in the first second after
burst by replacing the model instantaneous cloud formation with a finite
formation time. At present this level of detail is not considered
necessary. If at a later time some E-O system is sensitive to these
first-second details, then the model improvement can be implemented.

In the E series of tests, note the prominent spikes in the test
data. The shorter time constant of the E series allows these scintilla-
tions to be resolved. Dust clouds are turbulent and the spatial dis-
tribution of the lofted dust is inhomogeneous. The model predictions
are for the mean attenuation; there the agreement is quite reasonable.

The E series of tests is a good illustration of the importance of
the initial cloud dust mass loading and also verifies the ASL-DUST

39

model of this important parameter. In our model we assume the initial lofted dust mass is proportional to the soil mass that was in the apparent crater volume left by the explosion:

$$M_L = F_{CM} \rho_G \left(1 - F_{H_2O}\right) V_A \quad g \quad ,$$

where

M_L = total mass of dust grains lofted (g)

F_{CM} = fraction of mass in apparent crater that is lofted

ρ_G = bulk density of *in situ* soil (g cm^{-3})

F_{H_2O} = soil moisture fraction by weight

V_A = volume of apparent crater (cm^3).

The only model input parameters that change from event to event in the E series are the apparent crater volume and the wind speed and direction. But the winds are so light that they have essentially no effect upon the calculated attenuation during the few seconds of significant attenuation. Hence all model differences from event to event are due to the changing crater volumes. These E events were all static detonations of three 155-mm projectiles, tilted at 30 degrees. In events E5 and E6 the projectiles were buried 2 feet deep; in E7 and E8 they were 1 foot deep; and in E9 and E10 they were at the surface. As expected, the apparent crater volume increased with burial depth. Assuming the apparent crater was a segment of a sphere, the average crater volumes were 2.3 m^3 for E5 and E6, 1.5 m^3 for E7 and E8, and 0.54 m^3 for E9 and E10. Both the calculated and observed attenuations decrease with decreasing crater volumes.

Figures 26 through 35 show the data (Reference 11) and the model predictions for the NRL measured transmissions at visible (0.55 μm) and infrared (10.35 μm) wavelengths for events B1 through B8 and E1 and E2. An interesting phenomenon is exhibited by the data and mirrored by the model predictions. In passing through particulate regions, normally the longer wavelength signal experiences less attenuation (more transmission) than the shorter wavelength signal. But

40

both model and data show an inversion of this normal relationship on the recovering signal; the infrared is attenuated more than the visible. This rather unexpected result is due to the dust particle size distribution.

Figure 36 shows the Mie extinction efficiencies for the visible and infrared wavelengths as a function of dust particle diameter. For particles less than about 5 microns in diameter, the visible wavelength has a higher extinction than the infrared. But for particles in the size range from 5 to about 50 microns (in the region of the infrared extinction peak), the infrared has a higher extinction. For larger particles, both wavelengths approach the large particle extinction limit of 2; the extinctions are essentially equal.

Thus the relative visible/infrared extinction depends on the particulate size distribution. The carbon particles in the dust cloud are modeled as a log-normal size distribution with a mean diameter of 0.5 microns and standard deviation parameter of 2. For these small particles, the visible is considerably more attenuated than the infrared. And indeed the attenuations measured in the oil fire event (where we expect carbon to be a major particle constituent) confirmed the predicted attenuation behavior. But for dust clouds, carbon is normally a minor constituent. The spectral dependence of the dust clouds is a function of time. At very early times when many large particles are still aloft, we would expect the visible/infrared attenuations to be approximately equal. As fallout diminishes the larger particles, the size distribution of the particles aloft shifts toward the smaller particles. The dust particle size distributions measured and assumed for the model have a significant fraction of particles in the 5 to 50 μm inversion region. Thus after a short fallout time, inversion occurs; the infrared is attenuated more by the dust particles aloft than the visible. If we were to wait long enough, fallout would shift the particle size distribution far enough so that another inversion would occur and the visible would be attenuated more.

41

The spectral dependence of the dust cloud is not only a function of time, but is also a function of position within the cloud. Smaller particles tend to rise to the top of the cloud and the larger particles sink to the bottom of the cloud. Thus while a sight path through the top of the cloud might show the normal visible/infrared dependence, a sight path near the bottom could simultaneously exhibit the inverted dependence. The advantage in using the ASL-DUST method of many size groups and an exact Mie calculation is that the model automatically calculates the spectral dependence both as a function of time and position within the cloud. Simpler models using an average mass extinction coefficient cannot model these spatial and temporal dependencies.

In these visible/infrared model transmission comparisons, the wind plays a major role, in contrast to the comparisons at millimeter wavelengths. The recovery time of the signal is determined primarily by the wind blowing the cloud out of the sight path. The speed of the recovery is determined partly by the wind and partly by the model mass distribution and diffusion. The visible/infrared spectral dependence is determined by the initial assumed particle size distribution and fallout mechanisms. In general the comparisons are quite good. A real dust cloud is a lumpy, bumpy thing and the real wind is not steady in direction. In events B5 and B7 the signal essentially recovers and then another piece of dust cloud is blown by the sight path. In event B5, we chose the model wind direction so the model transmission was intermediate between the two cloud pieces. In B7 we chose to match the primary recovery. In event B8, the test data show that the B8 dust cloud was initially blown away from the line of sight, and about 8 minutes later the wind blew the B8 cloud or another cloud back through the line of sight.

MODEL COMPARISONS WITH DUGWAY TEST DATA

In November and December of 1977 six dust cloud tests were conducted at the Dugway Proving Ground. Dust clouds were generated using static TNT charges to simulate the detonation of high-explosive munitions

42

rounds. Table 7 shows the trial number, the munition simulated, and the amount of TNT used. In the previous report, Reference 1, we compared the initial dust cloud size and the time histories of the cloud width and height with the model predictions. Now we will compare the measured transmission at 3.4 μm with the model predictions.

TABLE 7. LIST OF EXPLOSIVES AND SIMULATED
ROUNDS FOR DUGWAY TESTS

Trial Number	Simulated Round	Weight of TNT (lb)
DPG-002-D1	81-mm mortar	3.5
DPG-002-D2	4.2-inch mortar	5.0
DPG-002-D3	105-mm tank HEP	6.75
DPG-002-D4	120-mm mortar	8.0
DPG-002-D5	155-mm artillery projectile	15.0
DPG-002-D6	8-inch artillery projectile	35.0

In the DIRT-1 test series, the static firings were centered about the line of sight. In the Dugway tests, the dust cloud was generated to one side of the lines of sight and the prevailing wind blew the cloud through the sight paths. Figure 37 shows the three sight paths and detonation points. D6 is on the opposite side of the site because of a shift in the wind direction. The DIRT-1 comparisons serve as a test of the model predictions for the cloud behavior near the formation point. The Dugway series will test the model predictions for the cloud parameters after wind transport over the ground.

The dust particle size distributions and the crater volumes were not measured in the Dugway tests. We will assume the Dugway soil to be similar to the DIRT-1 soil and use the DIRT-1 size distributions and crater scaling factors. We use the Dugway measured meteorology parameters of wind directions, wind profile power exponent, and

43

Pasquill stability factor. We choose an average wind speed which cor-
responds with the arrival of the dust cloud at the most distant sight
path. Table 8 shows the model input parameters.

TABLE 8. MODEL INPUT PARAMETERS FOR DUGWAY TESTS

Input Parameter	Trial Number					
	D1	D2	D3	D4	D5	D6
Yield (lb TNT)	3.5	5.0	6.75	8.0	15	35
Crater volume scaling factor $(m^3 [lb TNT]^{-1.111})$	0.064	0.06	0.06	0.04	0.04	0.032
Wind speed at 8 meters altitude $(m \ s^{-1})$	2.2	4.0	5.0	4.7	6.5	4.7
Wind azimuth (deg)	208	204	171	175	157	344
Wind vertical profile power exponent	0.06	0.08	0.09	0.07	0.15	0.16
Pasquill stability factor	C	D	D	D	D	C
Note: Model azimuth = true azimuth - 145°.						

Figures 38 through 55 show the data (Reference 4) and the model
comparisons. Any individual dust cloud has a very irregular structure.
The model cloud has a very regular structure which supposedly repre-
sents the average of a large number of real clouds. So our model pre-
dictions can be expected to vary about the measured data but to agree
on the average. For D1 the model cloud is early in reaching row O but
is late in reaching row M; for both rows the width of the cloud and
the minimum transmission agree approximately with the data. The other
tests show variations between model and data, but on the average the
comparisons are quite reasonable.
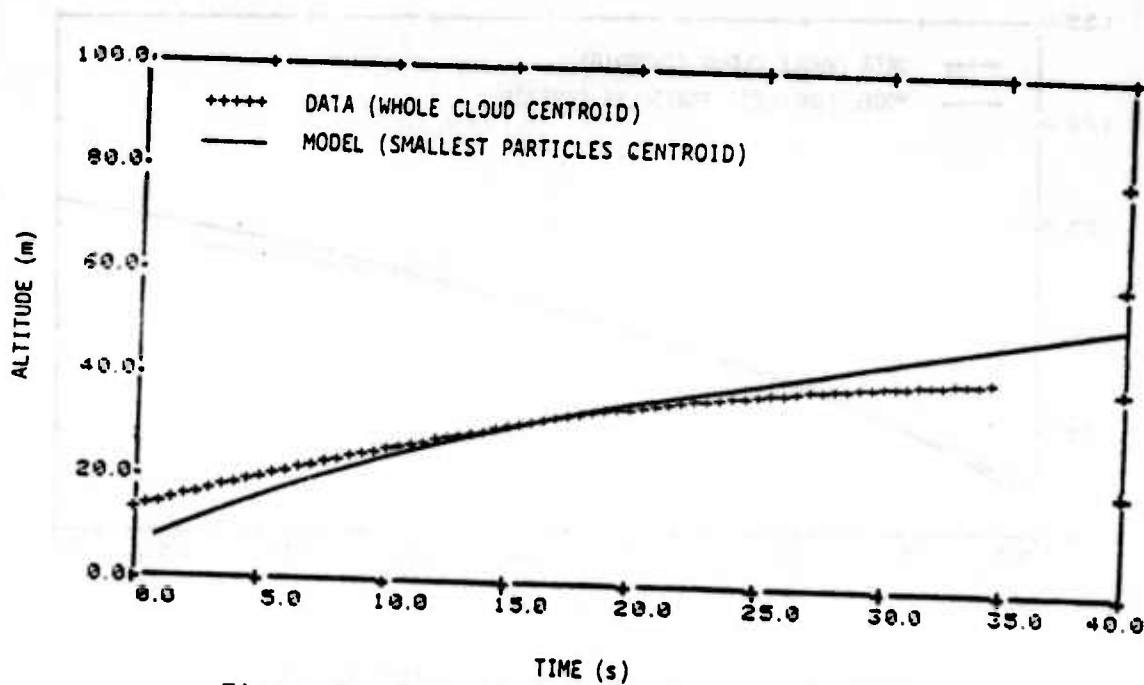
Figure 7. Dust cloud centroid altitude for event B2.
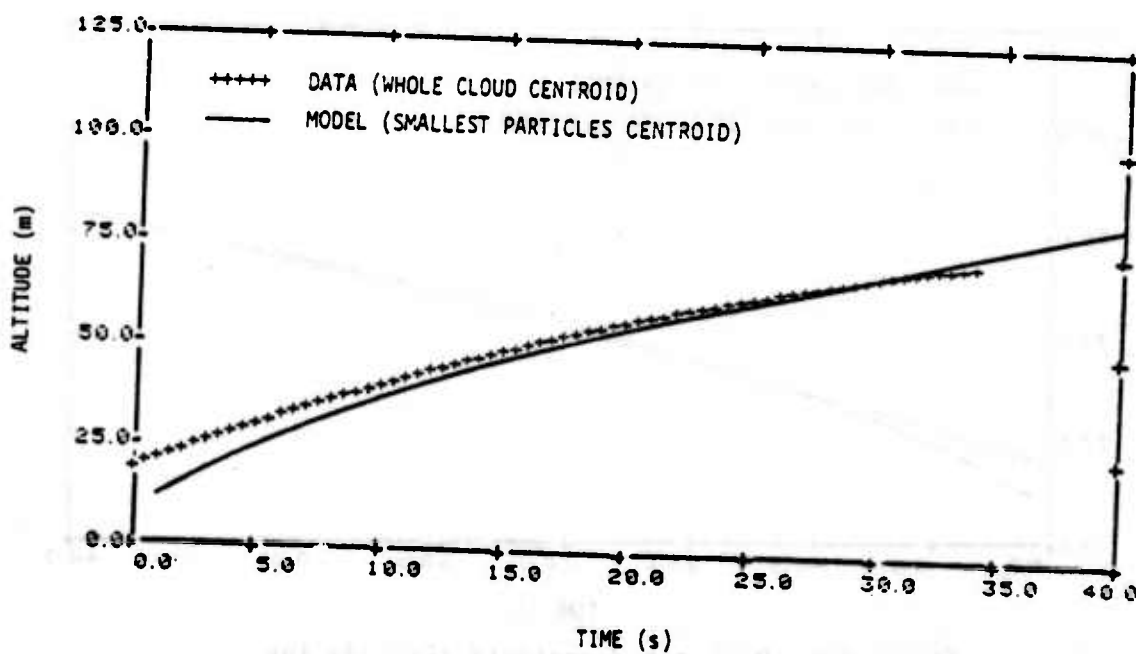
Figure 8. Dust cloud centroid altitude for event B3.
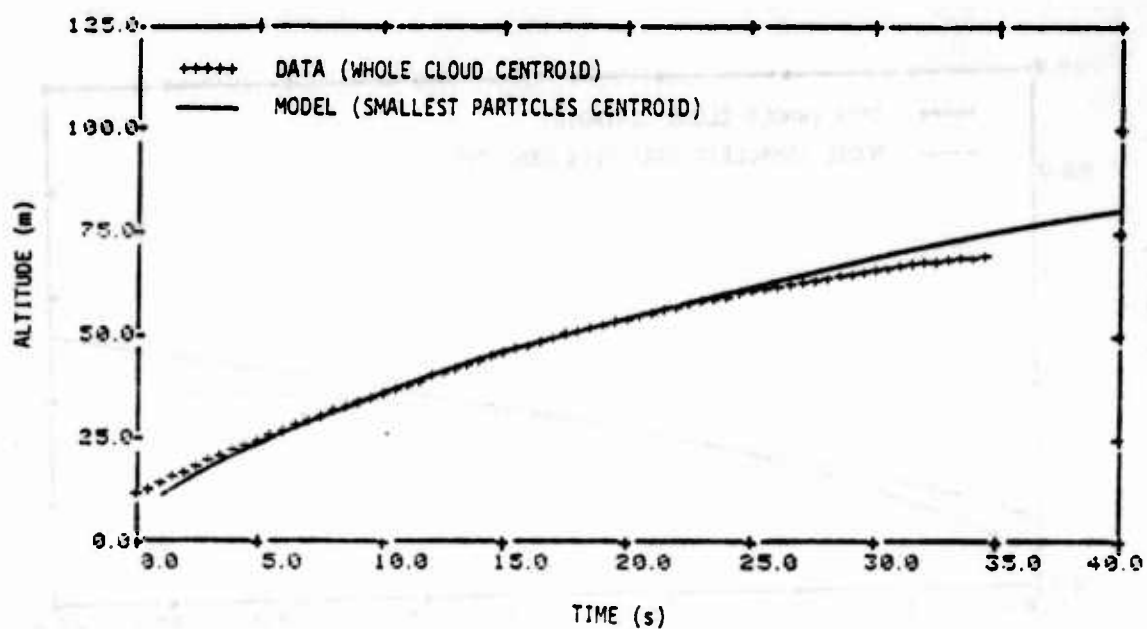
Figure 9. Dust cloud centroid altitude for event B4.
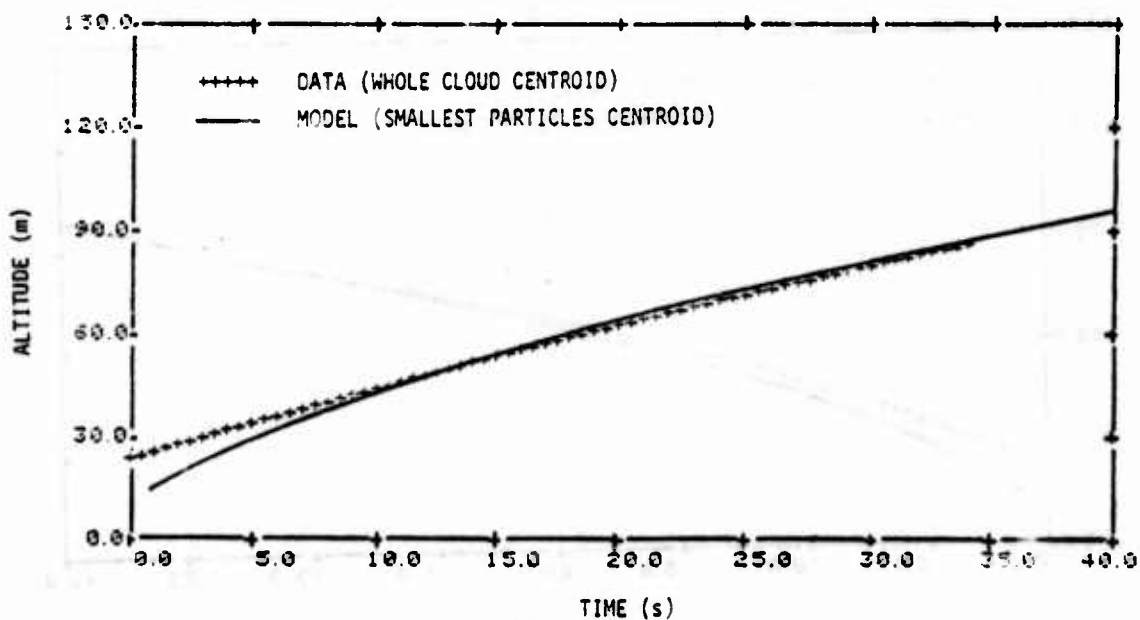
Figure 10. Dust cloud centroid altitude for event B5.

46
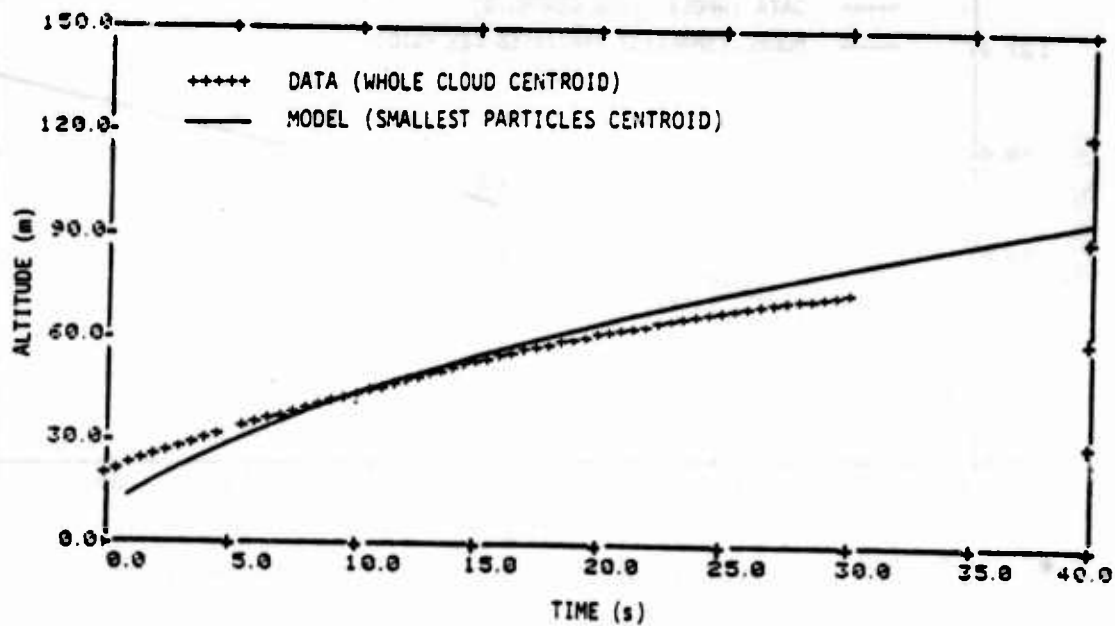
Figure 11. Dust cloud centroid altitude for
event B6.
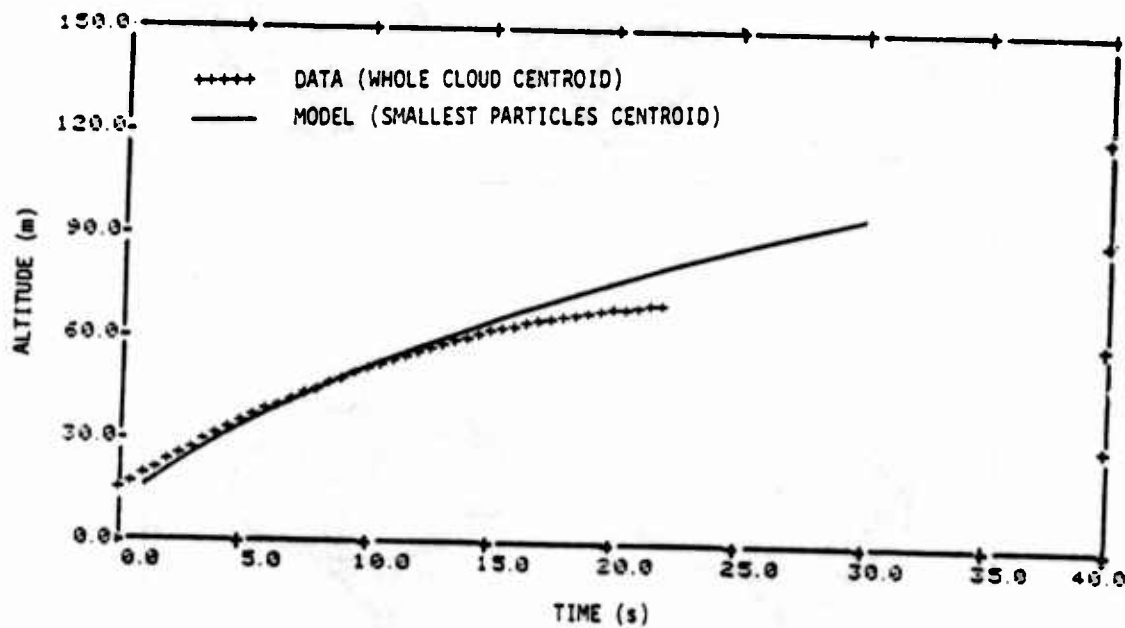
Figure 12. Dust cloud centroid altitude for
event B7.
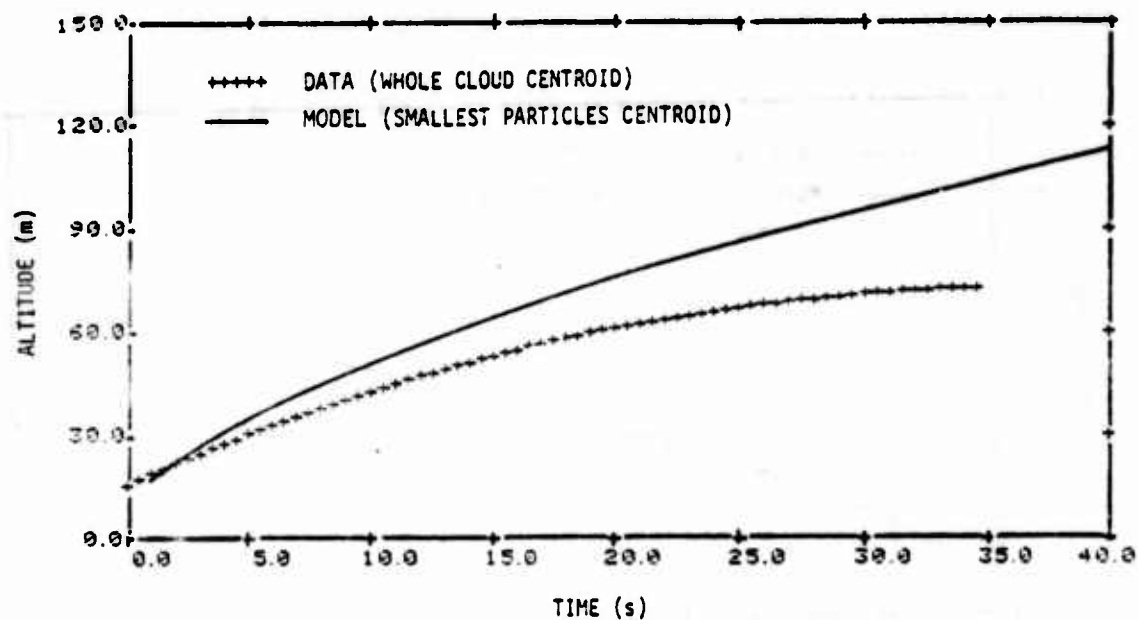
Figure 13. Dust cloud centroid altitude for event B8.
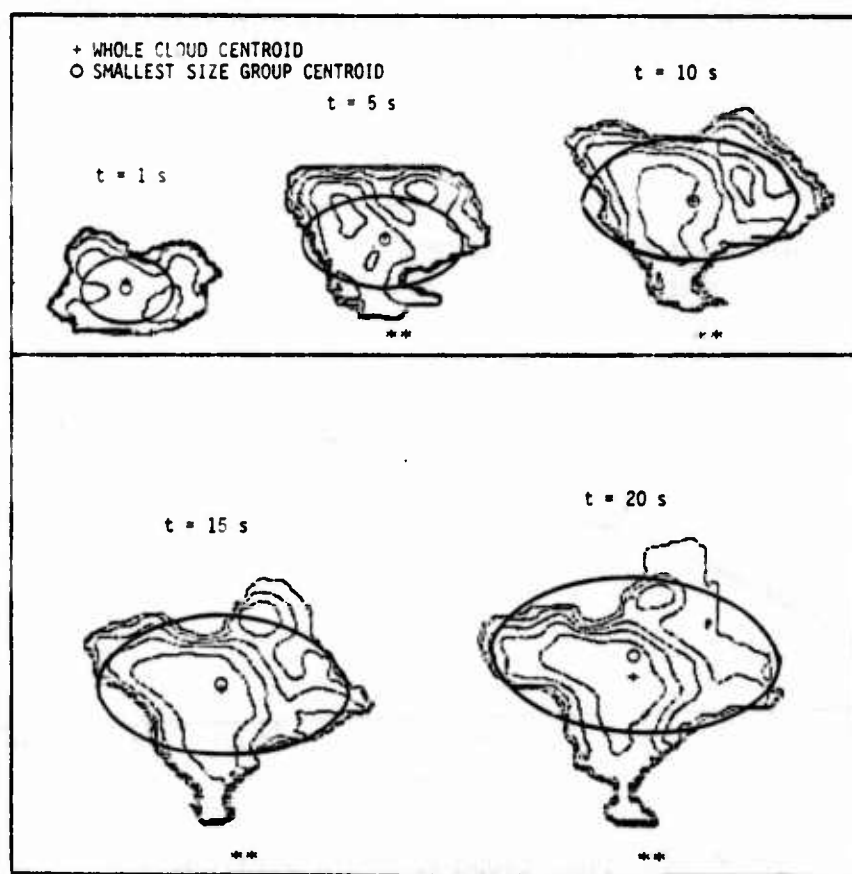
Figure 14. Comparison of cloud geometry for event B7.
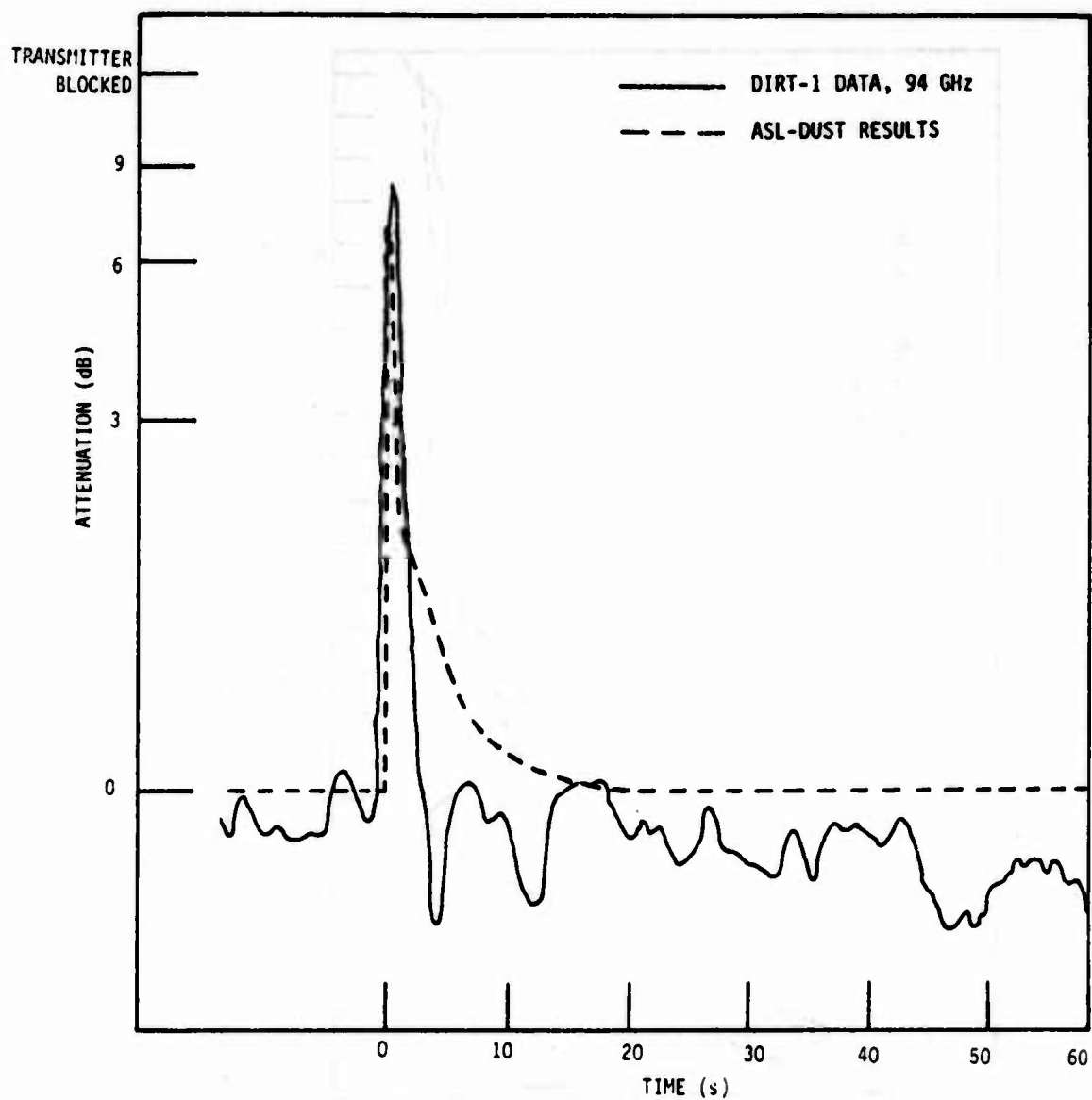
Figure 15. Attenuation at 94 GHz for event B4.
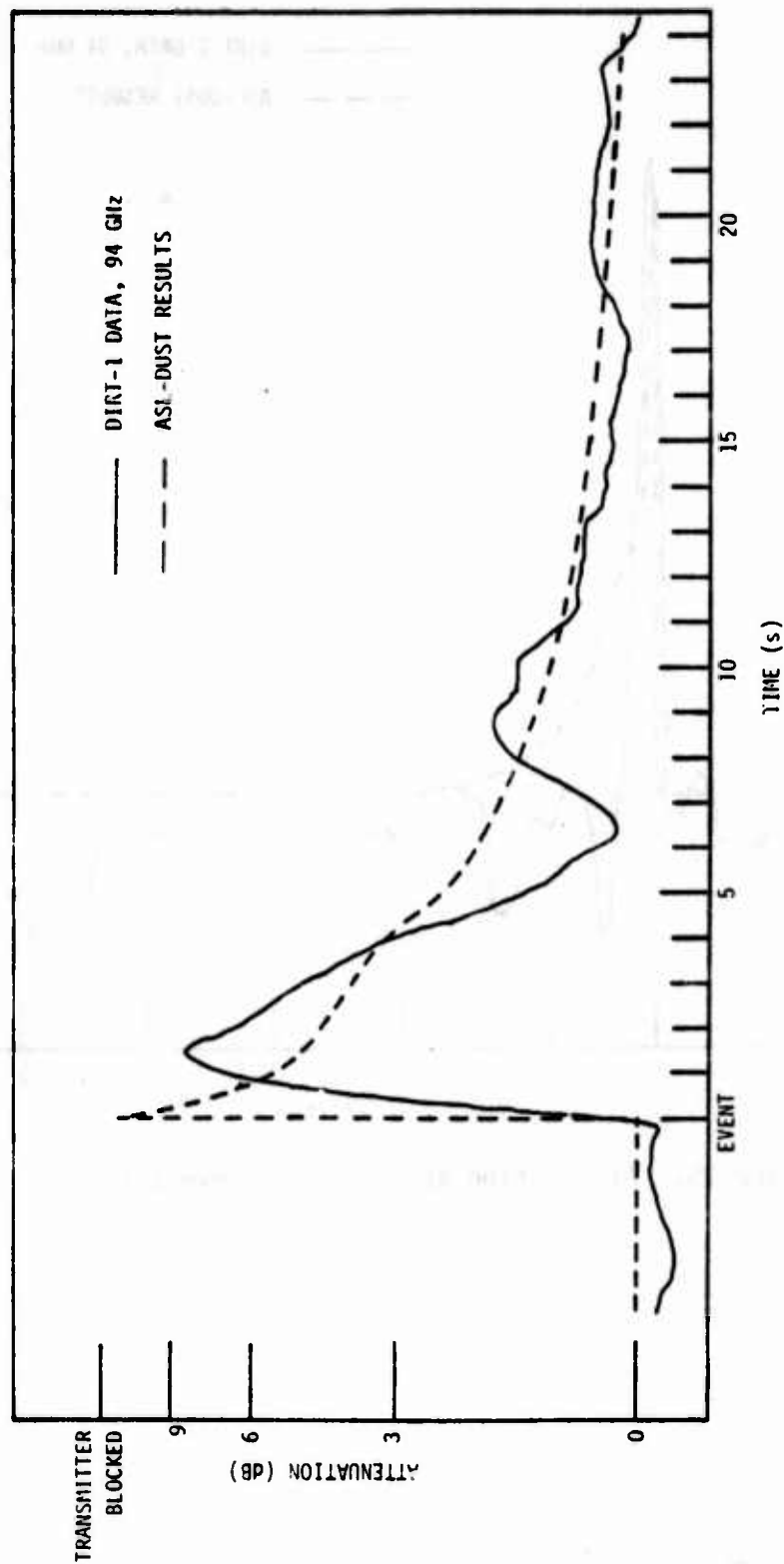
Figure 16. Attenuation at 94 GHz for event B5.

50
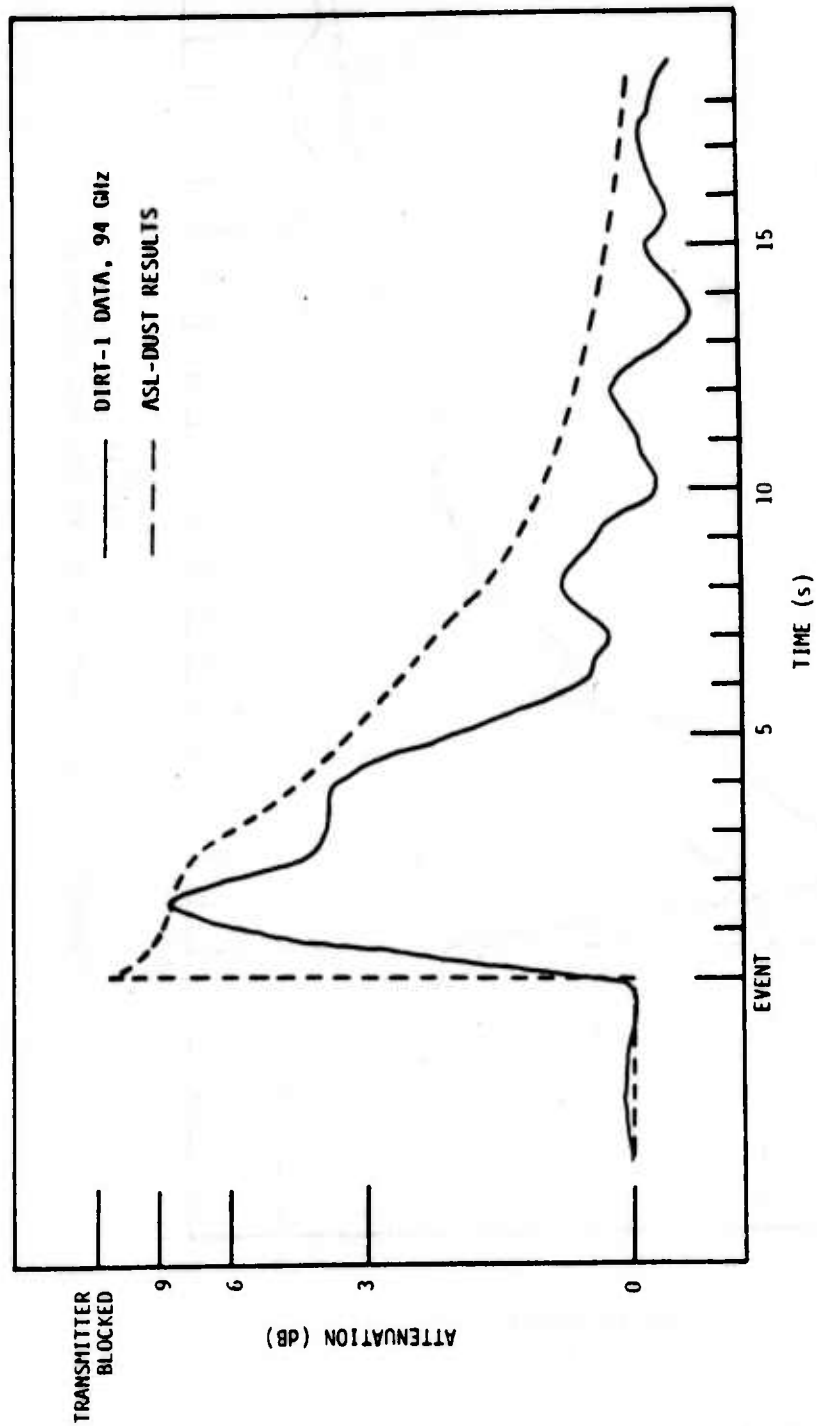
Figure 17. Attenuation at 94 GHz for event B6.

51
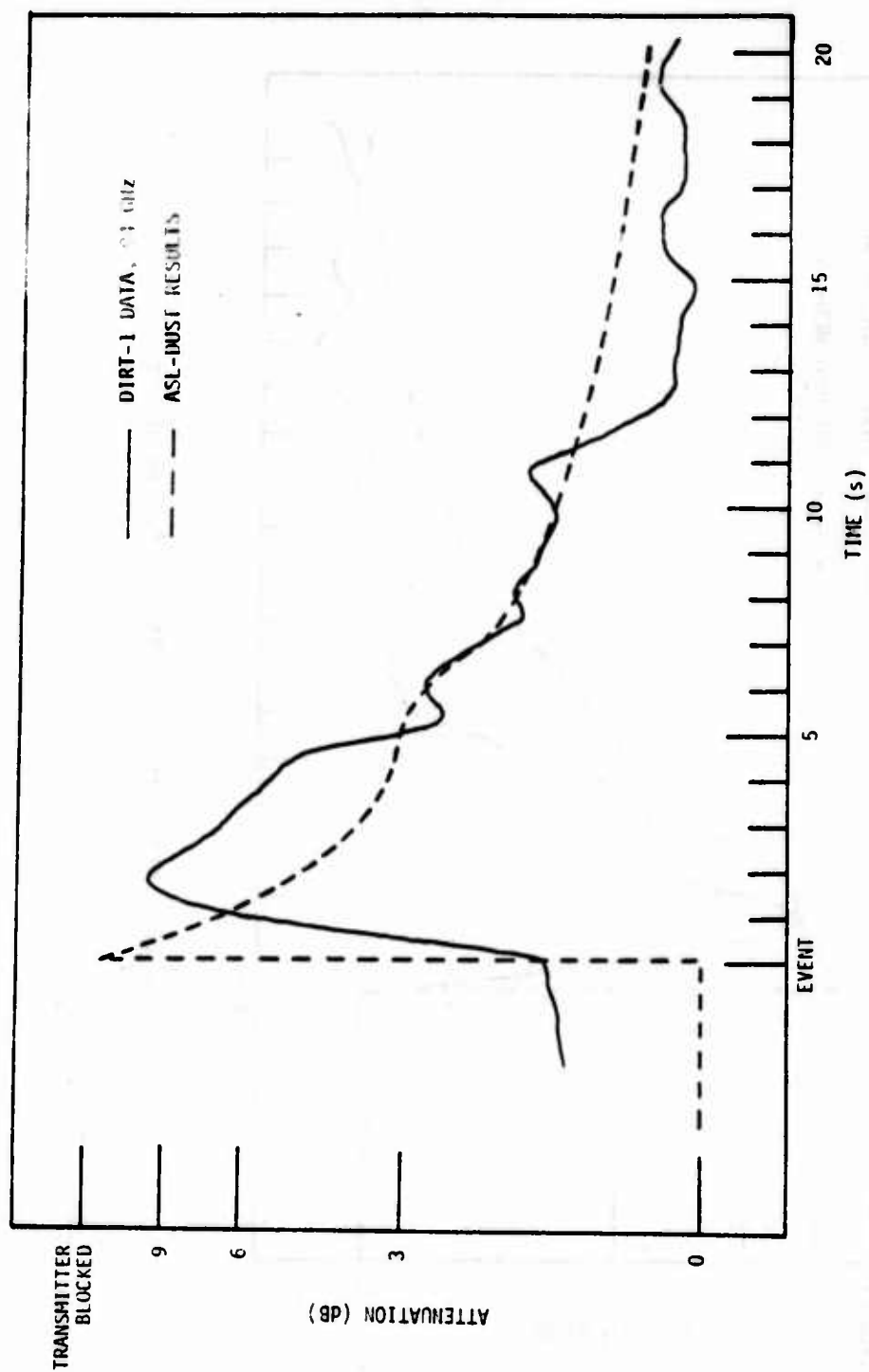
Figure 18. Attenuation at 94 GHz for event B7.

DIRT-1 DATA, 94 GHz
ASL-DUST RESULTS

TRANSMITTER BLOCKED

ATTENUATION (dB)

TIME (s)

EVENT

52
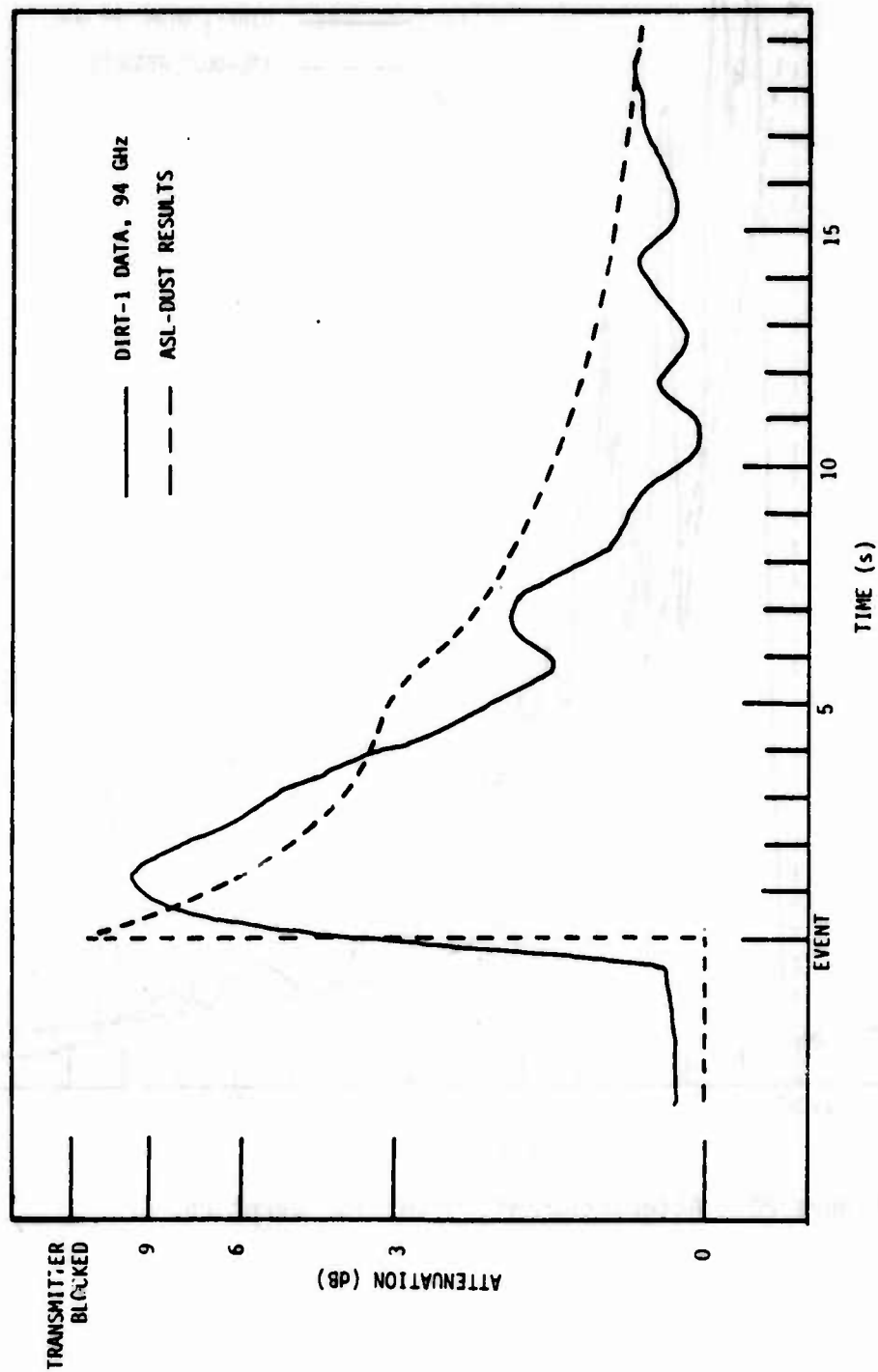
Figure 19. Attenuation at 94 GHz for event B8.

53
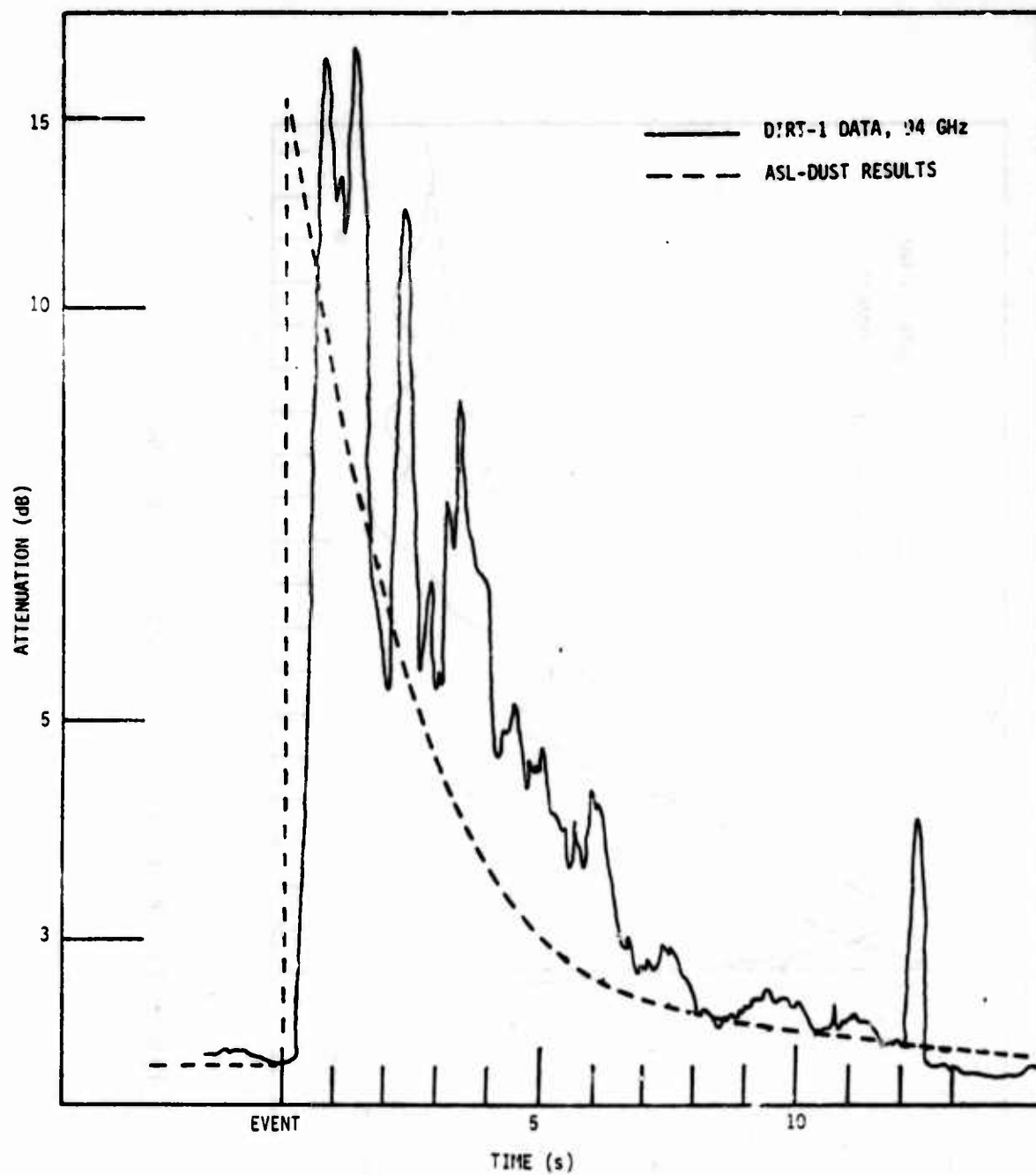
Figure 20. Attenuation at 94 GHz for event E5.
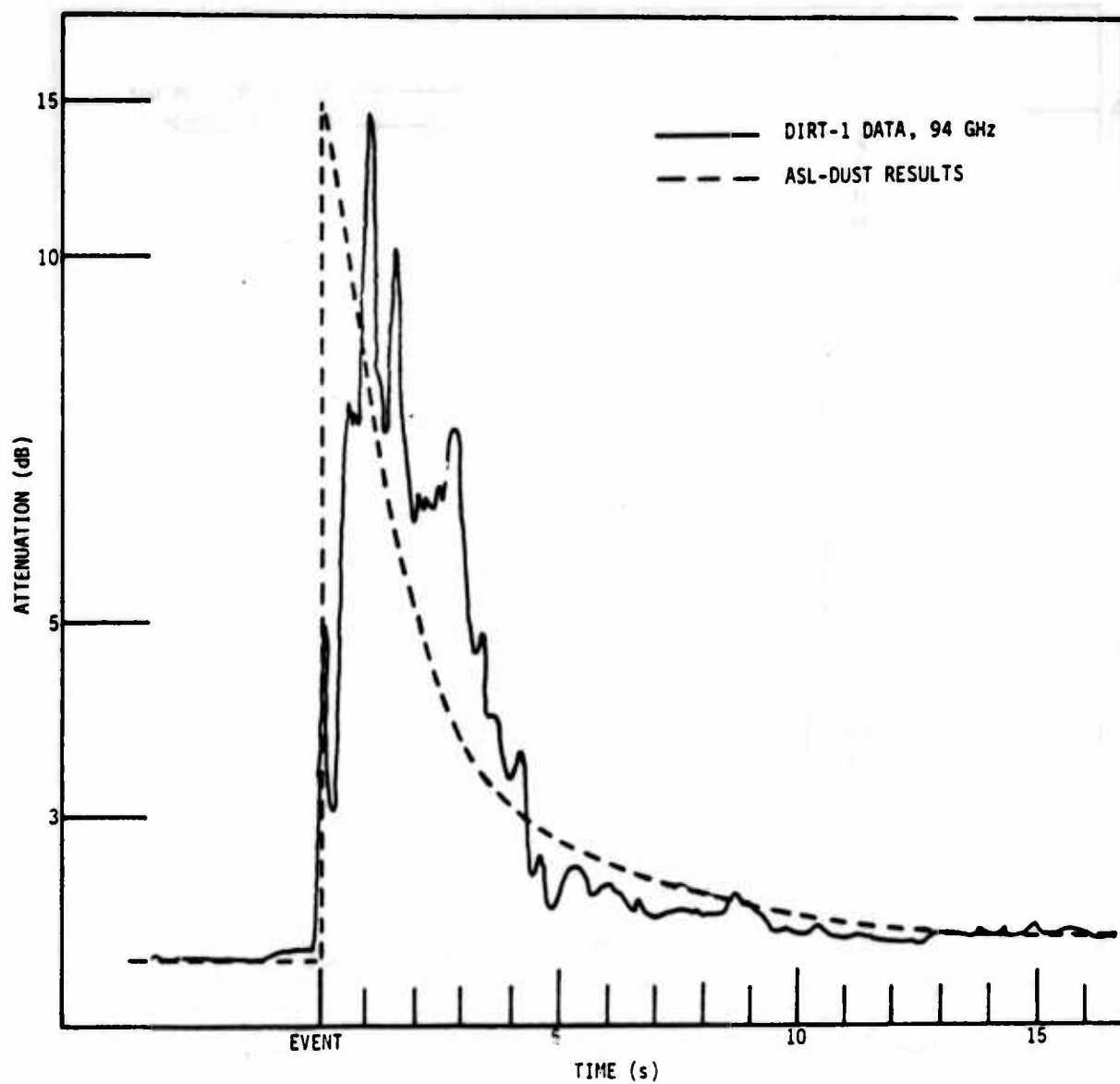
Figure 21.   Attenuation at 94 GHz for event E6.
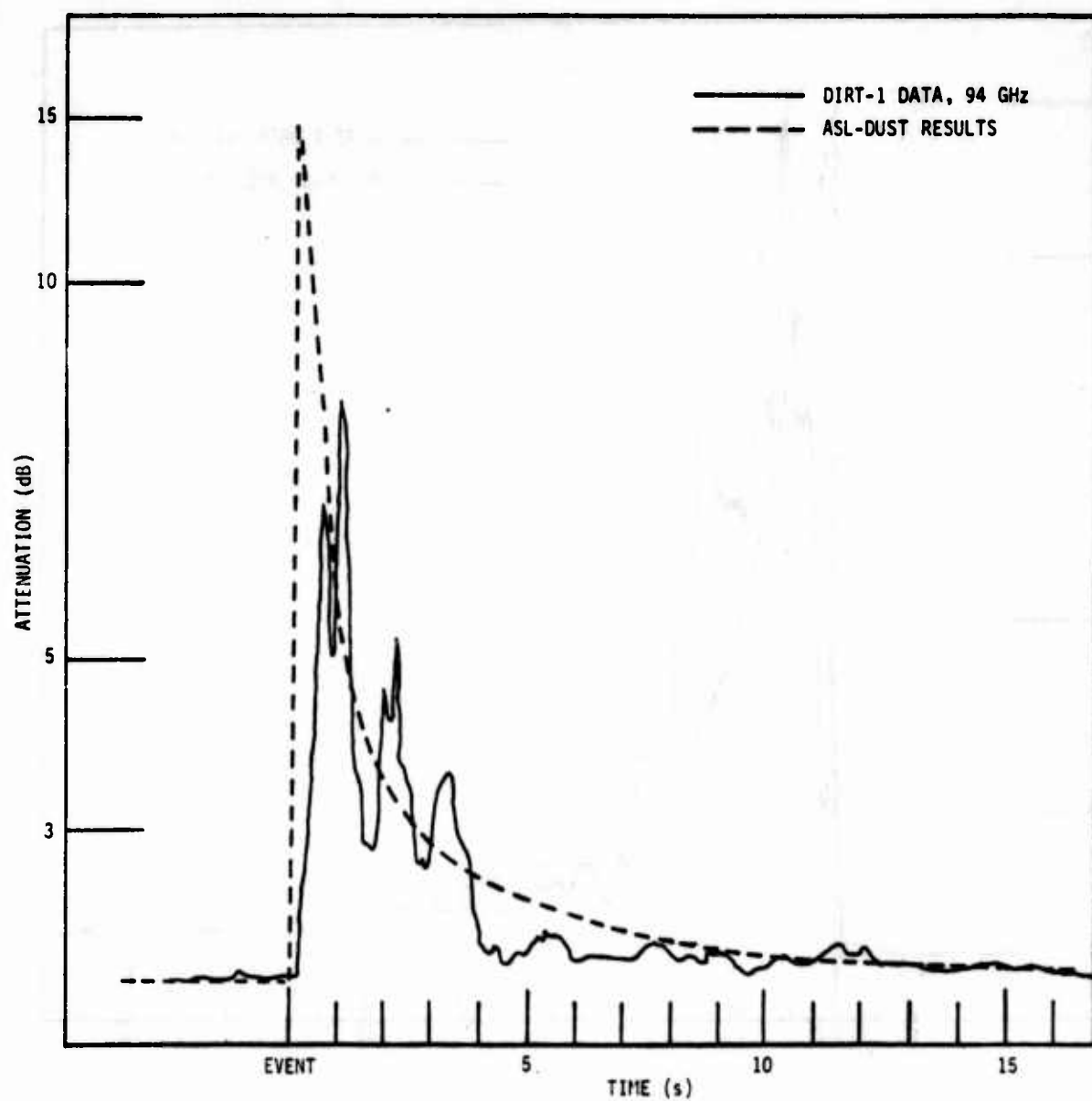
Figure 22. Attenuation at 94 GHz for event E7.
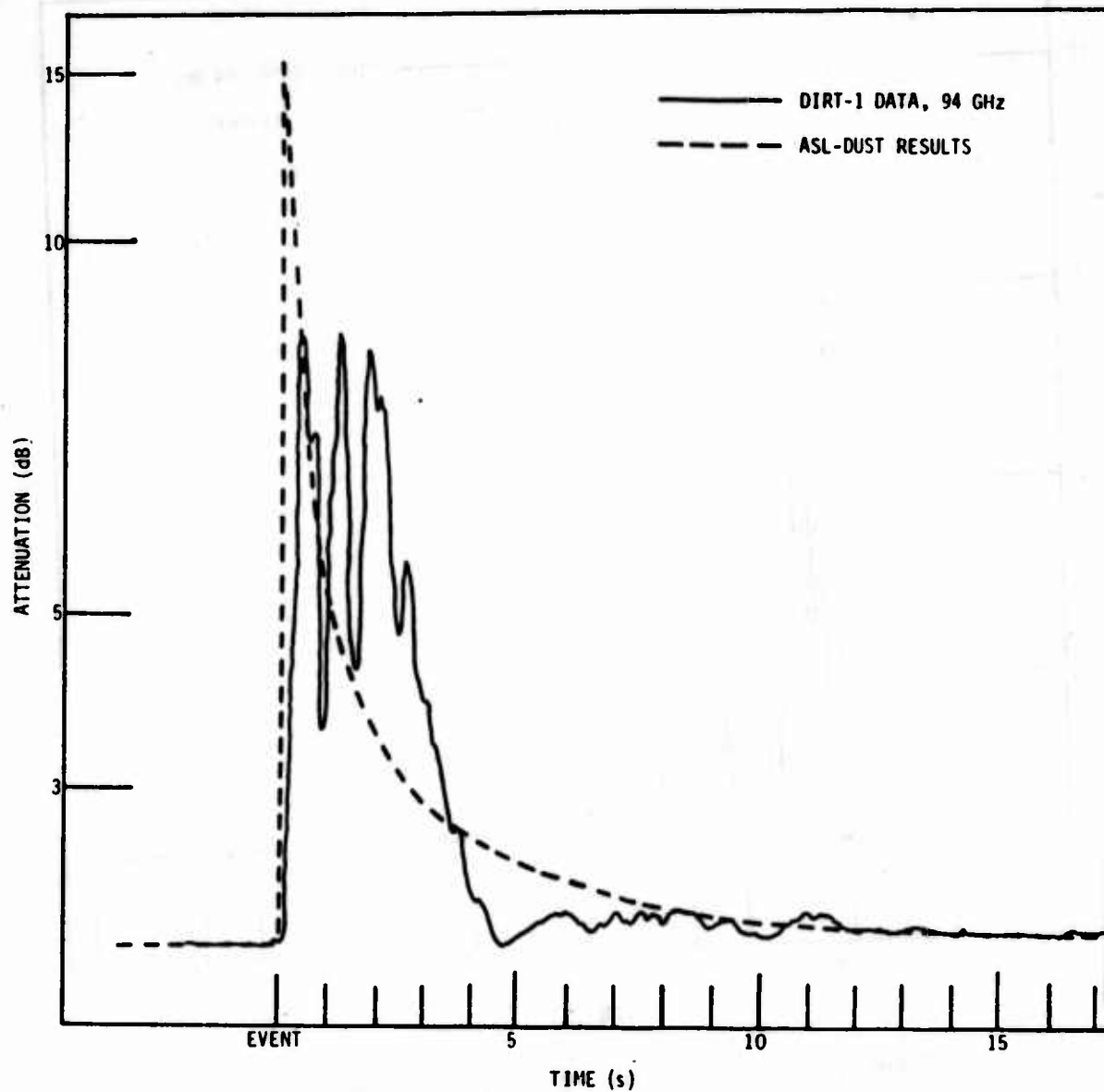
Figure 23. Attenuation at 94 GHz for event E8.
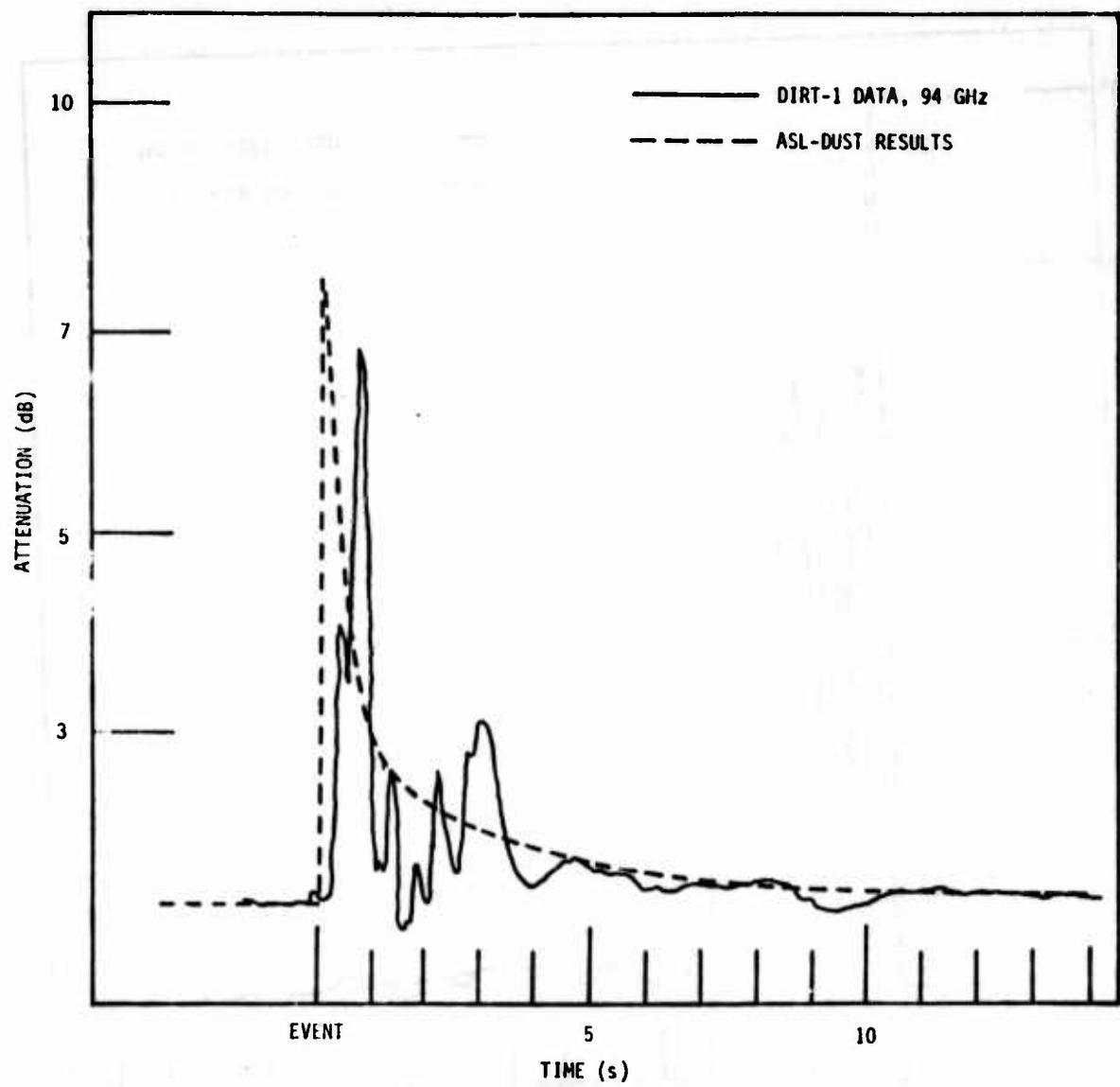
Figure 24. Attenuation at 94 GHz for event E9.
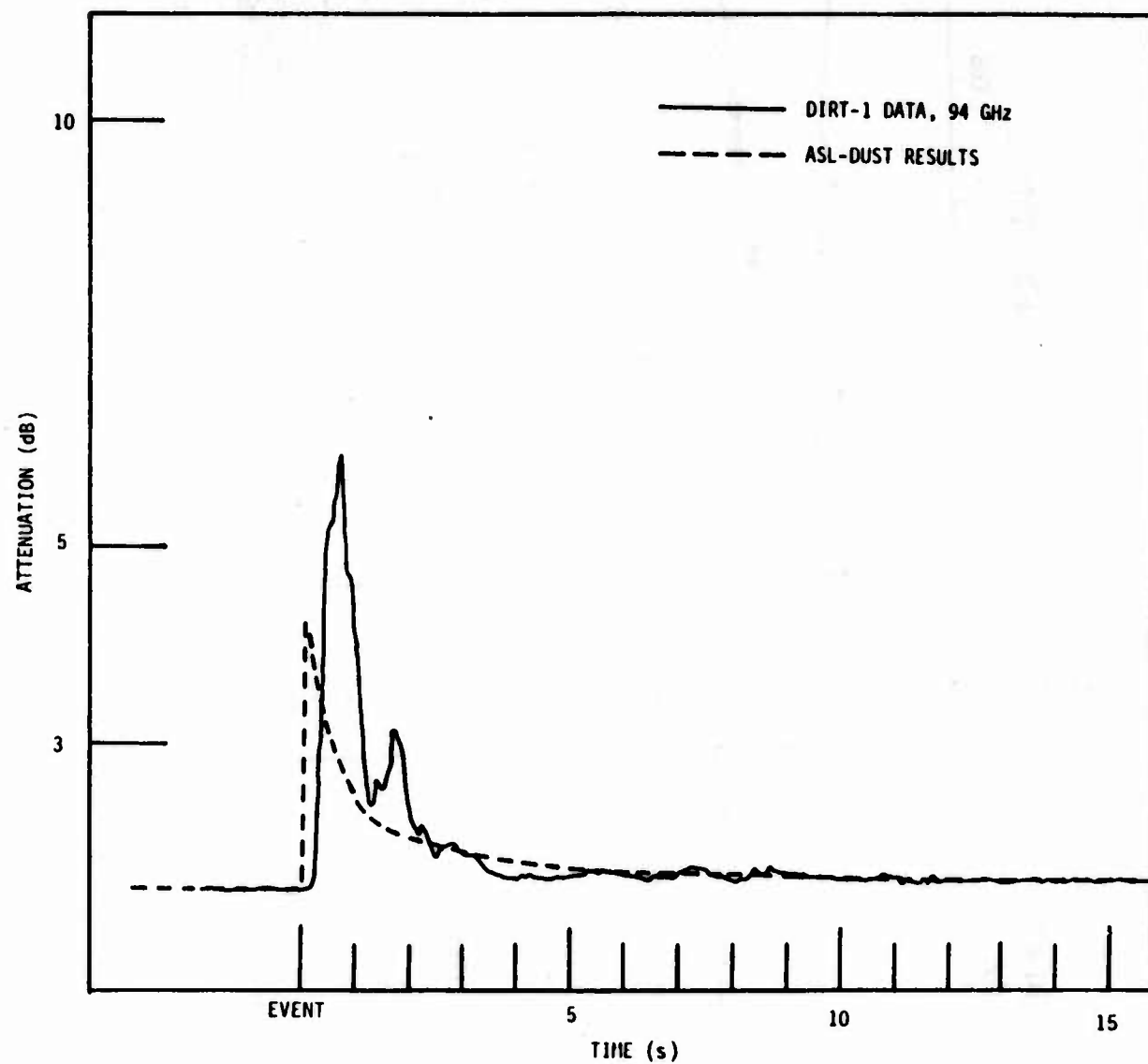
Figure 25.   Attenuation at 94 GHz for event E10.
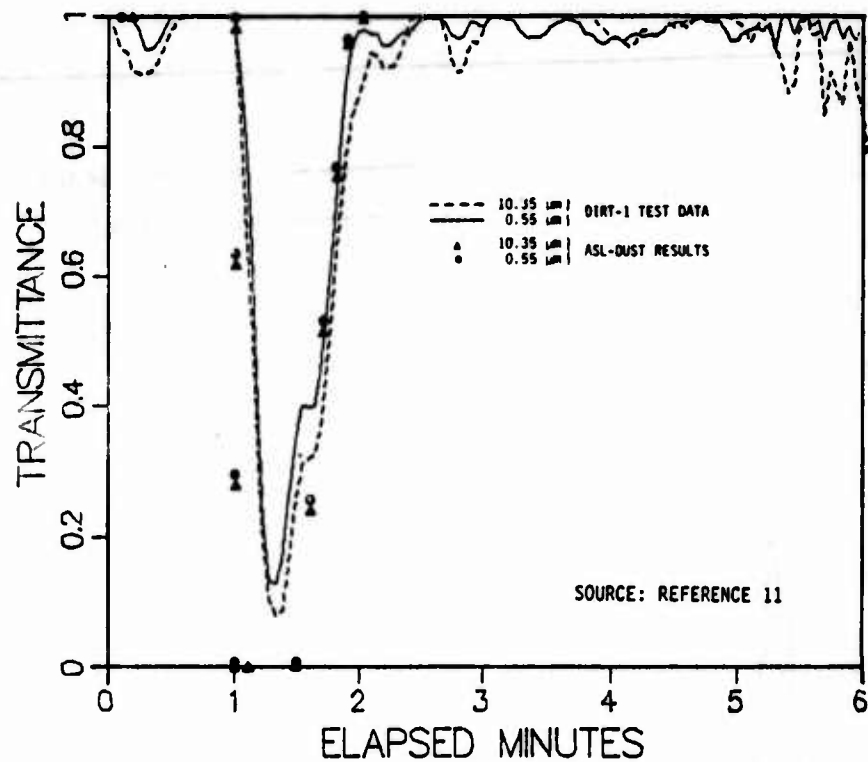
Figure 26. Transmittance at 10.35 μm and 0.55 μm for event B1.
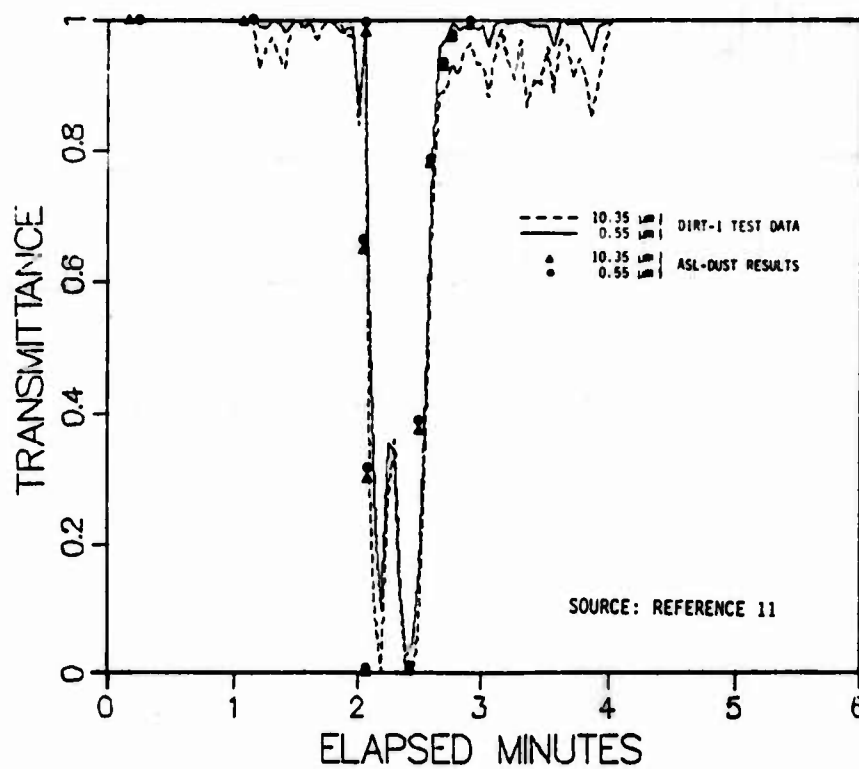
Figure 27. Transmittance at 10.35 μm and 0.55 μm for event B2.

60
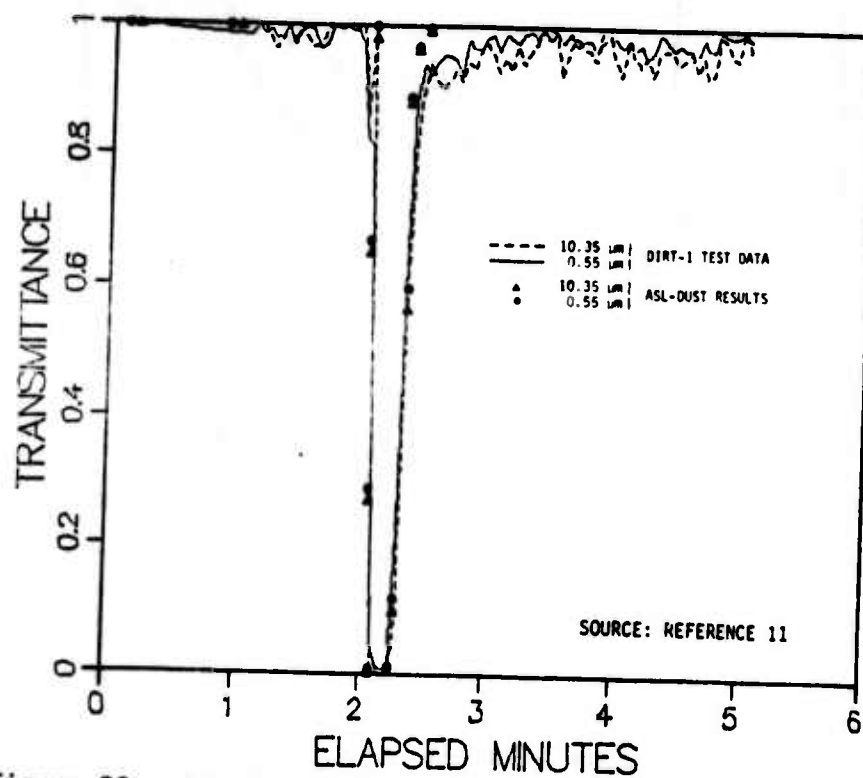
Figure 28. Transmittance at 10.35 μm and 0.55 μm for event B3.
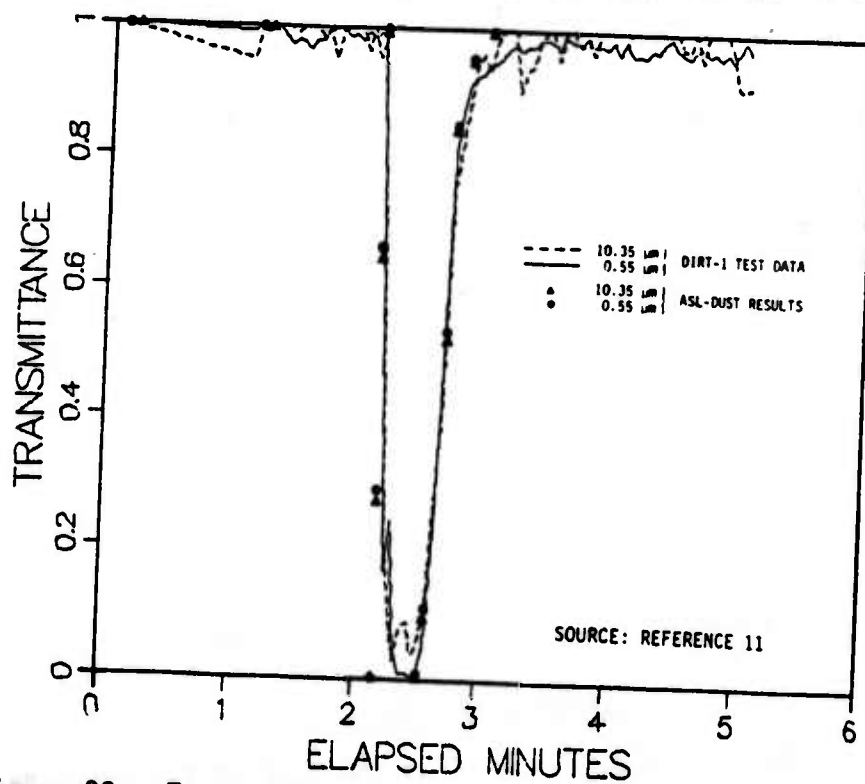
Figure 29. Transmittance at 10.35 μm and 0.55 μm for event B4.
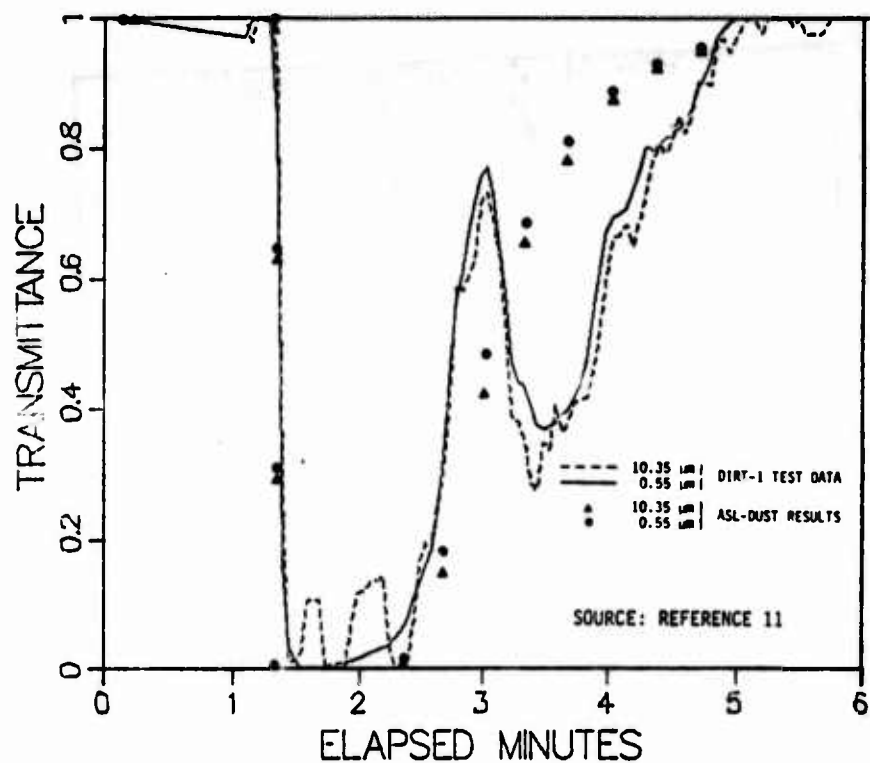
Figure 30. Transmittance at 10.35 μm and 0.55 μm for event B5.
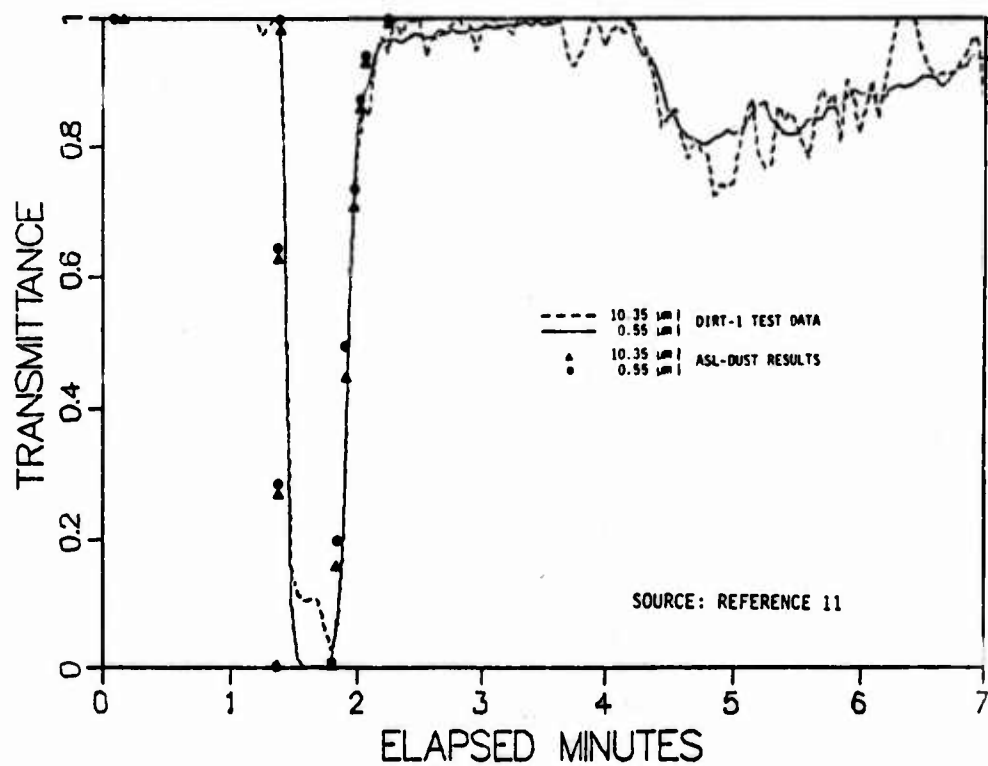
Figure 31. Transmittance at 10.35 μm and 0.55 μm for event B6.
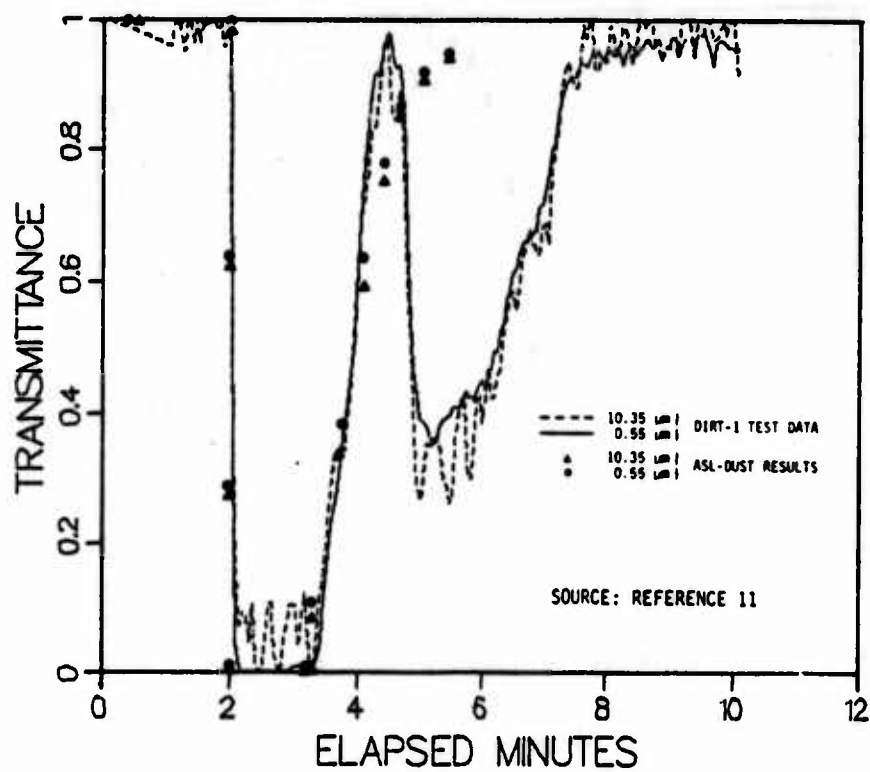
Figure 32. Transmittance at 10.35 μm and 0.55 μm for event B7.
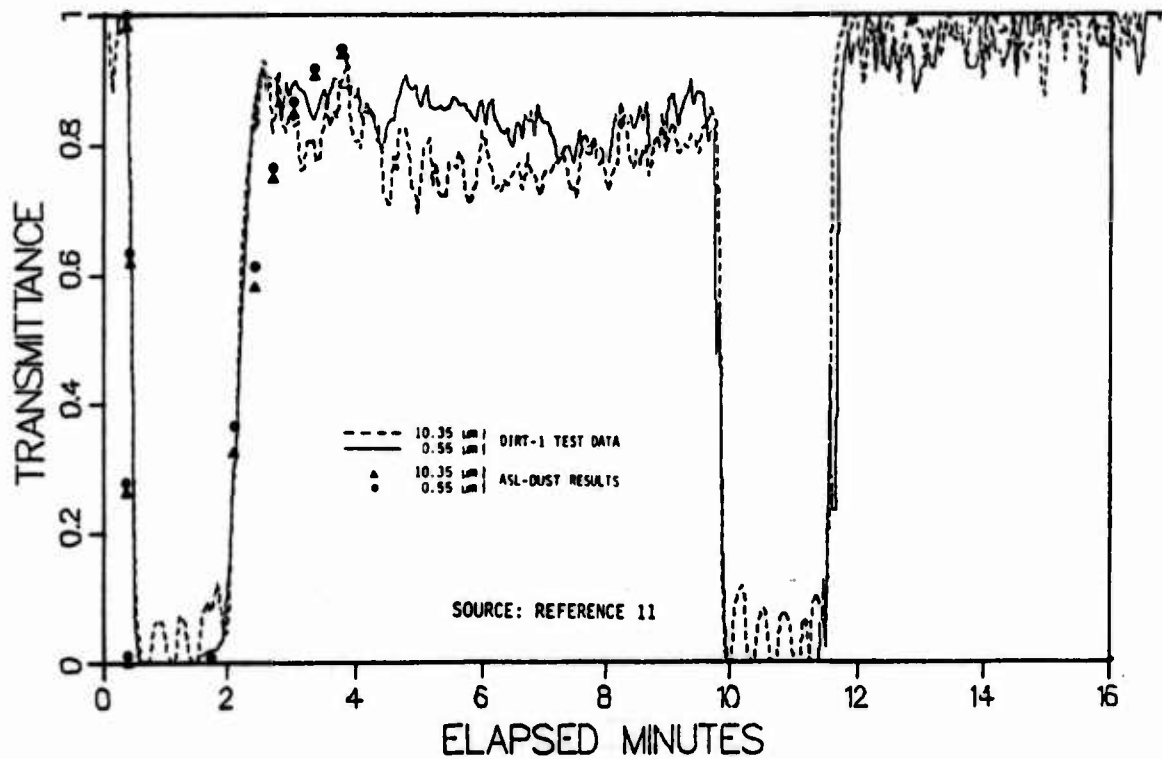
Figure 33. Transmittance at 10.35 μm and 0.55 μm for event B8.
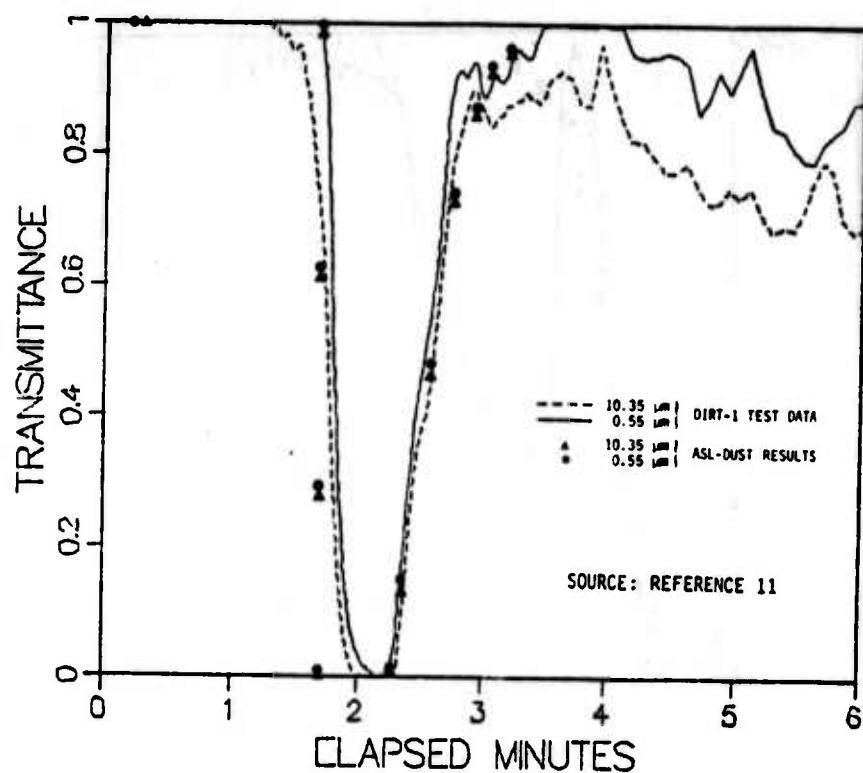
Figure 34. Transmittance at 10.35 μm and 0.55 μm for event E1.
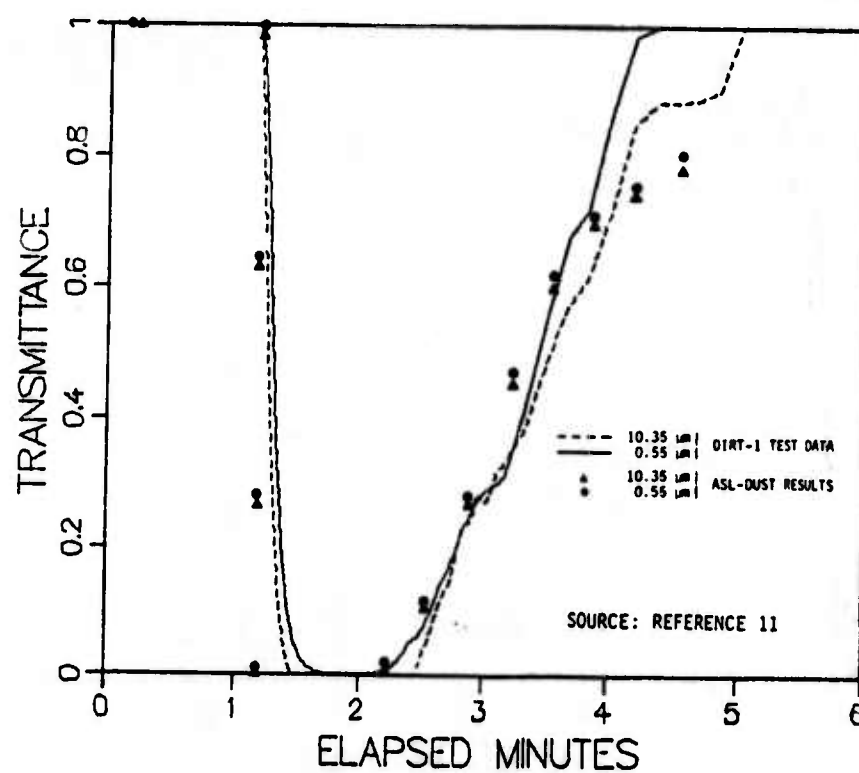
Figure 35. Transmittance at 10.35 μm and 0.55 μm for event E2.
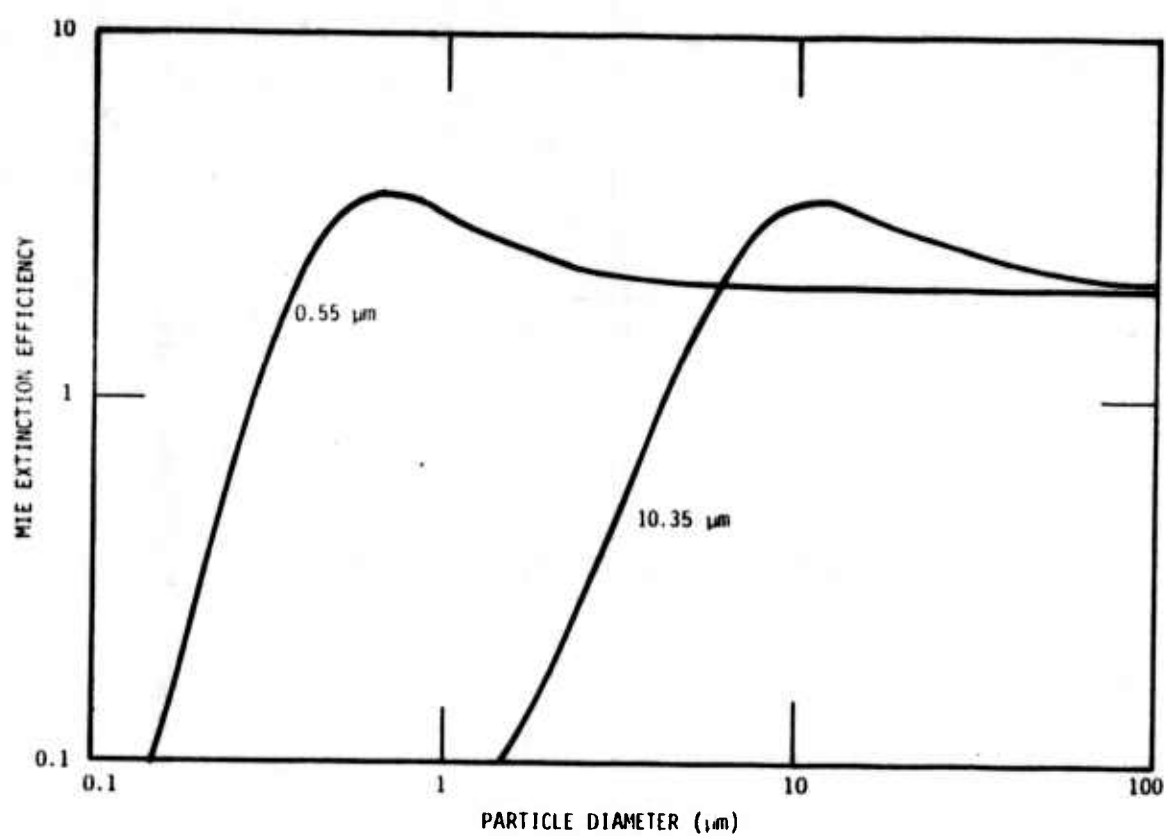
Figure 36.   Mie extinction efficiencies for visible and
             infrared wavelengths.
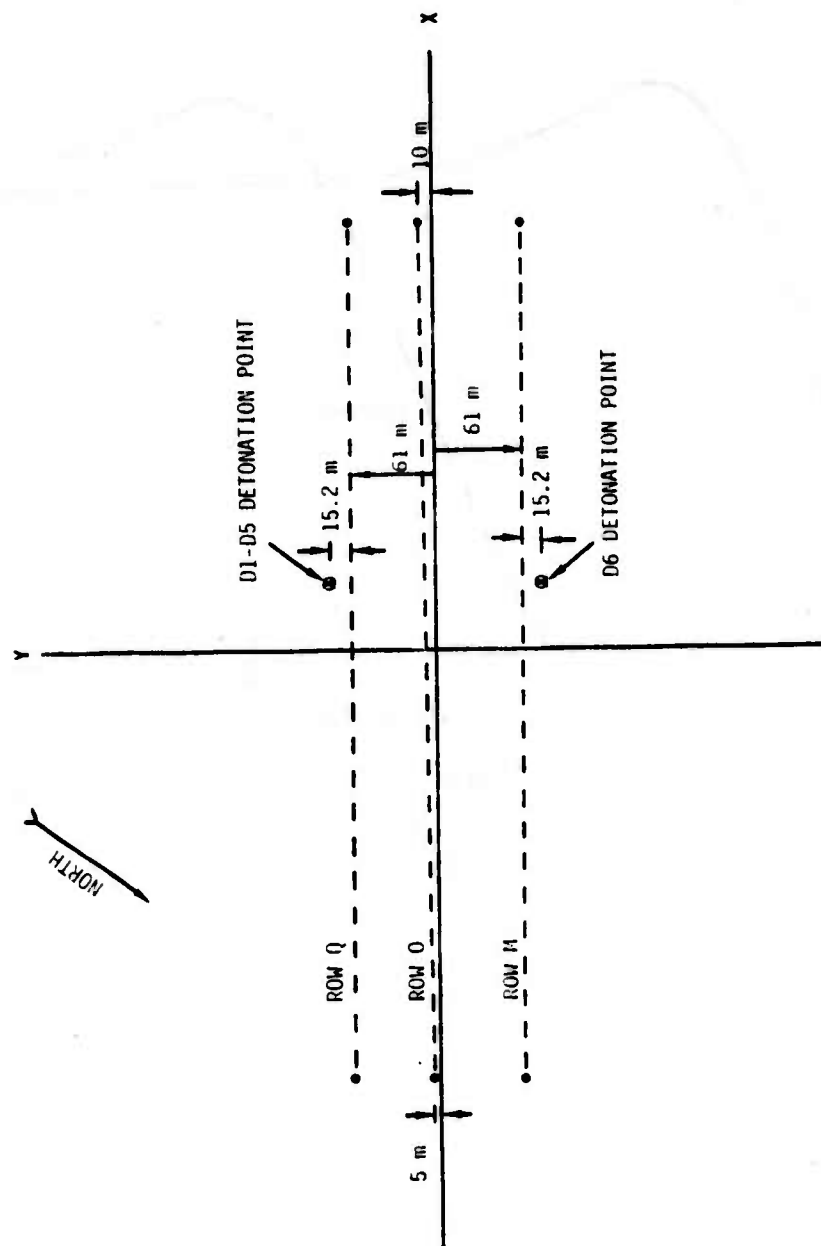
Figure 37. Site geometry for Dugway 3.4 μm measurements.
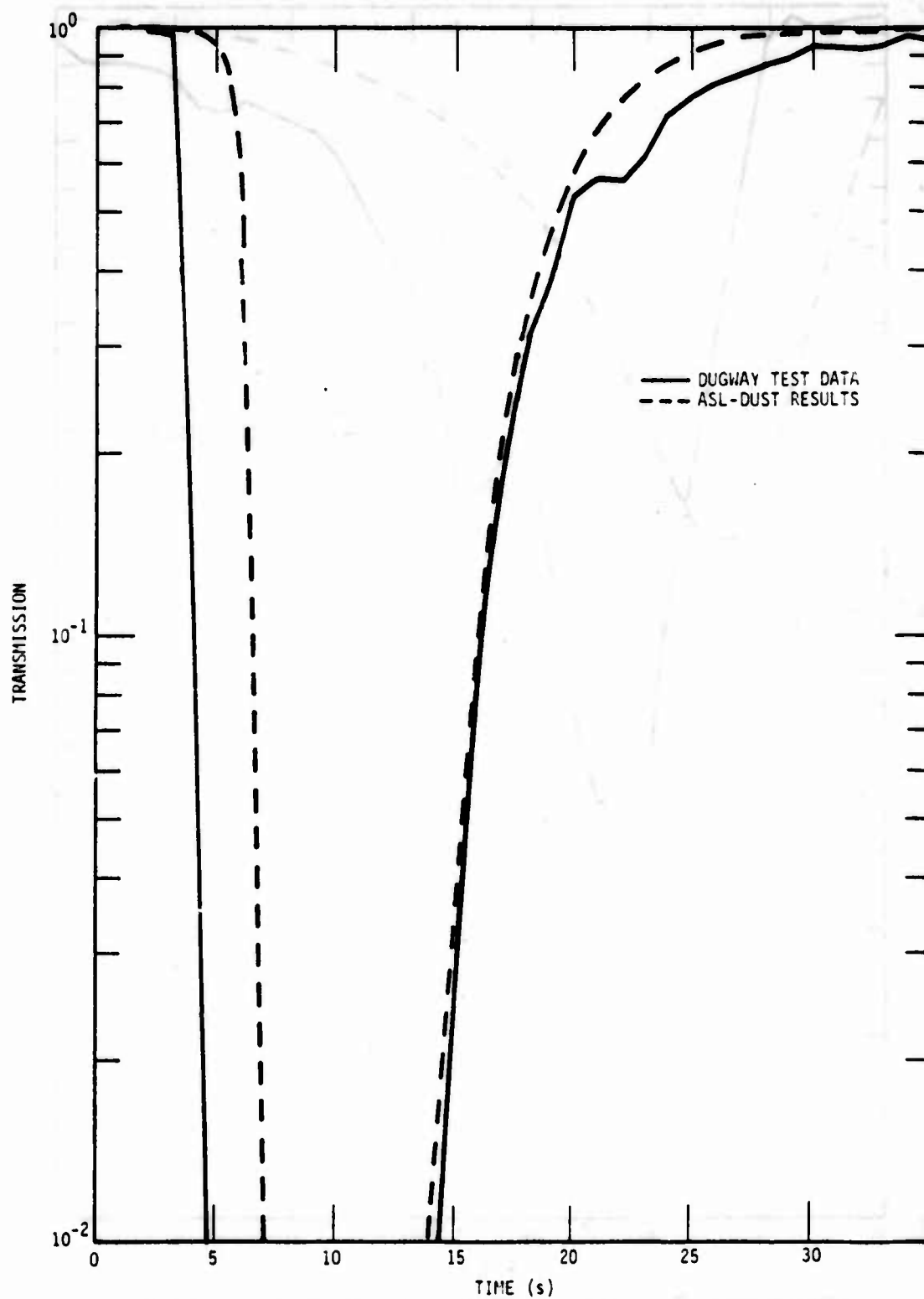
Figure 38. Transmission at 3.4 µm for event D1, row Q.
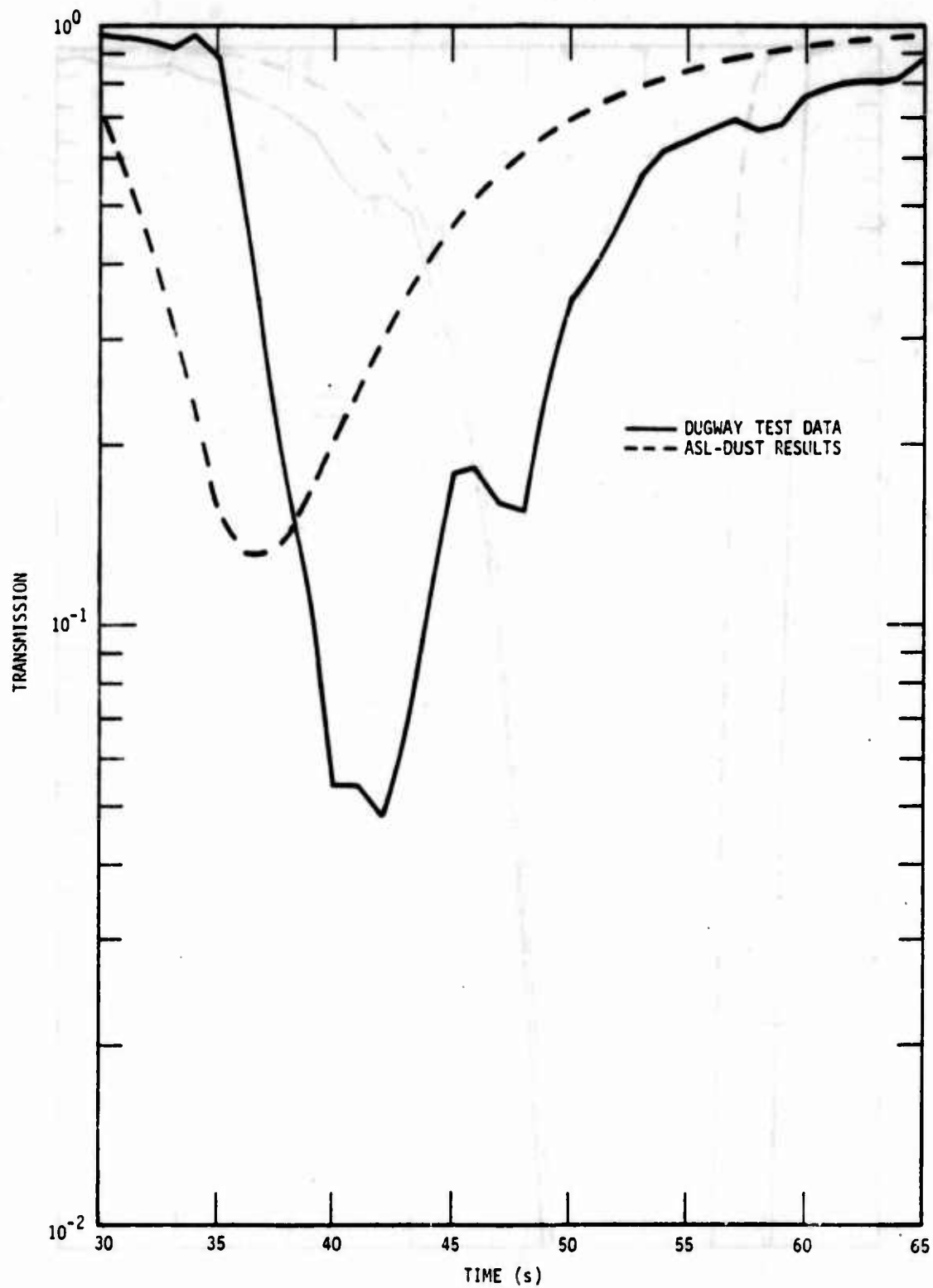
Figure 39.   Transmission at 3.4 μm for event D1, row 0.
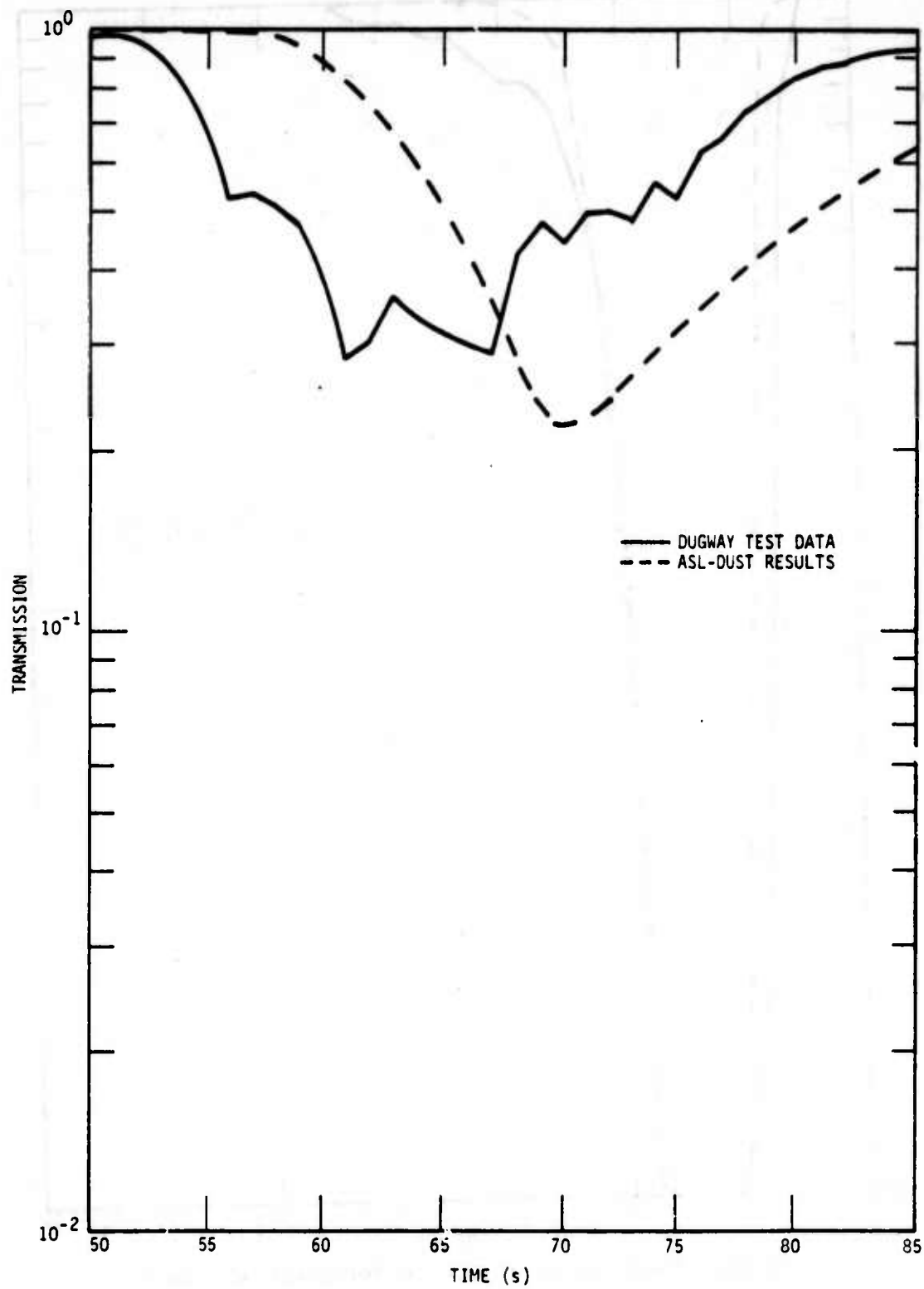
Figure 40.   Transmission at 3.4 μm for event D1, row M.
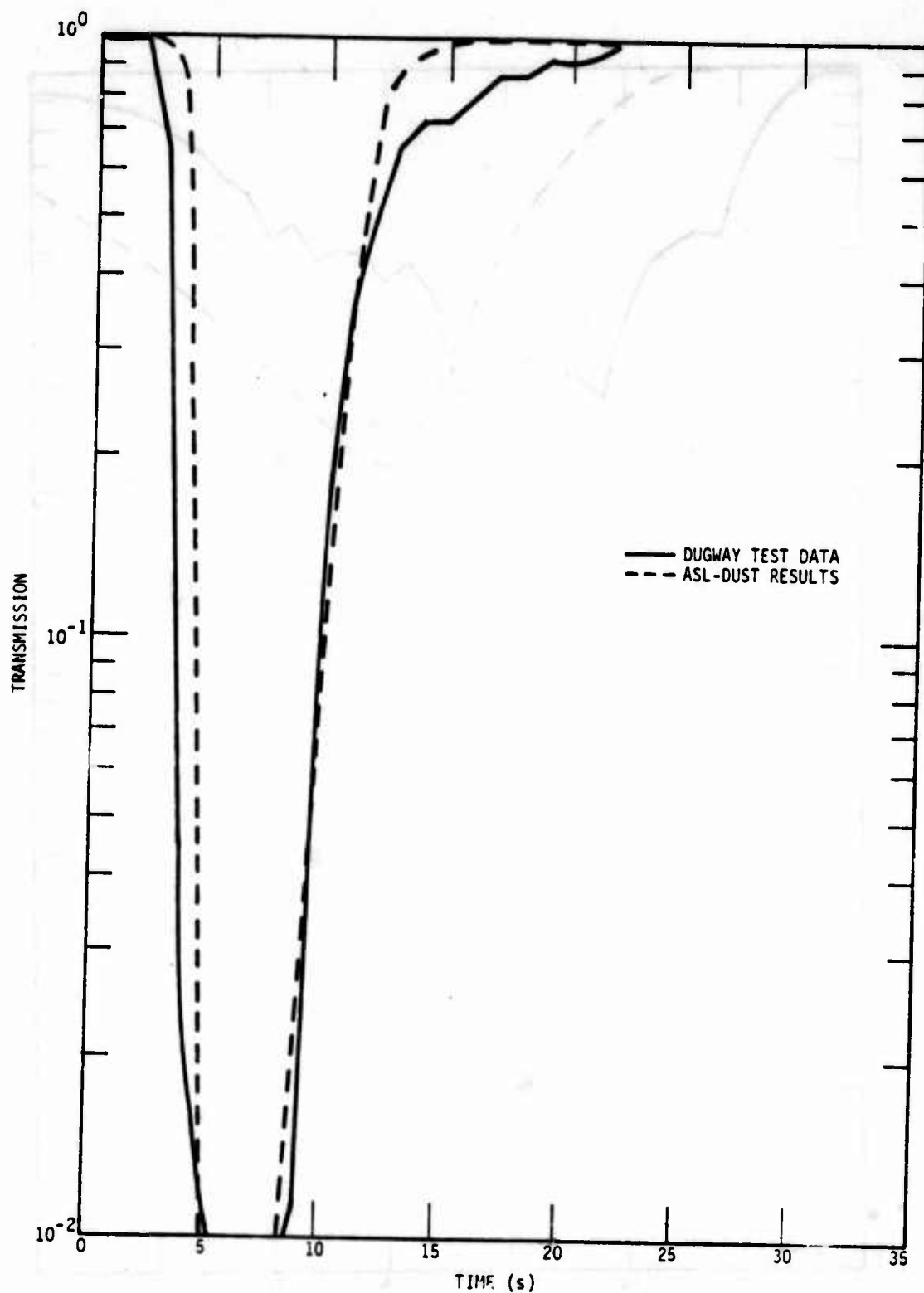
Figure 41. Transmission at 3.4 µm for event D2, row Q.
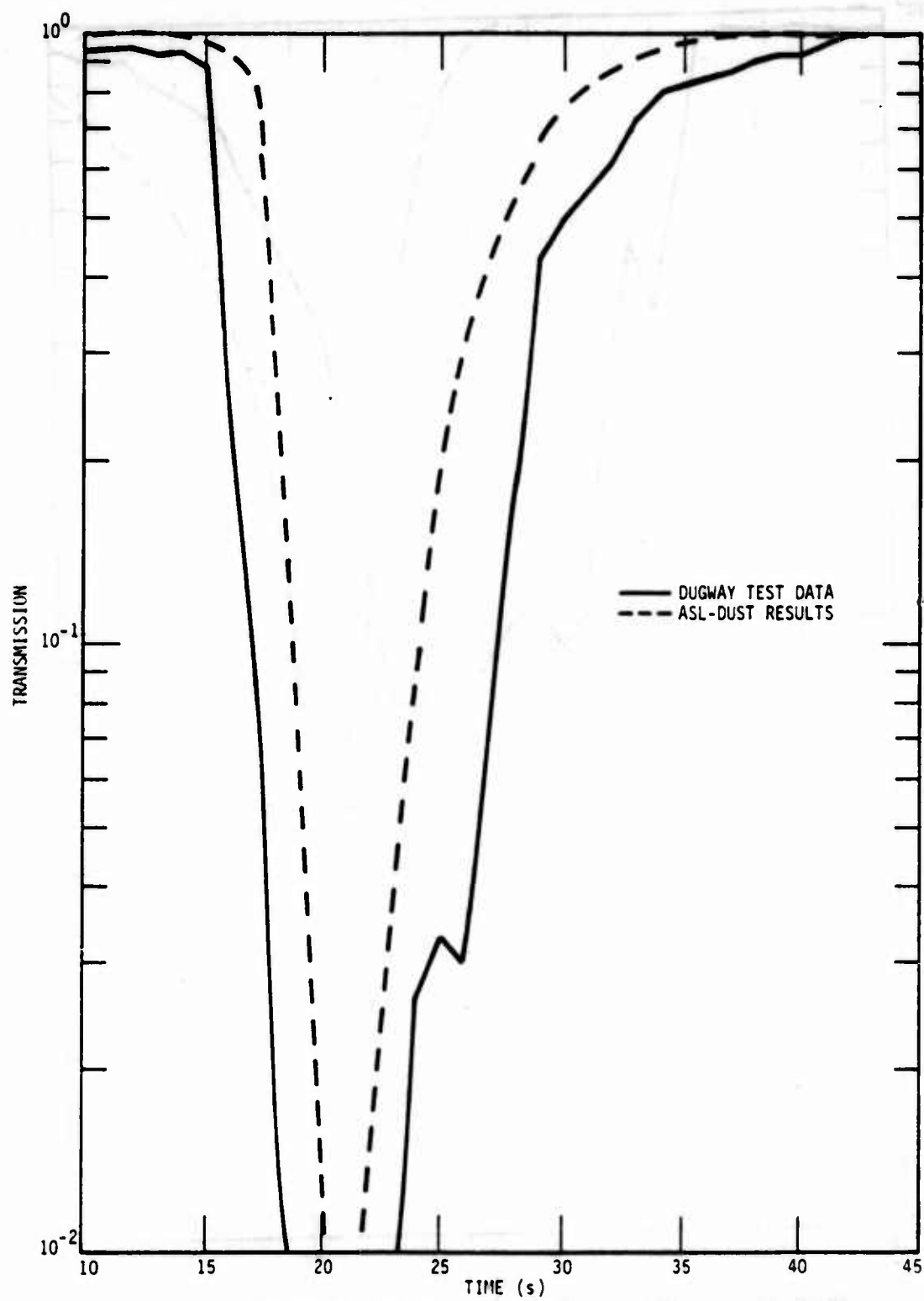
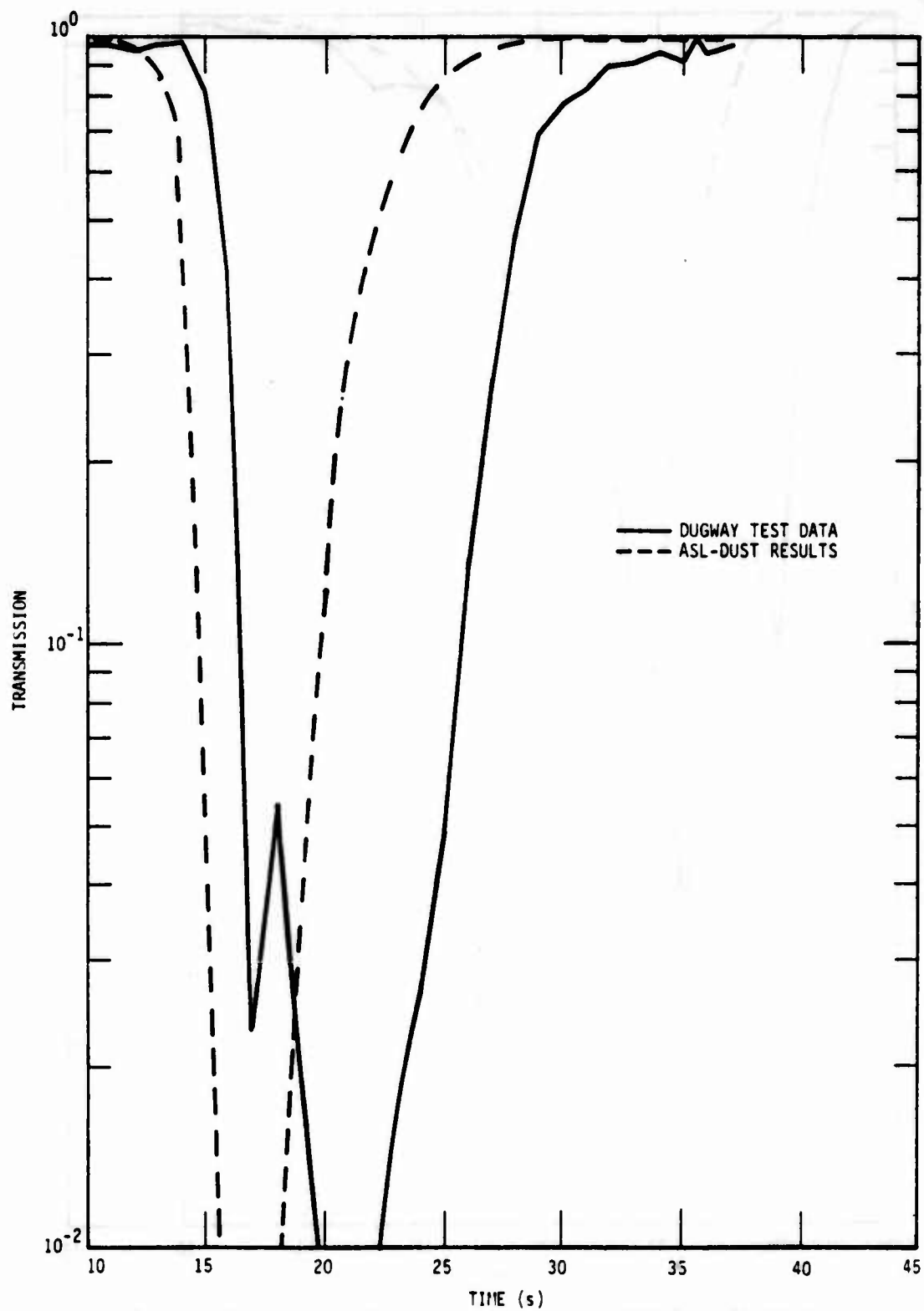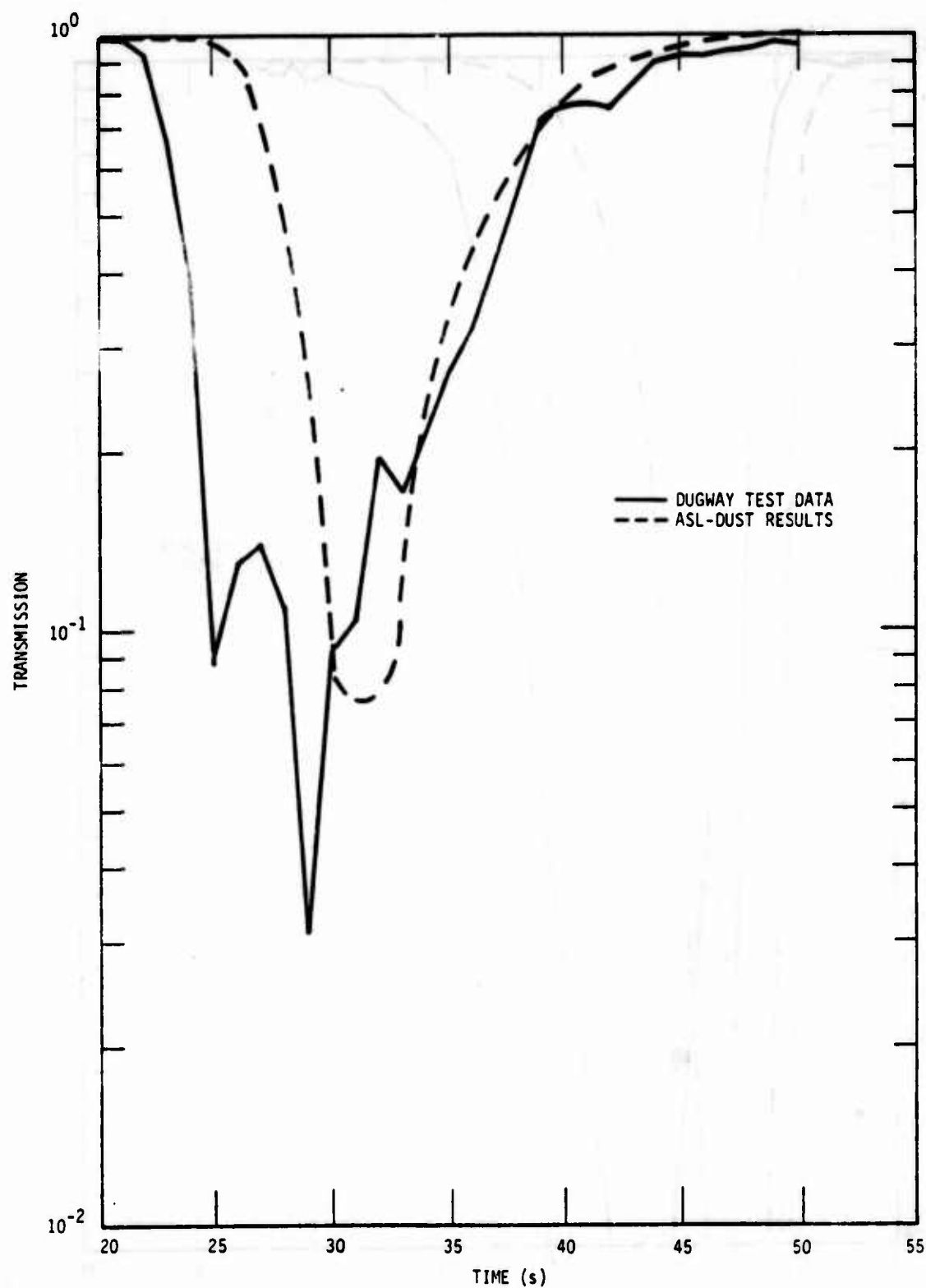Figure 42. Transmission at 3.4 μm for event D2, row 0.
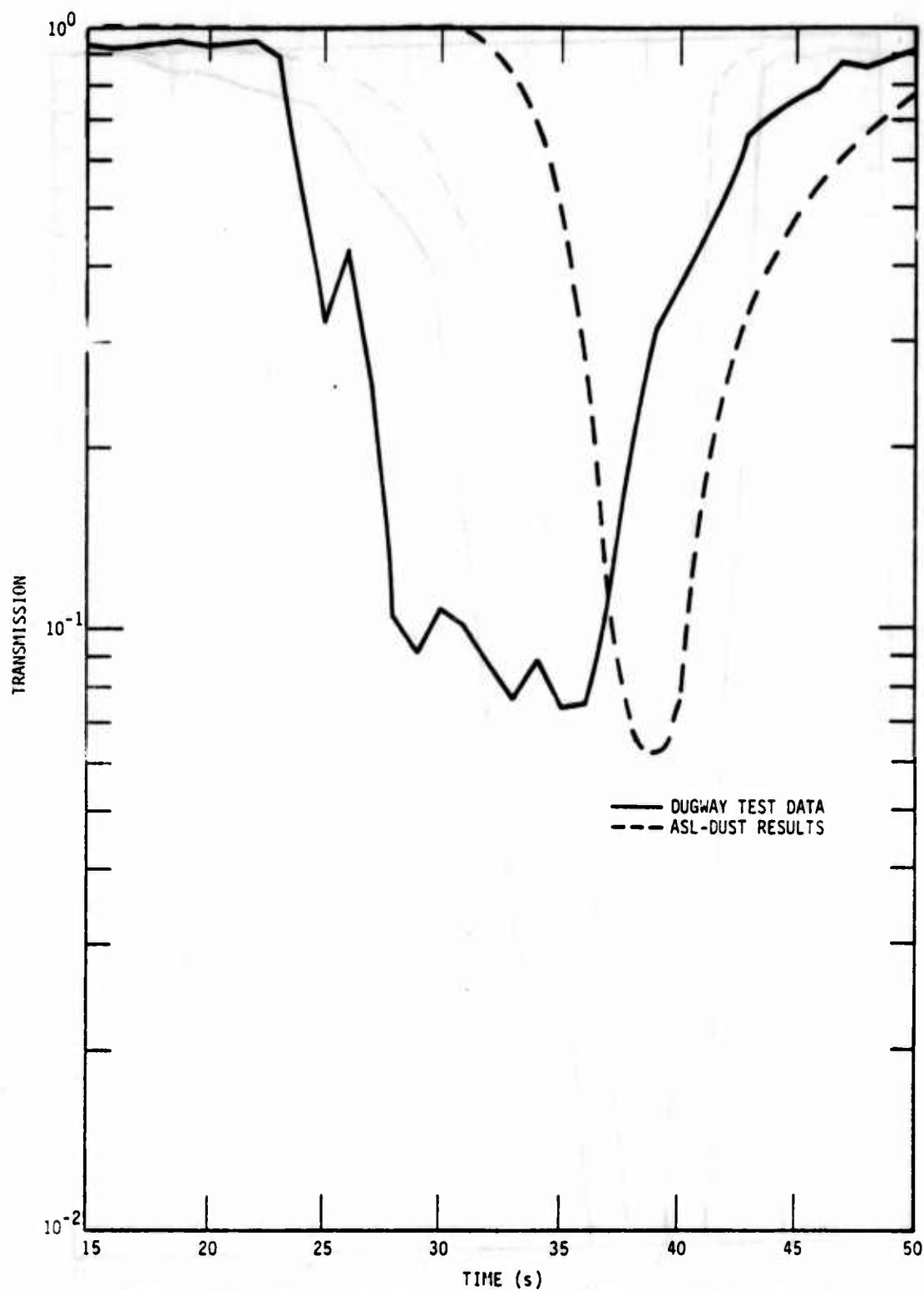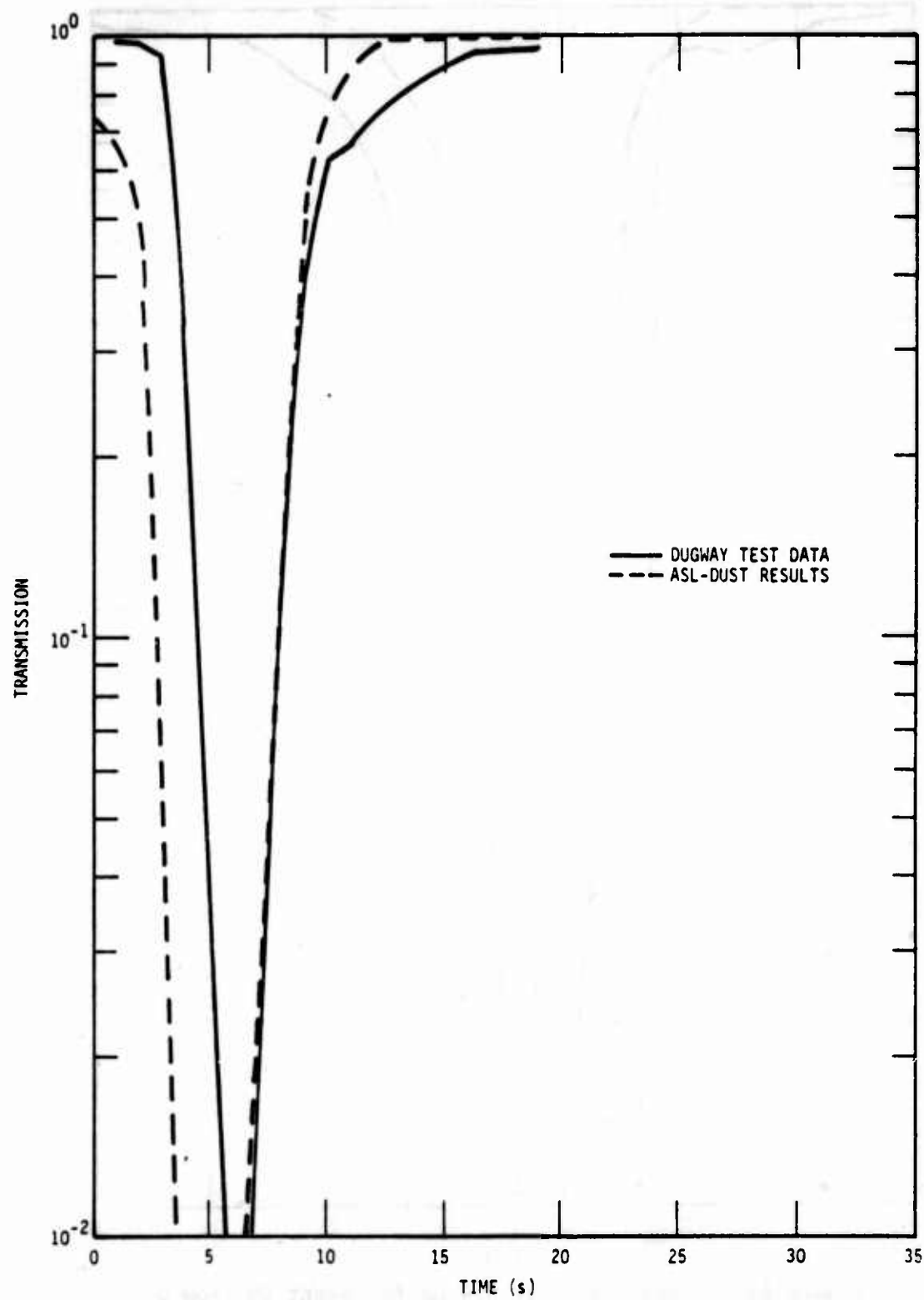
Figure 43. Transmission at 3.4 µm for event D2, row M.
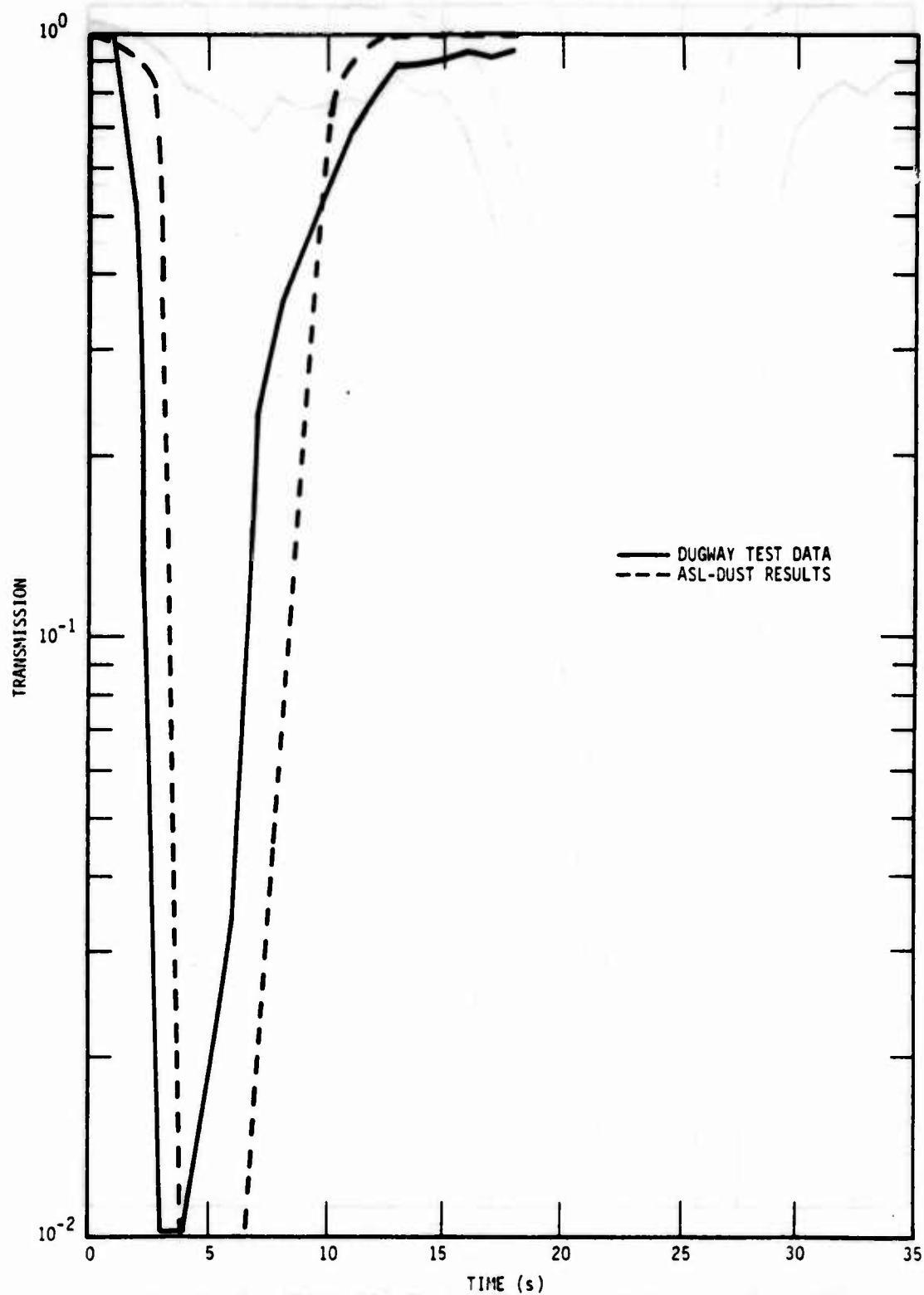
Figure 44. Transmission at 3.4 μm for event D3, row Q.
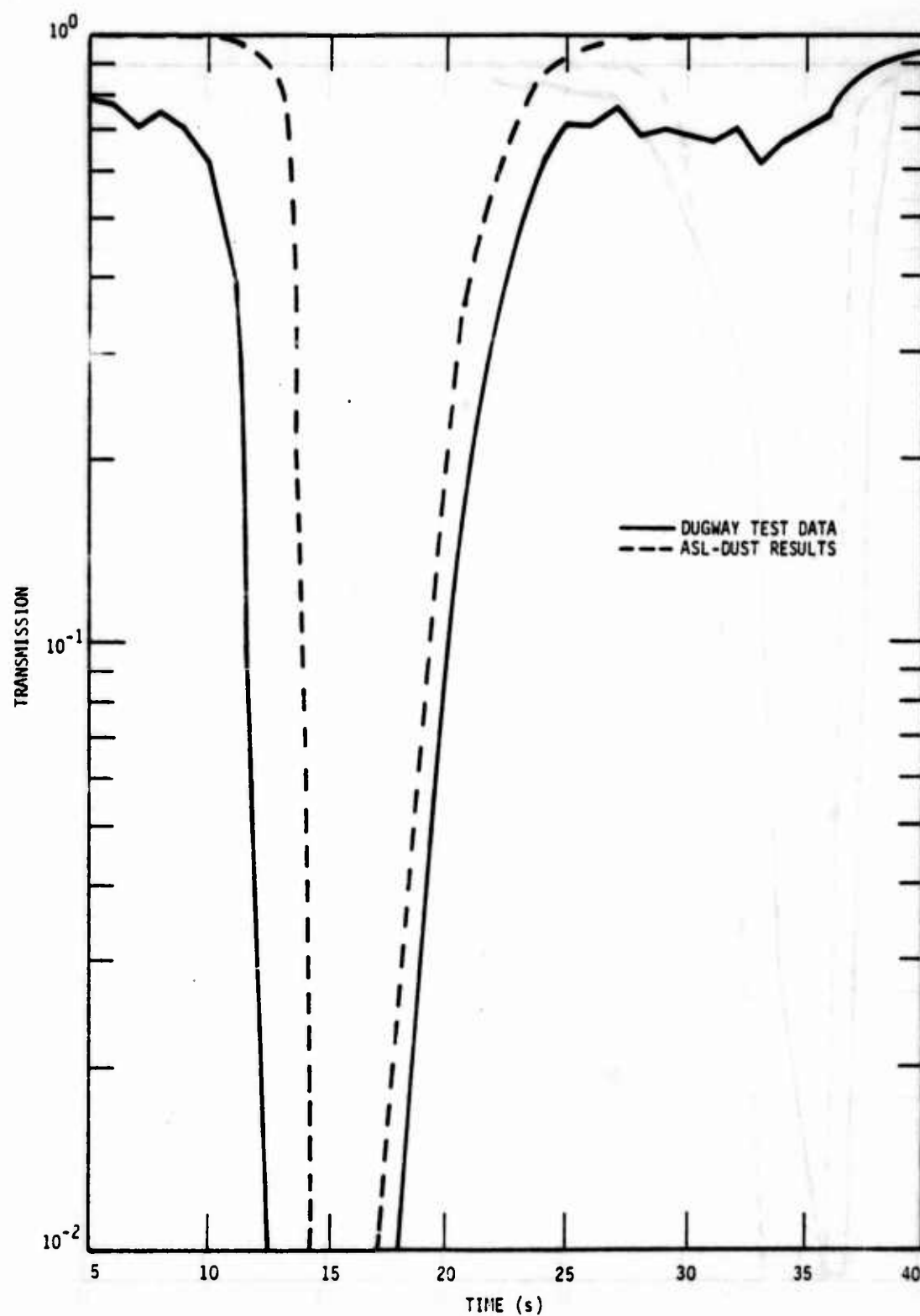
Figure 45.   Transmission at 3.4 μm for event D3, row C.
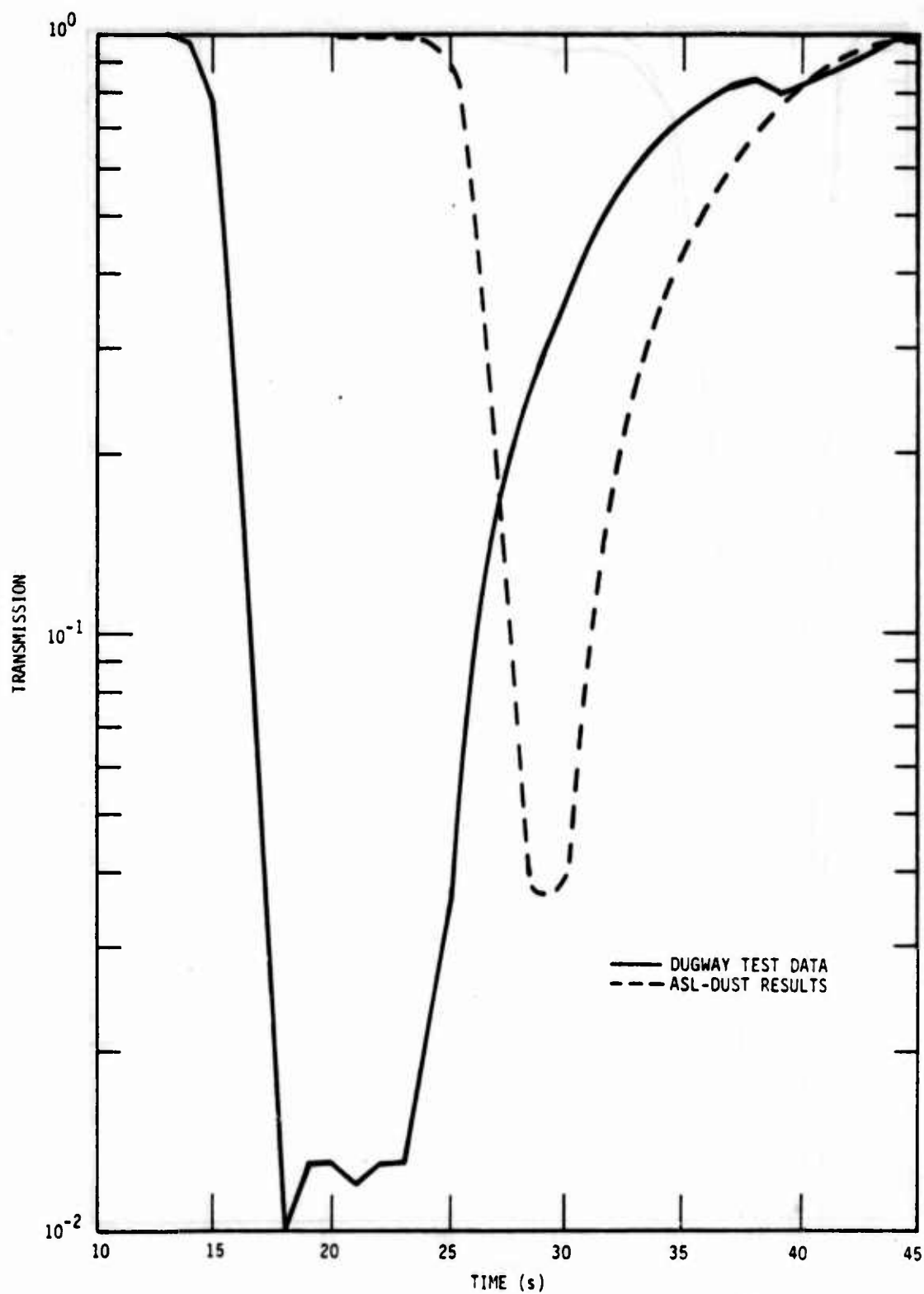
Figure 46. Transmission at 3.4 μm for event D3, row M.
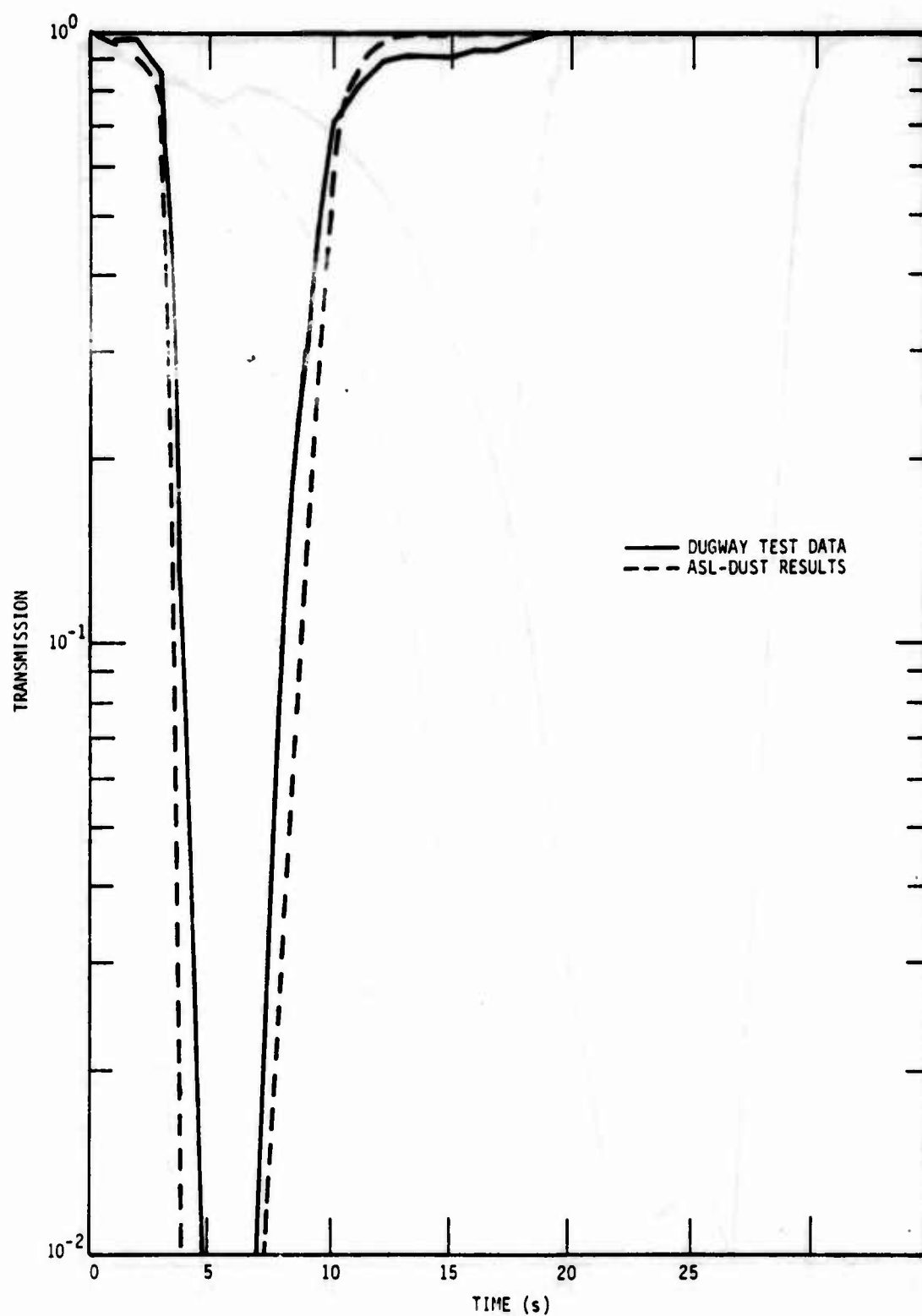
Figure 47. Transmission at 3.4 μm for event D4, row Q.

Figure 48. Transmission at 3.4 μm for event D4, row 0.

77

Figure 49. Transmission at 3.4 μm for event D4, row M.
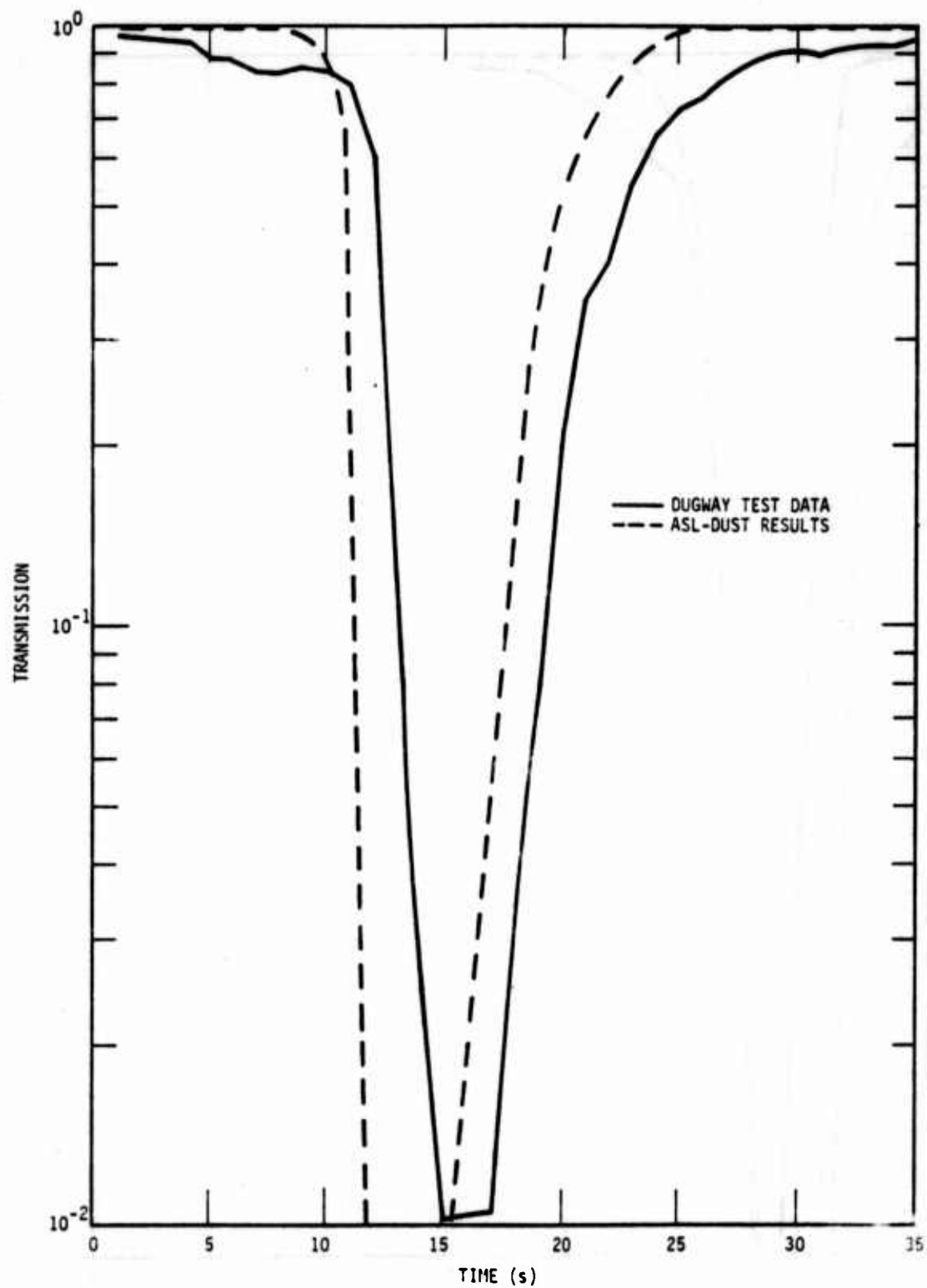
Figure 50.   Transmission at 3.4 μm for event D5, row Q.

Figure 51. Transmission at 3.4 μm for event D5, row 0.
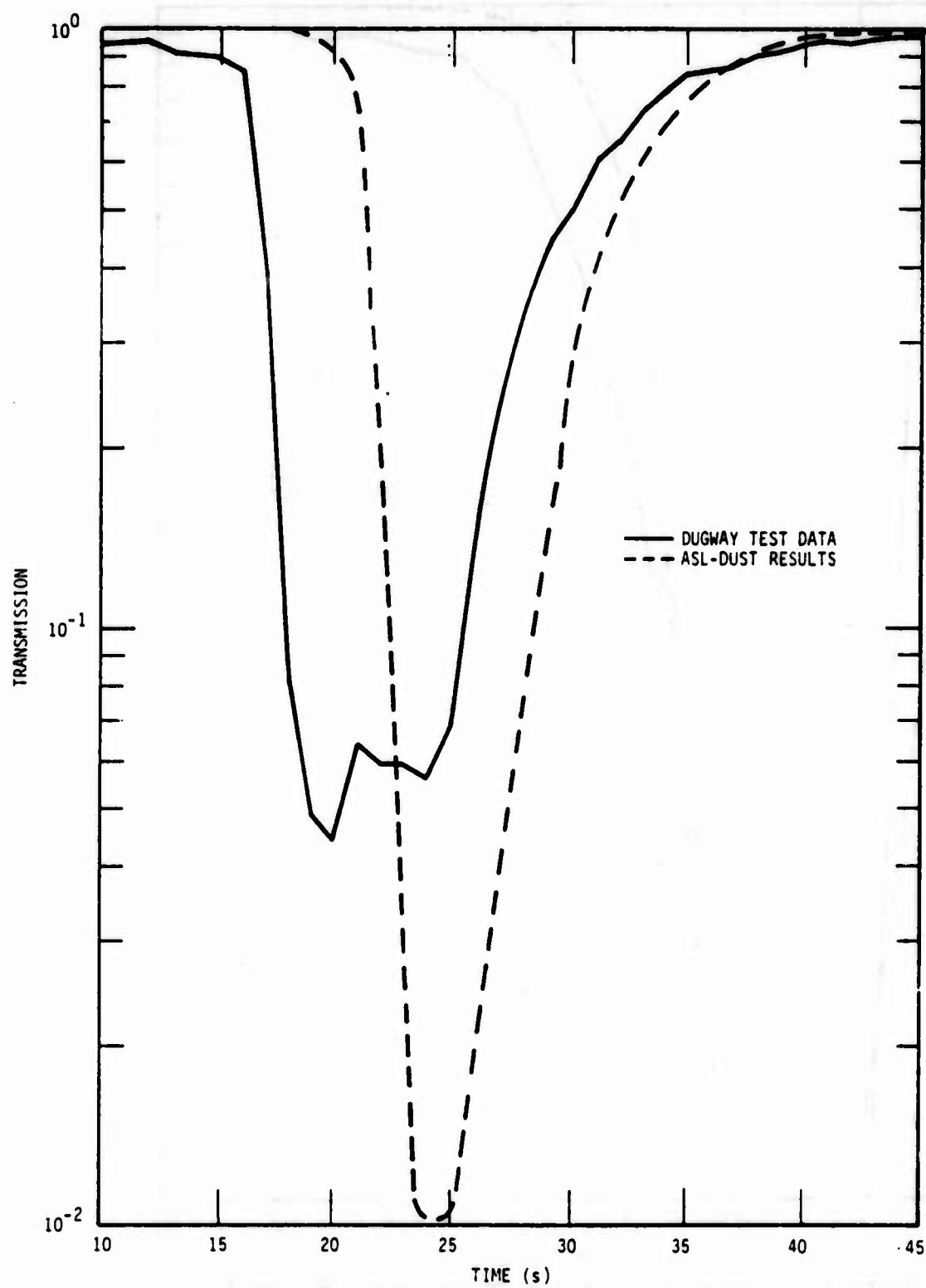
Figure 52. Transmission at 3.4 μm for event D5, row M.

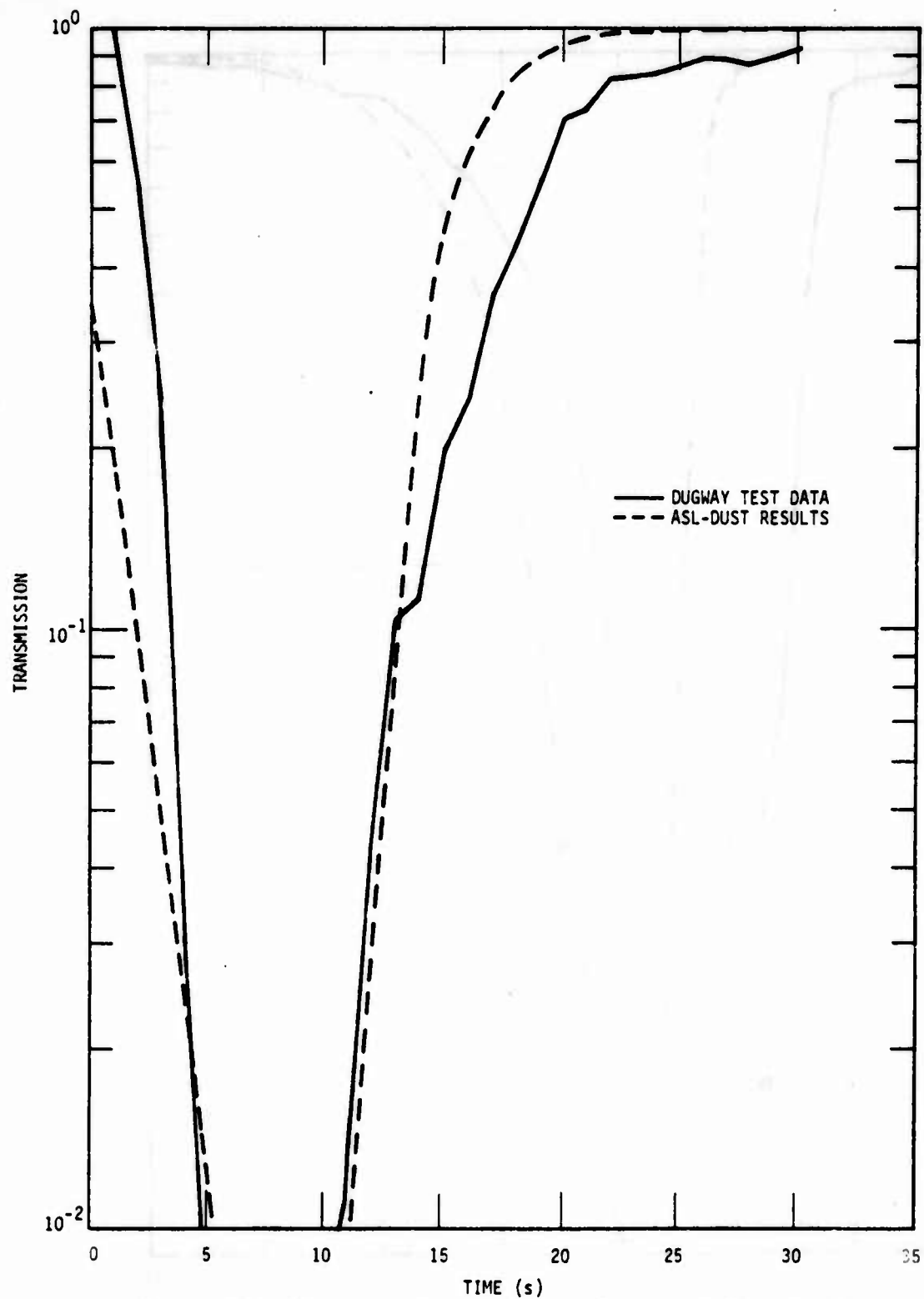Figure 53. Transmission at 3.4 μm for event D6, row M.

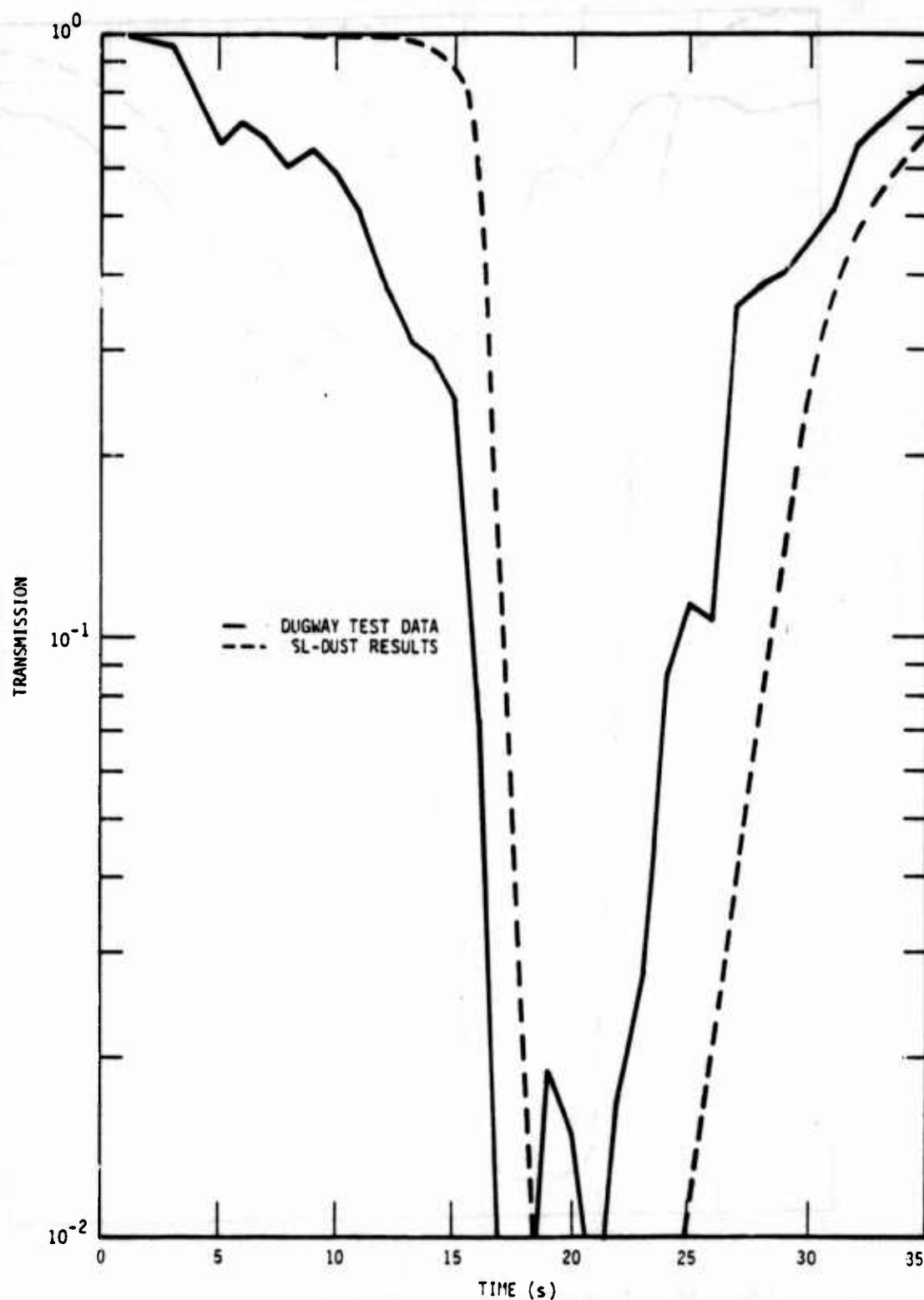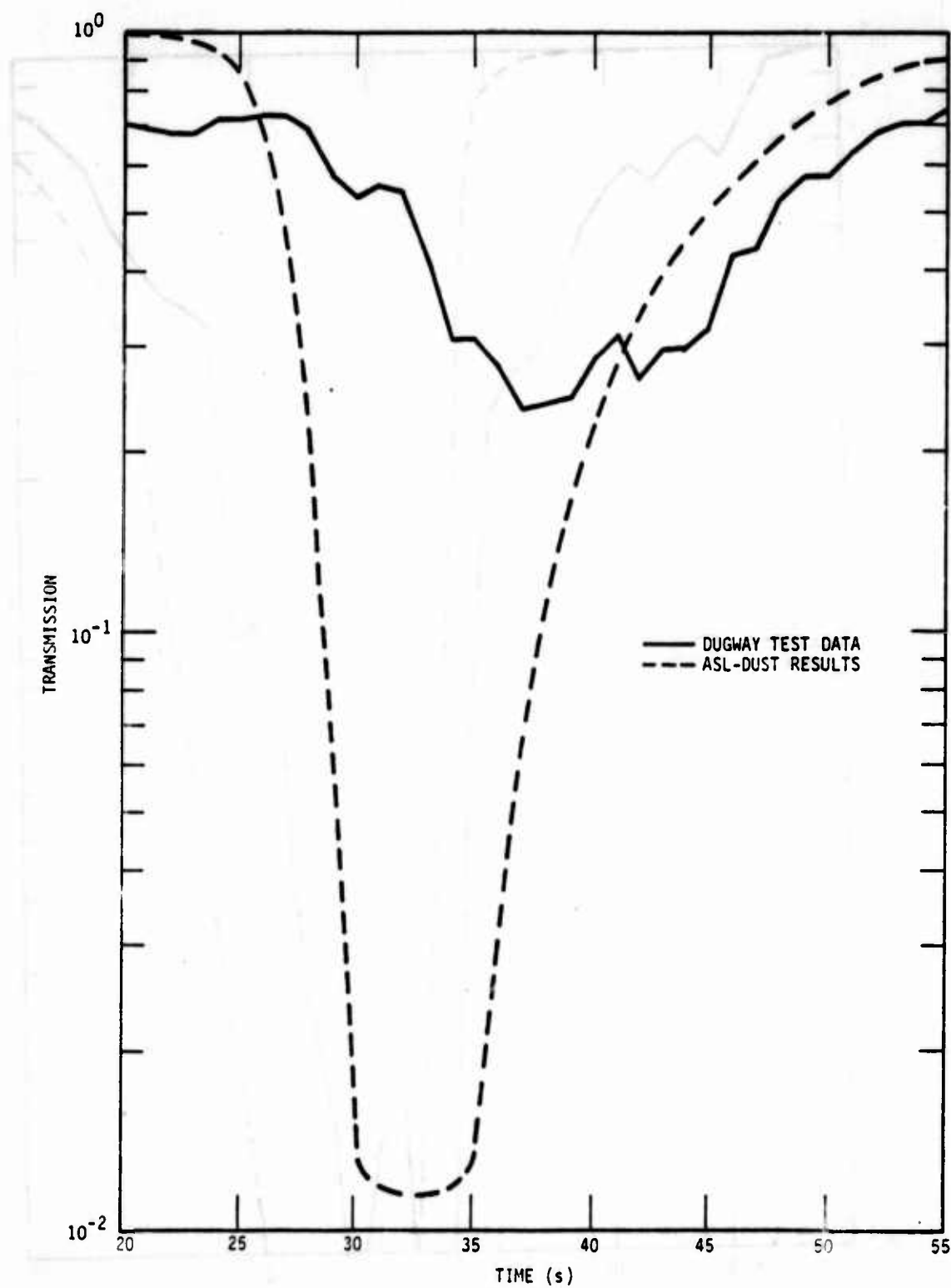Figure 54. Transmission at 3.4 µm for event D6, row 0.

Figure 55. Transmission at 3.4 μm for event D6, row Q.

REFERENCES

1. Thompson, James H., *Models for Munition Dust Clouds*, GE78TMP-99, General Electric-TEMPO, November 1978.

2. Thompson, James H., *ASL-DUST: A Tactical Battlefield Dust Cloud and Propagation Code, Volume 2 - User's Manual*, GE80TMP-5, General Electric-TEMPO, January 1980.

3. Pasquill, F., *Atmospheric Diffusion, The Dispersion of Windborne Material from Industrial and Other Sources*, 2nd Edition, John Wiley and Sons, 1974.

4. *Dust Trial Phase of Inventory Smoke Munition Test (Phase IIa)*, Preliminary draft copy of Final Test Report, 7-CO-RD7-DP1-002, U.S. Army Dugway Proving Ground, May 1978.

5. Preliminary Fort Sill Munitions Test Data, May 1978.

6. Lindberg, James D., editor, *Measured Effects of Battlefield Dust and Smoke on Visible, Infrared, and Millimeter Wavelength Propagation: A Preliminary Report on Dusty Infrared Test-1 (DIRT-1)*, ASL-TR-0021, U.S. Army Atmospheric Sciences Laboratory, WSMR, January 1979.

7. Miller, Charles A., *Terrain Characteristics at DIRT-1 Test Site White Sands Missile Range, New Mexico*, ASL-IAO-79-8146-1, U.S. Army Engineer Waterways Experiment Station, March 1979.

8. McMillan, R.W., et al, *Millimeter Wave Propagation Through Battlefield Dust*, Final Report, ASL-CR-79-0026-1, U.S. Army Atmospheric Sciences Laboratory, WSMR, June 1979.

9. *Fixed Camera Data, Dusty Infrared Test-1 (DIRT-1)*, 2 October through 14 October 1978, ASL-CR-79-00801, Physical Science Laboratory, New Mexico State University, August 1979.

10. VanDer Laan, Jan E., *Lidar Observations at 0.7 μm and 10.6 μm Wavelengths During Dusty Infrared Test 1 (DIRT-1)*, ASL-CR-79-0001-2, SRI International, September 1979.

11. *Preliminary NRL Filter Transmissometer Data from the Dusty Infrared Test-1 (DIRT-1)*, private communication, Naval Research Laboratory, August 1979.

12. Stull, V.R., *Carbon Particles in the Battlefield Environment*, GE79TMP-58, General Electric-TEMPO, October 1979.